Study on Prediction of Thrust Force on Wing with Elastic Deformation Effects

A Thesis

Submitted for the Degree of

Doctor of Philosophy

In

Mechanical Information Science and Technology

By

Aphaiwong Junchangpood

Department of Information Systems

Graduate School of Computer Science and Systems Engineering

KYUSHU INSTITUTE OF TECHNOLOGY

September 2012

Abstract

In this thesis, the simple predicting method of thrust-production on the wing's elastic deformation effects has been proposed, which is named DRR's principle. And then, the development of DRR's principle for the flexible wing is described. Particularly, emphasis has been based on the explanations the reasons of why DRR has been different in phase and amplitude with thrust coefficients.

The thesis consists of five chapters covering the background history, problem formulation, solution approach and discussion of the results and conclusions.

CHAPTER I deals with a detailed background history of the deformation effects to aerodynamic forces, problem associated with elastic deformation, its importance in practical applications in flying robot. And also, the research purposes are specified.

CAPTER II describes method of solution, development of a numerical algorithm, grid system, finite volume and finite element discretization of the governing equations, and the calculation of the physical amounts in fluid dynamic analysis.

CHAPERT III contends with the mathematical model of evaluating the deformation effects. Also, the previous works are described. The results of the effects of the vortex structures in the wake behind both the flapping rigid and elastic wings, and the varying the wing's flexibilities due to some ribs attached with the main spare of the wing structures is investigated. In addition, the characteristic effects of elastic deformation using FEM simulation are examined.

CHAPTER IV explains the relationships between DRR variable and thrust coefficient. And also, the vortex flow structure results obtained by FSI simulation are illustrated. In particular, the newly developed DRR's principle for the prediction of a dynamic thrust is explained and their mathematical results are discussed.

CHAPTER V in this final chapter, a conclusion is drawn regarding the robustness of the newly developed mathematic model in predicting simply the dynamic thrust based on the elastic deformation effects.

Especially, to verify DRR's principle, the reasons of their amplitude and phase difference have been found, as these are follows: First, for amplitude difference, due to highest *DRR* has been proportional to both the maximum trailing-edge deformation and deformational area, which at this point occurs zero deformational velocity ($V_{deform} = 0$). On the other hand, the maximum dynamic thrust has been dependant on both high amplitude of dynamic pressure difference and the trailing projection area. Otherwise, both *DRR* and C_T have coupled only with the maximum trailing deformation. Second, for phase difference, due to the effects of constructive interference between pressure difference, $\Delta p(t)$, and projection area, $A_{TE,deform}(t)$, with the same frequency but different amplitude have occurred, thus the resulting wave of thrust force has been equal to the sum of these two waves. However, the resulting wave of DRR has not only been affected by local $\Delta p(t)$, but also 3-D deformation of wing. Especially, it can also be explained by that K_{DRR} and C_{DRR}, where K_{DRR} indicates the potential energy caused by the surface pressure and total wing's deformation and the leading-edge deformation is indicated by $C_{DRR.}$ As results, for newly model of thrust coefficient based on DRR's principle, an error of between 8% and 18 % have occurred for high thrust and small thrust force region, respectively.

Finally, suggestion for future work has been highlighted.

Key words: Flapping wing, Elastic deformation, Thrust force, Fluid Structure Interaction, DRR's principle

Nomenclatures

a	acceleration	[m s^-1]
A_θ	Flapping angle amplitude	[deg]
A_ω	Angular velocity amplitude	[rad s^-1]
b	Wingspan	[m]
c	Chord length	[m]
Cd	Drag coefficient	-
c_m	Mean chord length	[m]
c_{ref}	Reference chord length	[m]
D	Drag force	[N]
DRR	Dimensionless deformational volume	-
E	Young's modulus	[Pa]
f	Flapping frequency	[N]
L	Lift force	[N]
p	Pressure	[Pa]
r	Distance	[m]
r_{md}	Mesh Displacement	[m]
r_E	Total Mesh Displacement	[m]
R	Half-wingspan	[m]
Re	Reynolds number	-
t	Time	[s]
T	Time period	[s^-1]
u, v, w	Velocity components	[m s^-1]
r_x, r_y, r_z	Cartesian coordinate components	[m]

Greek symbols

α	Angle of attack	[degree]
Δt	Time step	[s]
μ	Molecular viscosity	[Pa s]

ν	Poison's ratio, dynamic viscosity	-
δ	Deformational displacement	[m]
ε	Strain	[N m^-2]
φ	Phase difference	[rad]
θ	Flapping angle	[deg]
ρ	Density	[kg m^-3]
σ	Normal stress	[N m^-2]
τ	Shear stress	[N m^-2]
ω	Vorticity	[s^-1]
ω_{flap}	Flapping angular velocity	[rad s^-1]
τ_{xx} , τ_{yy}, τ_{zz}	Components of viscous stress tensor	

Subscripts:

i	inner
i,j	Cell centre value
flap	Flapping motion
max	Maximum value
min	Minimum value
LE	Leading edge
TE	Trailing edge
0	free stream condition/ initial

Table of Contents

Page

List of Figures

Page

List of Table

Page

CHAPTER I

Introduction

1.1 Introduction

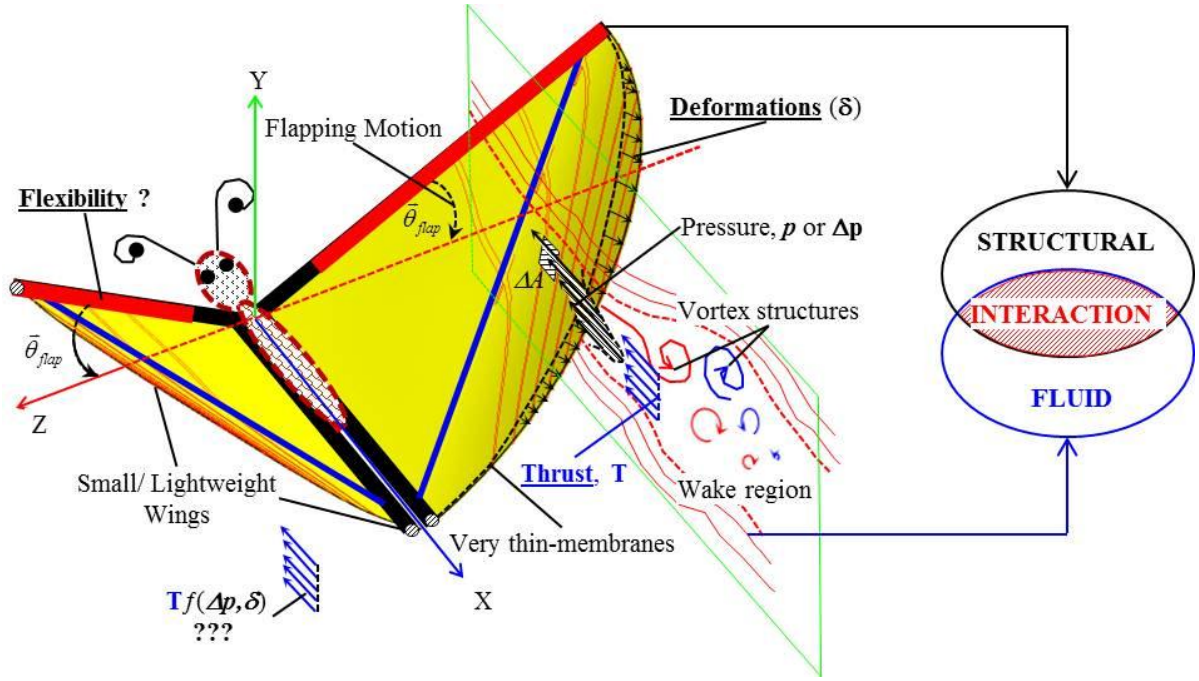

Fig. 1-1 Imaginary of actual flow over moving elastic body and fluid-structure interaction (FSI) coupled problems

Flying insects, birds, or aquatic animals fly or swim skillfully by controlling a flow field around their body using their wings or tail flukes of complex shape and their elastic deformation. There are two classes of aerial flapping flight (insect-like and bird-like). Birds have muscles attached to bones along the wing, used for flight and maneuvering. This makes them heavy and relatively less efficient (in terms of specific power). On the other hand, insects possess an exoskeleton: all actuation is carried out at the wing root and, consequently, the wing structure is very light, generally accounting for ~1% of the insect's weight. This makes insect flight very attractive as a model, while also satisfying all the other requirements of the flight envelope identified above (especially hover) for the micro air vehicles (MAVs) [1-2]. Hence, the insects have been evolved and perfected their flight, making them the most agile and maneuverable creatures for their size today. Many researchers attempt to mimic these characteristics of the insect flight, and construct a small flying robot or MAVs for performing the special missions [2-9]. However, the relationships need to be clarified as to how the complex shapes and elastic deformation can obtain a good condition for flight.

It is conceived, that flying insects acquire lift through interaction with the vortex around the wing boundary generated by flapping [10], and therefore, many researchers have recently studied this mechanism by way of the experimental and numerical analysis up to now [5-12]. Especially, this flow around moving elastic body is treated as the fluid-structure interaction (FSI) problems as imaginary illustrated in Fig. 1-1. There are a variety of the phenomena with FSI applications in many areas, such as analysis of aneurysms in large arteries, stability analysis of the aircraft wings, turbo-machinery design, design of the bridges, and so on. Hence, this is a new challenge in the fluid engineering field to clearly understand the phenomena of deforming structure largely and complexly associated a flow field characteristic. In this research, the relationships between the wing's flexibilities and thrust-production will be studied to understand its mechanisms, and to be significant for the applications.

Presently, other researchers have investigated the way in which flexibility affects the aerodynamics of flapping wing of airfoil [13] and the flapping root's wing [14-16]. Both have been studied by the experiments only in large wing [17-21], and 2D-simulation [22-24]. However, this information can also be used for solving the fluid-structure coupled problems, needed for the engineering design of the ornithopters as shown in Fig. 1-2. Figure 1-2(a) shows the actual wing designed and CFD wing modelling, which was used for studying about the relationships of an aeroelastic coupling in flapping wing system [25]. They also applied the small sensors for controlling the wing's deformation as well as the active control the flow field around the flapping elastic wings. Figure 1-2(b) shows the different wing constructions, which was used for determination of its effects to the aeroelastic characteristics by experimentation [26]. And also, the aeroelastic of the flapping wing has been investigated by experimentation [18, 19]. Many researchers have studied about the aeroelatic in the flapping wing system by experiment as well, because the wing systems have been large structures. Thus, it is easy to measure the aerodynamic force at a large scale. However, for the small wing system, difficulties arise when attempting to measure the small forces acting on the wing surface as illustrated in Fig. 1-1 before. In particular, these problems become even more difficult and highly complex, when the deformation of the elastic body by a fluid is introduced and flow field varies with the moving body. Also, the effects of a wing's twisting stiffness on the generated thrust force and the power required at different flapping frequencies has been investigated experimentally using the model of ornithopter as shown in Fig. 1-2(c).

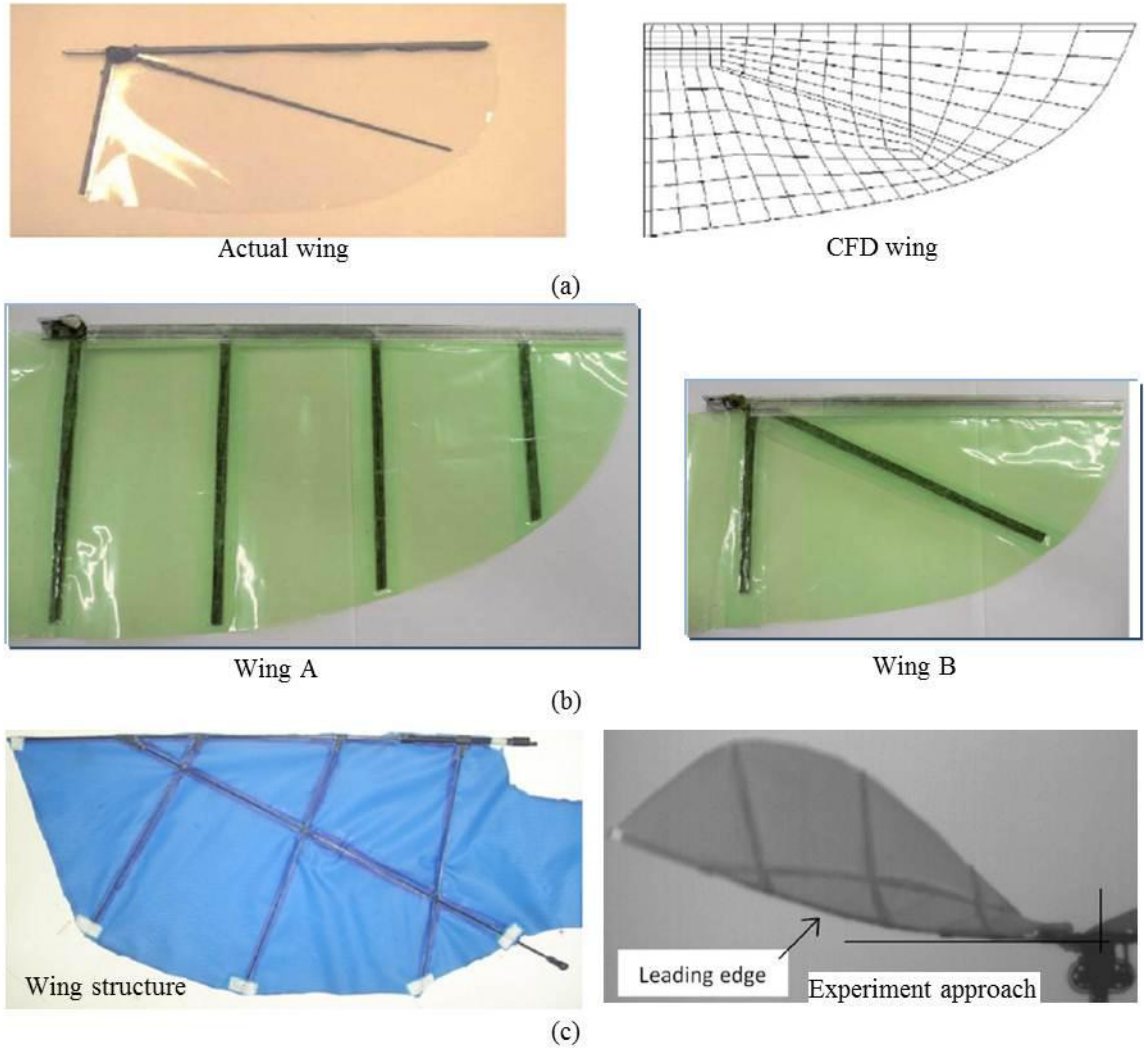

Fig. 1-2 Flapping wings of flying robots or MAVs, (a) Aeroelastic coupling in flapping wing, (b) Effects of different wing constructions, (c) Aroelastic investigation by experiment

However, it has not been fully solved. Recently, flow field around a flapping rigid wing has been investigated, which is one of fluid-structure interaction (FSI) applications as mentioned before. In previous works, a flow field around the flapping rigid wings through numerical analysis has been performed. In this work, one-way coupled analysis was employed for considering the moving boundary problems, in which the elastic deformation is expressed by a function [12]. In the case of the flapping rigid wing or small deformation, the way of giving a structural deforming functions have performed the wing deformation accurately. On the other hand, other researchers proposed the method of the finite element model to consider the structural deformations, in the cases of small deformation mostly [27-29]. However, in the case of a large and complex deformation, it could not be probably resolved by the functions. Hence, we have been going to resolve this structural problem with the finite element method (FEM).

Actually, to determine an ideal elastic deformation of the wings, there are many ways to make these wings, such as varying material properties, wing flexibility, wing configurations, wing structures due to some ribs, and so on. For the flapping flight, note that flapping wings are not limited to a fixed wing kinematic motion, but instead can change their wing's kinematic motion to gain the most advantageous geometry when maneuvering or transitioning from one flight mode to other [30]. The flapping robot does not have as any degree of freedom as natural flyers [19]. Rather, for the small wing structures, it has been impossible to control the wing's kinematic motion. Then, a good structural designing of the wings for itself deformation has proven to be a better way. Moreover, the relationships between the kinematics of deformation of the flexible fin and the surrounding unsteady flow have been studied [31].

In this thesis, the new simple way of how to predict the domination of the elastic deformation on production of driving force (thrust) is established, in which wing deformation is in the design of a wing. Hence, there is a need to design an efficient wing to achieve higher performance. Although the analysis approach for a flapping elastic wing is reasonably fluid-structure coupled problems related to the wing's material properties, realistic conditions, and coupling method. Presently, these analysis methods need improved criteria for solving those problems. The performance of the wings is critically dependent on the wing's characteristics and deformation. Specially, the new simple way of prediction has been proposed which is named DRR's principle. It is seemed to be a good way to predict their effects. However, it has to be modified to be satisfied in many area applications, and given the explanations how DRR can predict the thrust-production of the wings with the elastic deformation effects.

The present investigations about the flapping wing and their aerodynamic characteristics are to tackle fluid engineering FSI applications involving lightweight structure. Right from the start it was clear that highly advanced solvers for both CFD and CSD are required for this purpose, i.e., a finite-element solver for shell and membranes [32]. In particular, the calculation of the aerodynamic characteristics in separated flows is a fairly complicated problem [33]. And, it has been reported that high lift force of an airfoil can be controlled by the flow separation over deflect trailing edge flaps [34]. It seems that DRR's principle has been similar with the other researches.

1.2 Problem formulations

As mentioned in introduction, the object of the present investigation is to explain the phenomena of the aerodynamic characteristics of flapping wing at low Reynolds numbers. Many researches have been studied about these phenomena [35-46]. The need for the study arises due to no good new way for predicting the elastic deformation effect to the thrust force. DRR's principle has to be developed for this. The numerical techniques have been taken up for more realistic analysis since the flow phenomena is complex due to elastic deformation. An aerodynamic analysis is required to understand the flow phenomena and incorporate design changes without conducting simulation test. Methods which exist to analyse airfoils are potential method, IBM method Morphing [47, 48]. All these methods have limitations. Potential methods are purely inviscid whereas IBM (remeshing) method limited to boundary layer assumptions. So complete Navier-Stokes equation method is more general

which includes all the terms and hence can be used to analyse complex geometry, complex flow field such as massive separation and unsteady flows.

Recently, it has not had a good way for predicting the thrust generated by an elastic deformation. To be useful for fluid engineering, I have proposed the new way for do that, which is named the principle of the deformation region ratio (DRR). Actually, the research aim is to study the order magnitude of the wing's deformation effects to increasing dynamic thrust, which is compared with flapping rigid wings and original wing shape. Because of the shape of flapping elastic wing can be changed by flexibility and flapping motion, hence it causes to the thrust produce of the wings either. Most of the designing the wings have not been considered that the elastic deformation effects can improve the wing efficiency by itself deformation.

1.3 Research purpose

In order to predict the elastic deformation effects to thrust-production on the wings, two different approaches have been proposed in this work as follows.

One is the prediction of thrust-production using FSI simulation, which is one-way simulation with FEM simulation in structural analysis. Second, simple predicting method based on the characteristic effects of the elastic deformations, DRR's principle has been proposed to be advantages for considering those deformation effects. Since, it is found that dynamic DRR has been similar tendency with dynamic thrust. However, they have been different in their amplitude and phase. Hence, to develop DRR model, the reasons of its difference have to be explained following objectives are below:

The aims of these research purposes are to explain why the amplitude and phase of DRR have been different with C_T, and to find how *DRR* can predict C_T. In addition, I would like to clarify how the wing's flexibility affects to thrust-production using simple predicting method of newly DRR's principle.

Especially, the research purposes have mainly two issues on which have been carried out as being explanatory and predictive. First, it is to analyse why the relationships, patterns and links between DRR variable and thrust coefficient have occurred. Second, it is to develop a mathematic model of DRR that predicts the likely the thrust coefficient.

CHAPTER II

Theory and Methodology

In order to address the technical challenges associated with successful the micro aerial vehicles (MAVs) development as Fig. 2-1(a) [18-20], designers are looking to biological flight for inspiration. Successful development of these biomimetic MAV concepts will require significant advancements in the fundamental understanding of the unsteady aerodynamics of low Reynolds number fliers and associated fluid-structure interactions as Fig. 2-1(b). The inherent flexibility in the structural design of lightweight MAVs and the exploitation of that flexibility creates strong coupling between the unsteady fluid dynamics and the airframe structural response giving rise to tightly integrated, multidisciplinary physics. Conventional simplified analytical techniques and empirical design methods, although attractive for their efficiency, may have limited applicability for these complicated, multidisciplinary design problems. Critical insight into the highly complex, coupled MAV physics calls for the exploitation of advanced multidisciplinary computational techniques. Beside experimental investigation, numerical simulations have been better approach for solving this kind of problem. However, both (Fluid and Structure) fields have been considered following details below.

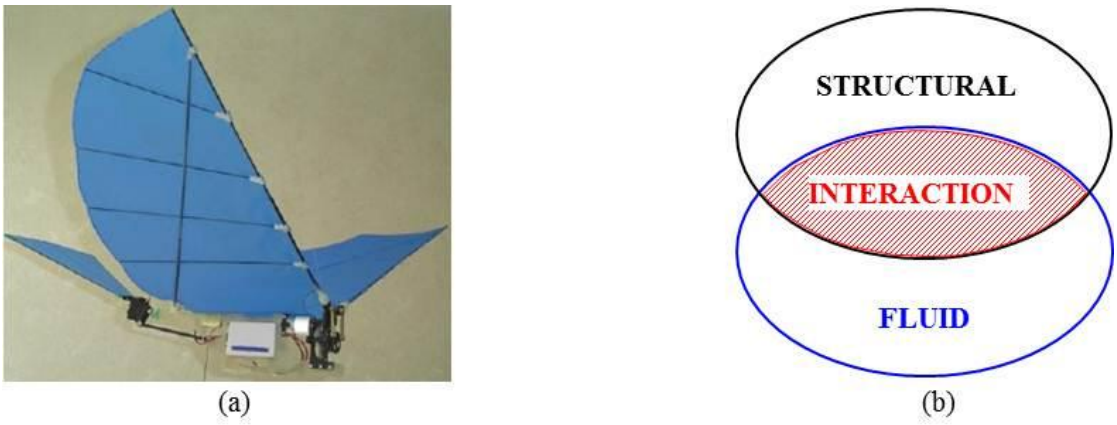

Fig.2-1 Fluid structure coupled problems, (a) MAV application, (b) Overlap between fluid and structure

2.1 Computational fluid dynamics (CFD)

2.1.1 Governing equation for FVM

The present study is the global analysis of the flow past 3-D flapping wing at low Reynolds number region using Navier-Stokes equations. Its analysis is confined to viscid flow for the boundary conditions. For analysis of the flow phenomena, a flow over both the flapping rigid and flexible wing is considered. The governing equations and assumptions are the unsteady flow, three-dimensional incompressible and turbulent flow. Hence, the continuity and Navier-Stokes equation [49] can be given as:

$$\frac{\partial \rho}{\partial t}+\frac{\partial}{\partial x_i}\left(\rho u_i\right)=0 \tag{2-1}$$

$$\frac{\partial}{\partial t}\left(\rho u_i\right)+\frac{\partial}{\partial x_j}\left(\rho u_i u_j\right)=-\frac{\partial p}{\partial x_i}+\frac{\partial}{\partial x_j}\left[\mu\left(\frac{\partial u_i}{\partial x_j}+\frac{\partial u_j}{\partial x_i}-\frac{2}{3}\delta_{ij}\frac{\partial u_i}{\partial x_i}\right)\right]+\frac{\partial}{\partial x_j}\left(-\rho\overline{u_i' u_j'}\right) \tag{2-2}$$

Here, u is the velocity, p is the pressure, ρ is the density of air, and μ is the viscosity.

2.1.2 Discretization

The discretization of this wing model is based on a three-dimensional finite-volume method (FVM) which is used to discretize the governing Eqs. (2-1) and (2-2).The discretization is done on a curvilinear, block-structured body-fitted grid with collocated variable arrangement by applying standard schemes. A midpoint rule approximation of second-order accuracy is used for the discretization of the surface and volume integrals. Furthermore, the flow variables are linearly interpolated to the cell faces leading to a second-order accurate central scheme. In order to ensure the coupling of pressure and velocity fields on non-staggered grids, the momentum interpolation technique is used.

2.1.3 Turbulent model of SST k-ω

In a turbulent flow, due to the flow behaviours around the flapping robot are the turbulent flows, therefore a turbulent modelling is considered also. The turbulent flows are characterized by fluctuating velocity fields which these fluctuations mix transported quantities. Instead, the instantaneous (exact) governing equations can be time-averaged in a modified set of equations that are computationally less expensive to solve. However, the modified equations contain additional unknown variables, and turbulent models are needed to determine these variables in the terms of know quantities. In this simulation model, Shear-Stress transport (SST) $k-\omega$ model [50-52] was chosen, because the $k-\omega$ model can predict a characteristic behaviour well in the boundary layer on the wings. The transport equations for SST $k-\omega$ model are the turbulence kinetic energy (k) and specific dissipation rate (ω), which are given as:

The turbulence kinetic energy (k):

$$\frac{\partial(\rho k)}{\partial t}+\frac{\partial(\rho k u_i)}{\partial x_i}=\frac{\partial}{\partial x_j}\left(\Gamma_k\frac{\partial k}{\partial x_j}\right)+G_k-Y_k+S_k \tag{2-3}$$

The specific dissipation rate (ω):

$$\frac{\partial(\rho k)}{\partial t}+\frac{\partial(\rho k u_i)}{\partial x_i}=\frac{\partial}{\partial x_j}\left(\Gamma_k\frac{\partial k}{\partial x_j}\right)+G_k-Y_k+S_k \tag{2-4}$$

In Eqs. (2-3) and (2-4), G_k represents the generation of turbulence kinetic energy due to mean velocity gradients. G_ω represents the generation of specific dissipation rate. Γ_k and Γ_ω represent the effective diffusivity of k and ω, respectively. Y_k and Y_ω represent the dissipation of k and ω due to turbulence. S_k and S_ω are user defined source terms. All of the above terms are calculated as described in reference [50].

2.1.4 Dynamic mesh method

Although systems for physically based fluid animation have developed rapidly in recent year and can now reliably generate production-quality results, they still have some limitations. Simulation domains can change substantially from step to step because of deforming boundaries, moving obstacles, and evolving fluid motion. For the flapping wing model, it is treaded as moving boundary problem. So, dynamic mesh method is provided for solving this kind of problem in FLUENT solver. In deforming fluid zone, only tetrahedral cells of the elements can be applied to the dynamic mesh model. The remeshing method is used for generate the new mesh which can decrease or add the number of elements.

2.2 Computational structural dynamic (CSD)

Actually, a structural analysis is a key part of the engineering design of structures or structural engineering. It is to determine of the effects of loads on physical structures and their components. In addition, it incorporates the field of applied mechanics, materials science and applied mathematics to compute a structure's deformations, internal forces, stresses, support reactions, accelerations, and stability. The results of the analysis are used to verify a structure's fitness for use, often saving physical tests [32, 53]. In order to compute the wing's deformations, CSD method is achieved, which the solutions are derived from the equations of linear elasticity. The equations of elasticity are system of 15 partial differential equations. Due to the nature of the mathematics involved, analytical solutions may only be produced for relatively simple geometries. Hence, the wing's deformations are large and complex. It might be impossible to estimate by making a function of elastic deformation. For complex geometries, a numerical solution method such as the finite element method (FEM) is necessary. This way is employed for obtaining the wing's deformation.

In this section, the structural analysis is described to determine an elastic deformation of the wing structures due to the wing's flexibilities, which is the way of the rib-wing structures. Three types of the wing structure were varied for modelling as shown in Fig. 2-2. The elastic deformations were obtained for different wing structures and materials, and we show how the elastic deformation and inertial flapping forces affect the dynamical behaviours of the flapping wings.

2.2.1 Governing equation for FEM

When the flapping elastic wing is working, it is treated as a transient structural problem. To determine the time-varying displacements, strain or internal forces, we have also concerned over the structural behaviours of the flapping elastic wing under an inertia force. Based on the continuum mechanics assumption the dynamic equilibrium of the structure is described by the momentum equation given in a Lagrangian frame of reference (see section 3.2.5 in Fig. 3-11(a)). Allowing large deformations, where geometrical non-linearities are not negligible the following boundary value problem has to be considered, which can be given as:

$$[M]\{\ddot{u}(t)\}+[C]\{\dot{u}(t)\}+[K]\{u(t)\}=\{R(t)\} \tag{2-5}$$

where $\{R(t)\}$ is a vector containing the aerodynamic forces associated with the aerodynamic loads, and $\{\ddot{u}(t)\}$, $\{\dot{u}(t)\}$, and $\{u(t)\}$ are the acceleration, velocity and displacement vectors of the finite element assembly, respectively. These governing equations are solved by the discretization method being the finite element method (FEM) [54].

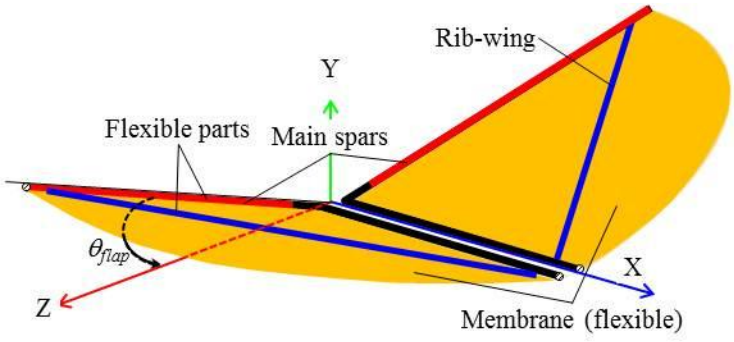

Fig. 2-2 Wing structures for structural analysis, (a) A-Type, (b) B-Type, (c) C-Type

2.3 Fluids-Structure Interaction (FSI) Simulation

In fluid and structure dynamic analysis, for a moving boundary problem, as one-way coupled method, the boundary motion was obtained by user of defined function (UDF). It was able to perform the boundary motion of rigid structure or small deformation structure, but this way is impossible to solve the large and complex structural deformations. For the moving boundary problems in two-way FSI analysis, the boundary is moved by momentum transfers across the interface between fluid and structure domains as shown in Fig. 2-3. In particular, fluid boundary moving depends on the structural deformation. The structural deformation can be defined by the finite element analysis (FEA). As well known in Structural engineering field, the finite element method (FEM) can be employed to obtain the solution accurately. After that, the communication data is controlled by the coupling method, which is explained in next topic.

2.3.1 Arbitrary Lagrangian-Eulerian (ALE) formulation

Within a FSI application the fluid forces acting on the structure lead to the displacement or deformation of the structure. Thus the computational domain is no longer fixed but changes in time, which has to be taken into account. Besides other numerical techniques, the most popular one is the so-called Arbitrary Lagrangian–Eulerian (ALE) formulation. Here the conservation equations for mass and momentum, which are to be solved based on a finite-volume scheme, are re-formulated for a temporally varying domain, i.e., control volumes (CV) with time-dependent volumes *V(t)* and surfaces *S(t)*. Hence the governing equations in ALE formulation expressing the conservation of mass and momentum read as referenced paper [32]

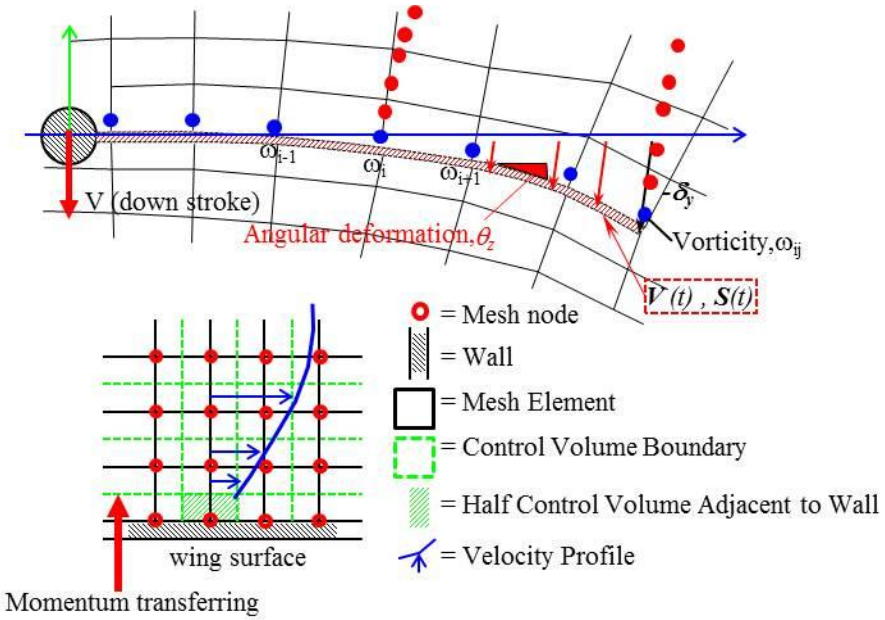

Fig. 2-3 Schematic of fluid-structure coupling for FSI simulation

The focus of the study is the analysis of aero science issues associated with a flexible membrane wing, using numerical simulation. The specific case to be considered corresponds to the experiments of butterfly robot [1] where flow visualizations as well as PIV measurements have been carried out for a simple membrane wing. The FSI approach [2] is employed to compute the turbulent flow field present in the experiments of butterfly robot. The FSI approach exploits the properties of a well validated, robust, fourth-order Navier-Stokrs solver [50-54]. This aerodynamic solver is coupled with a three-dimensional finite element rib-wing structural model suitable for the highly nonlinear structural response associated with a flexible wing frame.

2.3.2 Coupling method

In this method, we used the decoupled solver with the governing equations of the structural and fluid region independently. We perform a coupling simulation transferring on the fluid structure interface by using ANSYS 13.0 and ANSYS-CFX 13.0. The phenomena on the fluid, structural, and their interface region adequately are needed to keep convergence using iterative calculation because of strong interaction between the fluid and structural region. Maximum number of iterations of 10 each and 1×10^{-4} of convergence criterion on the fluid and structure solutions are defined. The transferred loading data are relaxed and calculated iteratively, and then a simulation in one step finishes. Moreover, due to independent data of fluid and structural region, the numerical error has occurred frequently. In the present paper, the 1×10^{-3} of convergence criterion employed the integral interpolations on the fluid structure interface is defined. The convergence solutions of last step in iterative calculation is determined the solution of this time step. In Fig. 2-4, the procedures of calculation following this are:

A: Structural solution has been solved. Maximum number of iterations of 250 and $5x10^{-4}$ of force convergence criterion are defined.

B: Then, mesh deformation has been calculated receiving from structural analysis on the interface boundary. Convergence criterion for mesh displacement of 5×10^{-6} m and 100 max-iterations are defined.

C: After update nodal position on the wing surface, fluid solution is solved by using the new boundary condition on the interface between fluid domain and structural domain.

D: Finally, from the solution of pressure profile on the wing, it is interpolated into nodal force for new condition on structural analysis. Herein, this is only one loop, which it depends on the interface load convergence scheme.

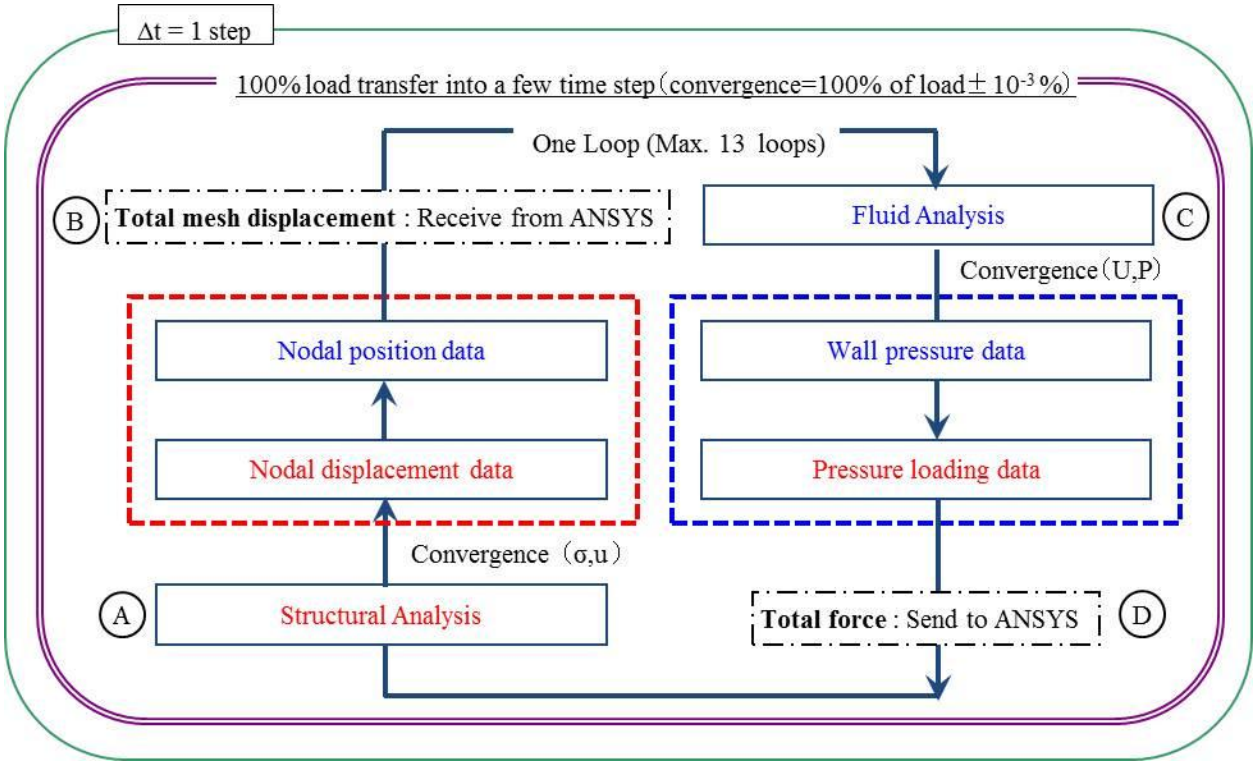

Fig. 2-4 Flowchart of coupling method for FSI simulation

2.3.4 Interface load convergence

For the solution control in external coupling, it can be controlled by two criterions. One is the maximum iteration of coupling step control, and the second is due to the under relaxation factor and convergence target. The under relaxation factor of 0.75 and convergence target of 0.001 are defined. In addition, 13 loops coupling for load transfer is also defined, because it has been a good increment of force acting on structure, and optimizing CPU time. The load increment effects were demonstrated by varying under relaxation factor as shown in Fig. 2-5. These plots show the convergence for each quantity which is part of the data exchanged between the fluid (CFX) and structural (ANSYS) solvers.

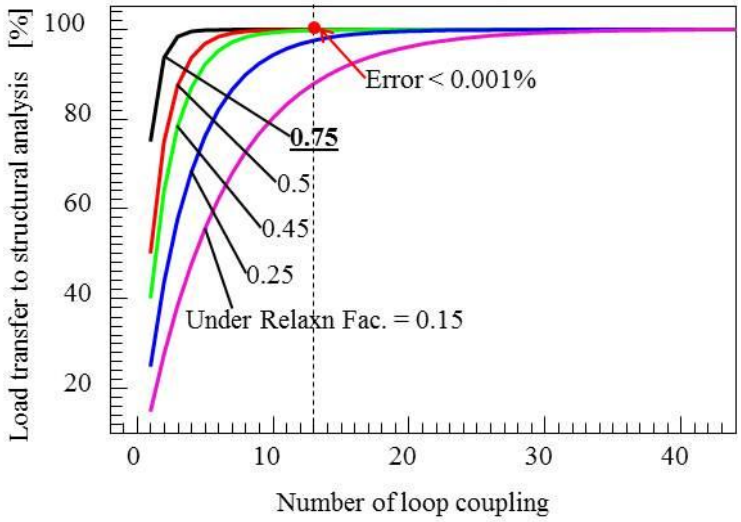

Fig. 2-5 Interface load convergence for FSI simulation

There will always be two plots: ANSYS Interface Loads (Structural) and ANSYS Interface loads (Thermal). The structural plot contains convergence information on forces and displacements, and the thermal plot contains information on temperature and heat flows/fluxes. For each variable (each x-, y-, and z-component of the load is a separate variable), the convergence norm for the data transferred across the interface is given by:

$$\Phi = \frac{\sqrt{\sum \left(u_{new} - u_{old}\right)^2}}{\sqrt{\sum u_{new}^2}} \tag{2-6}$$

where Φ represents the L2 norm of the transferred load, u_{old} is the load component transferred at the last stagger iteration, u_{new} is the load component transferred at this stagger iteration, and the sum is over all the individual load component values transferred (at different points in space). Each quantity is considered to be converged when $\Phi < \Phi_{min}$, where Φ_{min} is the convergence target for that quantity set in CFX-Pre or directly by the multi-field commands in the ANSYS input file (MFC0 command). Convergence of each quantity transferred across the interface is reported as e , where:

$$e = \frac{\log(\Phi / \Phi_{\min})}{\log(10 / \Phi_{\min})} \tag{2-7}$$

and this is the quantity plotted on the ANSYS Interface plots. This implies that each quantity has converged when the reported convergence reaches a negative value. In general, the ANSYS Interface Loads (Structural)

plot will contain six lines, corresponding to three force components (FX, FY, and FZ) and three displacements (UX, UY, and UZ). The x-axis of the plot corresponds to the cumulative number of stagger iterations (coupling iterations) and there are several of these for every time step. A "spiky" plot is expected as the quantities will not be converged at the start of a time step.

2.4 Lift and Drag calculation

The lift force is the force generated perpendicular to the direction of flight for an object moving through a fluid (air). The drag force is the resistance offered by a body that is equal to the force exerted by the flow on the body at equilibrium condition [37]. The drag force arises from two different sources. One is from the pressure (p) acting in the flow direction on the surface of the body (form drag) and the second is due to the force caused by friction [41]. In general, the lift and drag force is characterized by a lift and drag coefficient, defined as:

$$C_L = \frac{L}{A_{wing}\,\frac{1}{2}\rho_a u_a^2} \qquad ,C_d = \frac{D}{A_f\,\frac{1}{2}\rho_a u_a^2} \tag{2-8}$$

where L and D is the lift and drag force respectively, A_{wing} is the wing's planform area, A_f is the frontal area in the flow direction and the subscript a indicates the free stream value. The lift coefficient may be described as the ratio of lift force to dynamic pressure. For the drag force D, it contains the contributions from both the influence of pressure and friction, so which can be written by:

$$D = D_{press} + D_{fric} \tag{2-9}$$

where D_{press} is the pressure drag force and D_{fric} is the friction drag force in the flow direction. The pressure drag, or form drag, is calculated from the nodal pressure values.

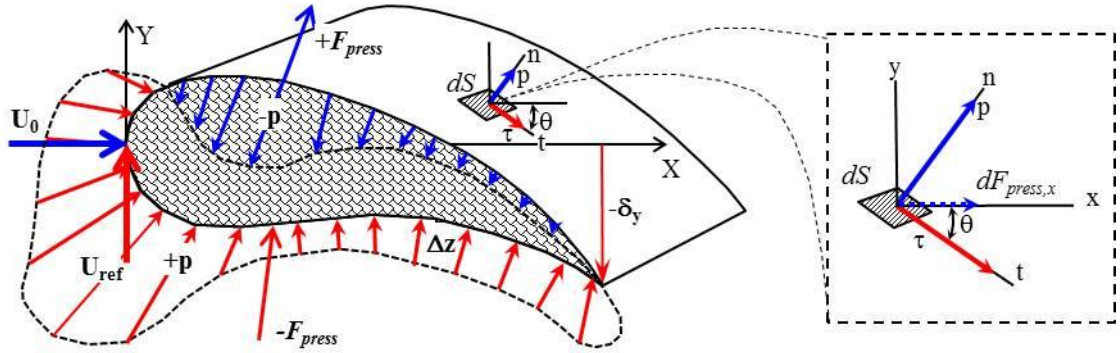

Fig.2-6 Schematic of calculation of pressure surface

For a two-dimensional problem, the solid wall may be a curve or a line and the boundary elements on the solid wall are one-dimensional with two nodes if linear elements are used. The pressure may be averaged over each one dimensional element to calculate the average pressure over the boundary element. It this average pressure is multiplied by the length of the element, the normal pressure acting on the boundary element is obtained. If the pressure force is multiplied by the direction cosine in the flow direction, we obtain the local pressure drag force in the flow direction. Integration of these forces over the solid boundary gives the drag force due to the pressure D_{press}. The viscous drag force D_{fric} is calculated by integrating the viscous traction in the flow direction, over the surface area. The relation for the total drag force in X-direction may be written for a two-dimensional case, which can be computed as:

$$D_x = \int_A ((-p + \tau_{xx})dA)_x + \int_A (\tau_{xy} dA)_x \tag{2-10}$$

where *A* is components of the surface normal **n** as shown in Fig. 2-6.

2.5 Vortex theory

A vortex can be any circular or rotary flow. Perhaps unexpectedly, not all vortices possess vorticity. Vorticity is a mathematical concept used in fluid dynamics. It can be related to the amount of "circulation" or "rotation" in a fluid. In fluid dynamics, vorticity is the circulation per unit area at a point in the flow field. It is a vector quantity, whose direction is (roughly speaking) along the axis of the swirl [50]. Mathematically, vorticity ($\vec{\omega}$) is defined as the curl of the fluid velocity $\vec{u}$, which can be expressed as:

$$\vec{\omega} = \nabla \times \vec{u} \,. \tag{2-11}$$

2.5.1 The vorticity equation

Starting with the Navier-Stokes equation, Eq. (2-2), we can derive equations for the time-dependent vorticity, which can be written as:

$$\frac{\partial \vec{\omega}}{\partial t} + \left(\vec{v} \cdot \vec{\nabla}\right)\vec{\omega} = \left(\vec{v} \cdot \vec{\nabla}\right)\vec{v} - \vec{\omega}\left(\vec{\nabla} \cdot \vec{v}\right) + \vec{\nabla} \times \left(\frac{\vec{\nabla} \cdot \overline{\overline{\tau}}}{\rho} \right) \tag{2-12}$$

Also, in scalar form, the vorticity components are given as:

$$\omega_x = \frac{\partial w}{\partial y} - \frac{\partial v}{\partial z} \qquad \omega_y = \frac{\partial w}{\partial y} - \frac{\partial v}{\partial z} \qquad \omega_z = \frac{\partial w}{\partial y} - \frac{\partial v}{\partial z} \tag{2-13}$$

So, the vorticity magnitude can be computed by:

$$\omega = \sqrt{\left(\omega_x^2 + \omega_y^2 + \omega_z^2\right)} \tag{2-14}$$

In SI unit, it unit is [s^-1]. Especially, one way to visualize vorticity, instantaneous vorticity (rest of the flow removed) particle would be rotating, rather than just moving with the flow (vorticity). Thus, finite volume in the flow is deformed which indicate a change in shape and/or size of the volume from initial or undefromed configuration to a current or deformed configuration.

2.6 Velocity vector and strain rate tensor

For incompressible flow, all three-dimensional flow topology can be classified in terms of the second and third invariant (see in Appendix D.4). To describe how fast the velocity gradient changes, the second invariant, Q, of the velocity gradient is can illustrate, which is defined as:

$$Q = \left[\frac{\partial v}{\partial y}\frac{\partial w}{\partial z} - \frac{\partial v}{\partial z}\frac{\partial w}{\partial y}\right] + \left[\frac{\partial u}{\partial x}\frac{\partial v}{\partial y} - \frac{\partial u}{\partial y}\frac{\partial v}{\partial x}\right] + \left[\frac{\partial w}{\partial z}\frac{\partial u}{\partial x} - \frac{\partial u}{\partial z}\frac{\partial w}{\partial x}\right] \tag{2-15}$$

CHAPTER III

Deformational Displacement

This chapter deals with the wing's kinematic effects to the flow field around the wings and their aerodynamics. In order to evaluate the deformation effects, hence these results on flapping rigid wing should be clarified first. After that, it will be used to be compared with the flapping elastic wing's results.

3.1 Flapping robot's wing

3.1.1 Flapping wing's characteristics

The both flapping rigid wing used in the fluid dynamic analysis and the flapping elastic wing used in the structural analysis, are same dimension with a real flying robot wing in experiment. The wing structures are defined as having the main spars and membrane part, which the main spar is the carbon rod material and the membrane is the paper material as shown in Fig. 3-1(a). The haft wingspan (R) and chord length(c) are 120 and 80 cm, respectively.

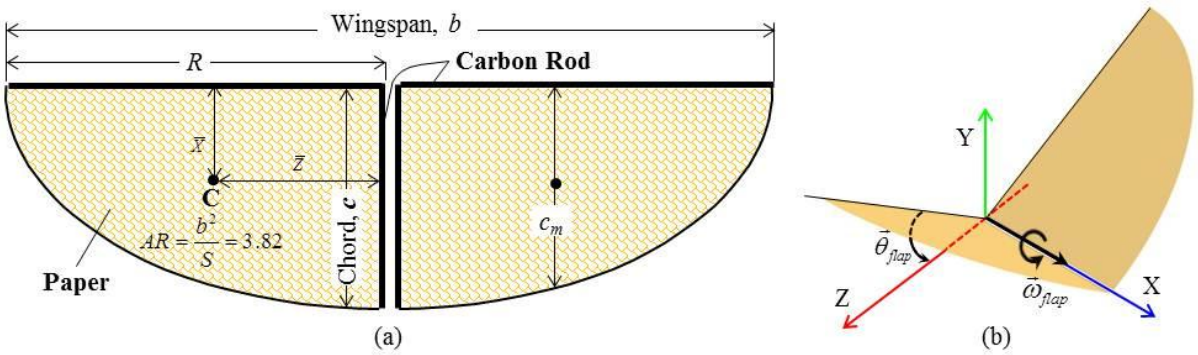

Fig.3-1 Wing's characteristics, (a) Wing structures, (b) Wing's motion

3.1.2. Kinematic motion of flapping robot's wing

For the kinematics equation of flapping robot's wings, which is referred form real motion in experiment. It has been similarly the sinusoidal oscillations as shown in Fig. 3-1(b). It is probably the most common form of periodic oscillation found in real life biological locomotion [56]. The time-dependent flapping angle and angular velocity are defined as [12]:

$$\theta_{flap,x} = [A_\theta]\sin(2\pi f(t+t_0)+\varphi_\theta)-\theta_0 \tag{3-1}$$

$$\omega_{flap,x} = [A_\omega]\cos(2\pi f(t+t_0)+\varphi_\omega) \tag{3-2}$$

where, A_θ and A_ω are the flapping angle and angular velocity amplitude (20 degree), f is the flapping frequency (about 10 Hz), t_0 is the initial time of flapping (about 0.01128 sec.), φ_θ and φ_ω are the phase difference of angular velocity(π rad), and θ_0 is the initial angular position (about 12.4 degree). The flapping angle is defined for boundary conditions both of fluid modelling and structural modelling. In the fluid modelling, the wall boundary condition was defined as moving boundary condition with this motion. Also, in the structural modelling, the support condition is defined as being the remote displacement as Eq. 3-1. In this class of methodology, the flow field around the flapping rigid wing is performed with FLUENT 6.3, and the user define functions (UDFs) code is used for solving the wing's motion in CFD simulation.

3.1.3 Moving boundary problem

Most problems of fluid dynamic are a fixed boundary condition. Fluid engineering concerns a flow field (pressure or velocity distribution) or its flow rate over fluid domain analysis. When simulating flows in which the geometry under consideration is moving with time, the generated mesh will need to change to allow for the alteration in the shape of the computational domain. This can be achieved by remeshing the entire domain (as mentioned section 2.1.4) at each time step [57]. Hence, the flow field around moving elastic body [58] has attracted significantly. It is treated as a coupled problem of a fluid and structure. Recently, many fluid-structure coupled problems have been performed through experimental and numerical analysis. For example, one-way coupled analysis considering a small deformation and coupled analysis, in which the elastic deformation is expressed by a function, have been performed [58, 59]. Since, it has been more complicated to clarify the flow phenomena and characteristics of generating dynamic forces. Firstly, simple model of flapping rigid wings immerged in air flow is further illustrated for considering vortex flow structure and producing lift and drag force. Moreover, in hovering flight, thrust-production can be considered by drag force which is equal to the opposite direction of the thrust force as shown in Fig.3-2.

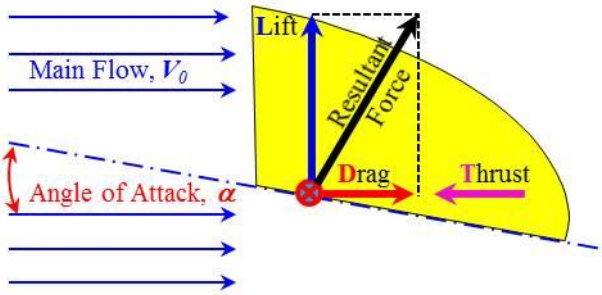

Fig.3-2 Angle of Attack defined in Flow Analysis

3.1.4 Rigid flapping wing modeling for CFD modeling

Firstly, in order to determine what the main effect is in obtaining the thrust force by varying the angles of attack and wing's deformations, hence the vortex structures and unsteady aerodynamic characteristic were considered with varying the angles of attack as 0, 5, 10 and 15 degree. The fluid analysis domain and boundary conditions are shown in Fig. 3-3(a), which is the front, the back, the span length, and the length in vertical direction are given to 2c, 5c, 3c, and 2c, respectively. In simulation, the dynamic mesh method is provided for solving a moving boundary problem. The most popular method for large moving boundary problem is the so-called remeshing method. Due to only tetrahedral cells is needed for this method only, so the mesh at near wing zone is constructed for the deforming fluid zone as shown in Fig. 3-3(b). On the other hand, out of deforming fluid zone is the stationary fluid zone which the mesh does not change for all the times.

3.1.4.1 Initial and boundary conditions

For initial condition, the flapping angle of the wing is specified as 0.0 degree, and after that it is time-dependent of the flapping motion as Eq. 3-1. The inlet velocity condition of 1.5 m/s was defined for the boundary condition, which referred from the real experimental measurement. In experiment, this flying robot can fly as flight speed from about 1.0 to 2.0 m/s. It is low Reynolds number about 8,000, based on the robot's specifications and flight characteristics. For remeshing new mesh in fluid domain, time-step size should be smaller than 1×10^{-4} [s] enough. In particular, the time-step size depends on the mesh sizing and flapping frequency. In addition, to capture the formation of the vortex structure from the wing's leading-edge to behind the wing, thus the flapping cycle should be set more than 6 cycles. Although these are a good condition for the simulation, but it has still been a long time calculation which is about two months. Also, all the conditions are defined for fluid analysis as summarized in Table 1.

Table 2 summarized Specification of the machine performance for calculations. The completion of the simulation also depends on the specification of simulation computer. Especially the parallel calculation method was used for this model completed in two months.

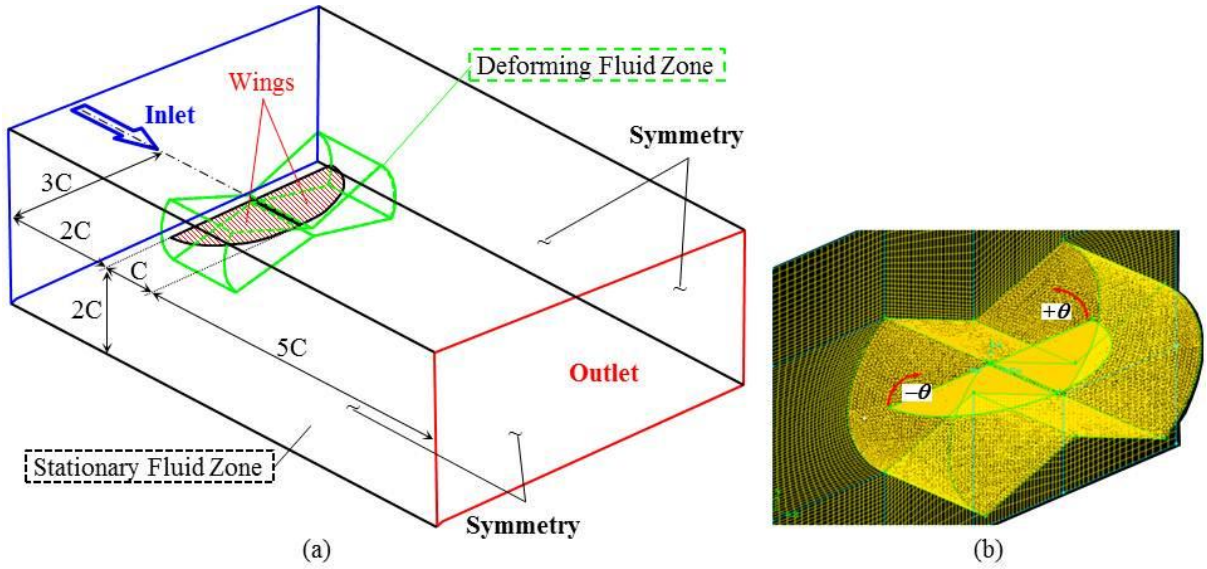

Fig.3-3 Fluid analysis domain, (a) Boundary conditions, (b) Computational grid around the flapping rigid wing (for moving boundary condition)

Table 1 The conditions in CFD for flapping rigid wing

Fluid	*Air*	Inlet	*1.5 [m/s]*
Mesh	*Hexa &Tetra*	Outlet	*0 [Pa]*
Element number	*3,000,000*	Wall	*Symmetry*
Turbulence	*SST k-w*	Angle of attack [deg]	*0, 5, 10, 15*
Re	*8000*	Solution convergence	1×10^{-4}
Iteration	*15*	Time step	1×10^{-4} *[s]*
Flapping cycle	*6*	Cal. time	*Two months*

Table 2 Specification of the machine performance for calculations

PC	*High Performance Computer (HPC)*
OS	*Linux RadHat HLWS 5.5×86*
CPU	*Xeon 2.66 GHz 4core ×2 (Quad)*
Memory	*24 GB*
HDD	*3 TB*
Parallel calculation	*8 CPUs*

3.1.5 Results and Discussion

Recently, many researches have studied about the relationships between momentum changing of fluid flow over immerged body and the generating dynamic forces [53, 60]. This is just one way of the explanation the flow phenomena in fluid dynamics. Description of flow phenomena is explained using variables of fluid flow theory (pressure, velocity). Hence, vortex dynamics is not much more complicated to explain.

Nakata et al. (2011) have studied about aerodynamic performance of hovering flight with flexible and rigid wings. They have found that similar vortex structures and wake patterns are observed in both flexible and rigid wings as shown in Fig. 3-4(a) and 3-4(b) respectively. This is the velocity vectors and contour are visualized at a cutting plane located at 1.5cm away from wing base; and iso-vorticity surfaces (gray) with a magnitude of 1.5 are superimposed in a perspective view [32]. On the other hand, they reported that aerodynamic force acting on the flexible wing has been different with the rigid wing. Hence, the relationship between the flow structure and the force-production has not been clarified fully yet. In addition, vorticity is important in many areas of fluid dynamics, such as approximation the lift distribution over a finite wing by a semi-finite trailing vortex behind it. Hence, I want to consider a vortex structure for predicting the dynamic forces affected by the elastic deformation firstly. Mathematically, vorticity is defined as the curl of the fluid velocity. It can be related to the amount of circulation or rotation in a fluid flow. Otherwise, it is the circulation per unit area at a point in the flow field. Therefore, the location of the circulation related with the position of flapping motion will be clarified first, and then their relation with the drag and lift force will be described either.

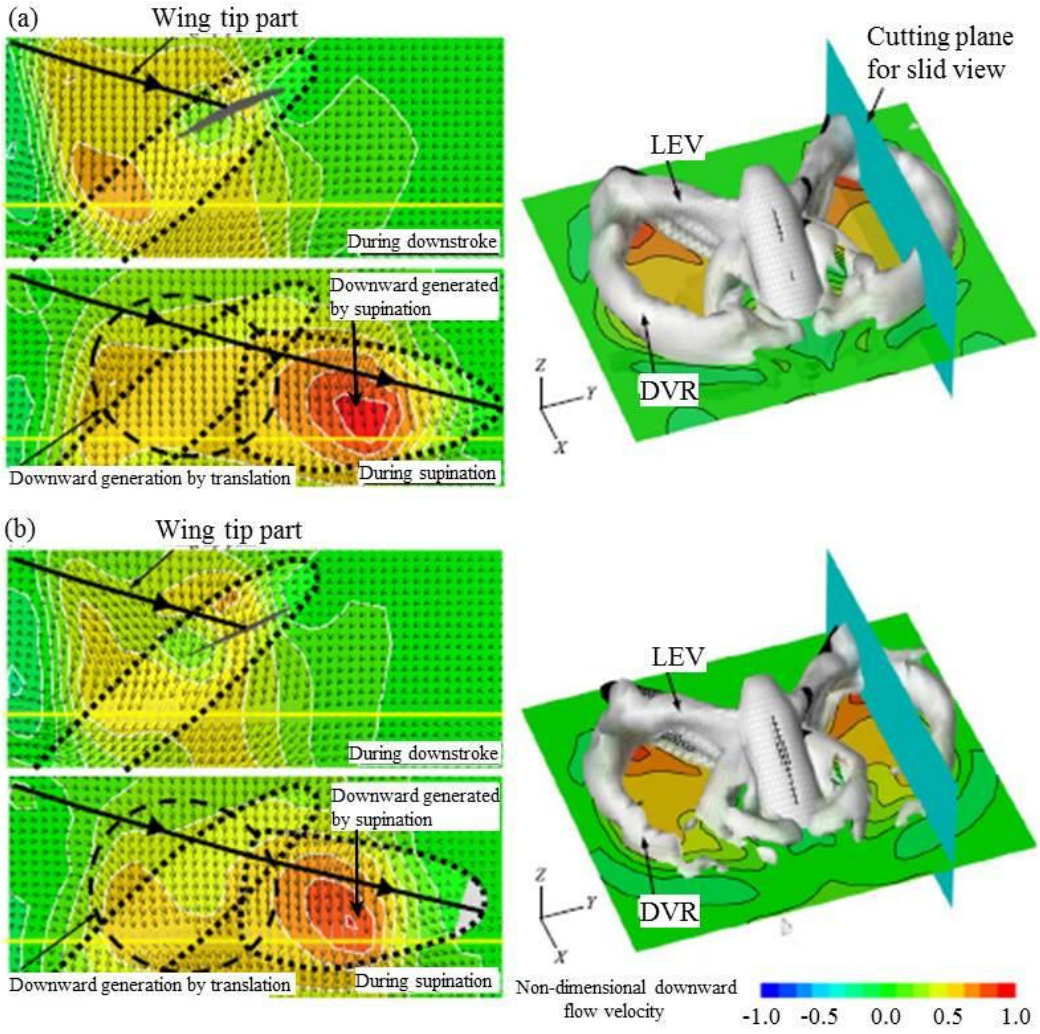

Fig. 3-4 Near- and far-field vortex structure at down-stroke, (a) flexible wing, (b) rigid wing

3.1.5.1 Vortex structure around flapping rigid wing

The flow field around the flapping rigid wings has been captured as a long the flapping motion. Four critical points selected which are bottom- and top-dead point at (A) and (C), and zero angular velocity at (B) and (C) respectively as shown in Fig. 3-5. Therefore, the vortex structure varied with the flapping wing positions was explained by the vorticity contours as shown in Fig. 3-6. This is the iso-surface vorticity of 160 1/s around flapping rigid wing varying, which the wing positions following this are: the top-dead point, moving down-center point, bottom-dead point, and moving up-center point, as shown in Figs. 3-6(a) – 3-6(d), respectively. It has been found, that the high velocities occur at tip-wing and trailing edge, because these positions had the high momentum transfer from the edge of the wing to the wake structure behind the wings. Moreover, the vorticity were largest behind tailing edge and near tip-wings, because difference between velocity gradient in X and Y axis, has been large and growth up from body to tip-wings. The vortices behind the wings are generated by flapping wings, which it could be indicated the behaviours of rotation fluid flow.

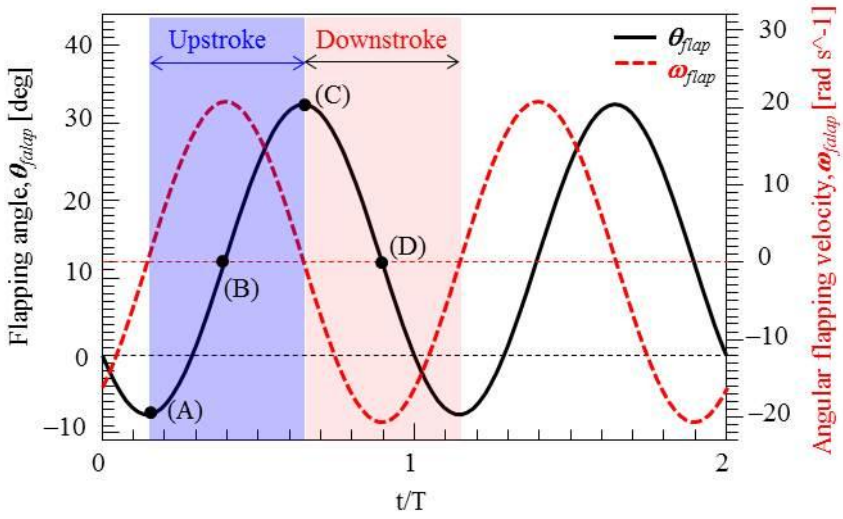

Fig.3-5 Computational grid and Boundary conditions in Structural modeling

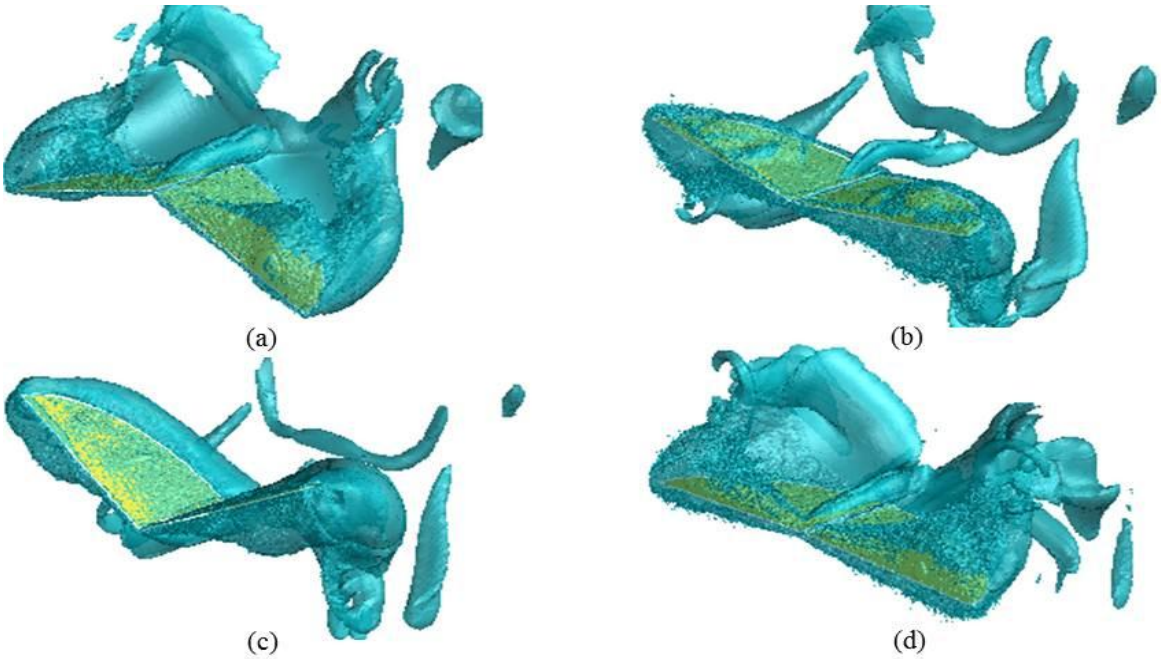

Fig. 3-6 Vorticity around flapping rigid wing varying the wing positions, (a) Bottom-dead point, (b) Moving down-center point, (c) Top-dead point, (d) Moving up-center point

3.1.5.2 Wing's aerodynamic characteristics and variations of angle of attack

Furthermore, we also obtained the time-varying of the drag and lift coefficient as shown in Figs. 3-7(a) and 3-7(b) respectively. It shows that both drag and lift are similar tendency for other angles of attack. It is demonstrated, that the body attack angle was affected to increase drag coefficient very well, as shown in Fig. 3-7(a). Otherwise, increasing angle of attack has been decreased the driving force for flapping flight, because that force is obtained by flapping motion and also itself deformation [20]. In addition, dynamic force depends on the flapping angle position. Hence, it is shown, that the unsteady drag force on the robot's wings occurs, when it is flying by flapping. However, in the term of the lift coefficient, it increases lightly with increasing the attack angle. Also, it cases to make an average lift force in one period flapping motion increasing, as shown in Fig. 3-7(b). This is a good point for flapping flight, because it able to keep the flying robot fly by generating lift force is more than payload weight.

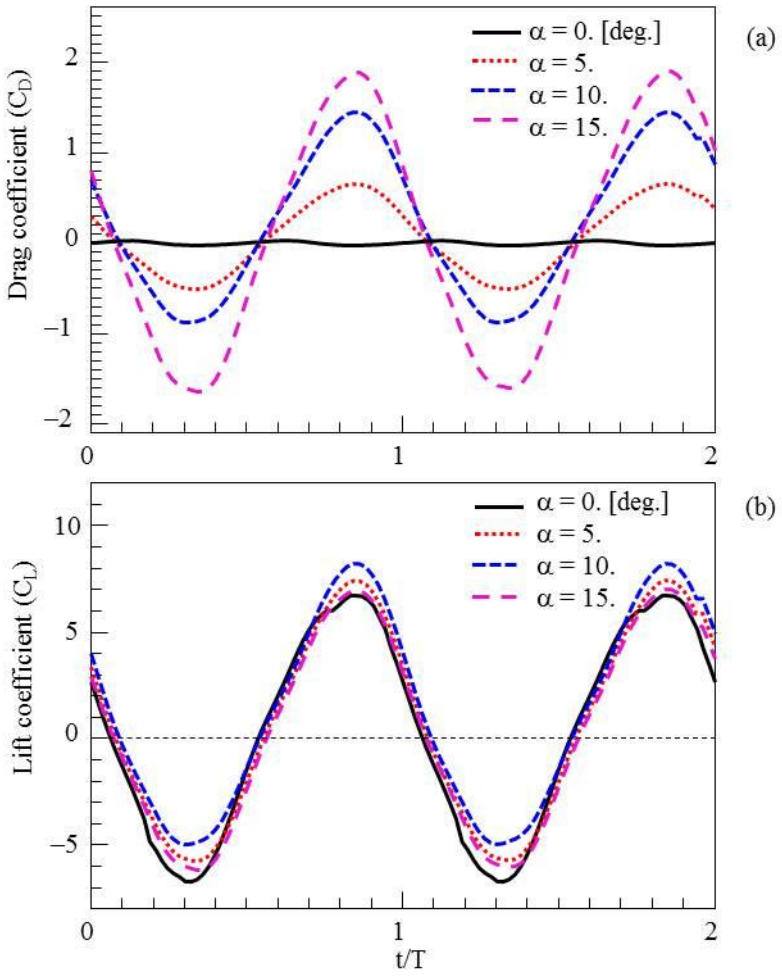

Fig.3-7 Unsteady aerodynamic characteristics, (a) drag coefficient, (b) lift coefficient

On flapping rigid wing analysis, it is shown that wing kinematic (flapping angle, angular velocity, angular acceleration) average flapping effects, Top-dead point, Bottom-dead point, Up-stroke, Down-stroke. Flapping velocity is zero at both top- and bottom-dead point. Hence, lift and thrust are not generated by flapping motion. Only it happens with the flapping rigid wings. However, for the flapping elastic wing has not been solved yet, because the simple flapping wing model has been able to capture for large and complex deformation. Hence, wing's deformation behaviours should be clarified first. I expected that structural analysis would be useful for fluid engineering for considering the elastic deformation effects to obtaining dynamic force.

3.2 Wing modelling for FEM simulation

3.2.1 Wing modelling in structural analysis

In this section, the structural analysis is described to determine an ideal elastic deformation of the wing structures due to some ribs. And also, to understand the mechanisms of wing deformation, the wing models would be varied. Four case studies of the wing structures are varied for modelling as shown in Fig. 3-8. The elastic deformations were obtained for different wing structures and materials, and we show how the elastic deformation and inertial flapping forces affect the dynamical behaviour of the flapping wings.

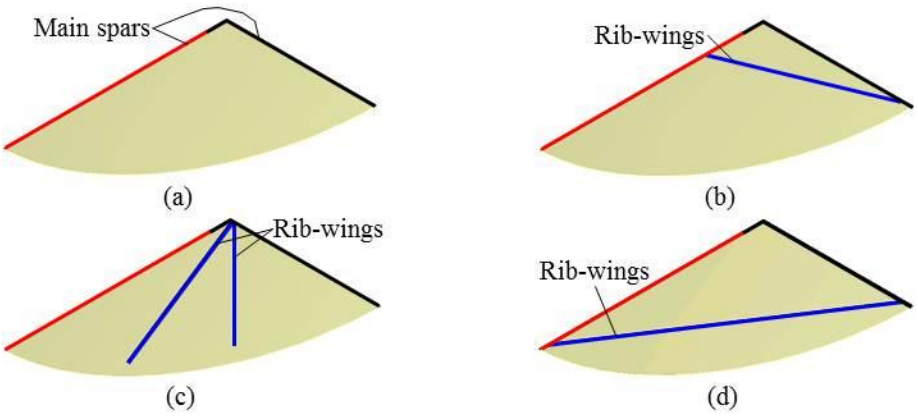

Fig. 3-8 Wing structures for structural analysis, (a) A-Type, (b) B-Type, (c) C-Type, (d) D-Type

In structural analysis, nonlinear structural dynamics problems related to the field of flapping flight have been investigating in the wing's flexibility analysis up to now [61]. In this study, the flexible wings used in the nonlinear elastic model are also varied with Young's modulus and density in three cases as shown in Table 3. Due to the true material properties used to constructing the wing structure is not measured, hence it is defined by referring with the material property region of the carbon rod and paper [18, 28]. For structural modelling, the wing structure is defined as having two parts, which are the wing frame and membrane part. The wing frame is the carbon rod material and membrane is the paper material. The flapping wing motion is specified at the support by Eq.3-1. The computational grid of structural analysis domain is demonstrated as shown in Fig. 3-9(a). The initial and boundary conditions in structural analysis are defined as shown in Table. 3.

3.2.2 Contact problem in structural analysis

Due to the wing consists form two parts, the contact problem is considered. The bonded contact is defined between main wing frame and membrane. In addition, the circular rod of wing frame is simplified as the square rod based on similar second moment of area on rod's cross-second area as shown in Fig.3-9(b).

3.2.3 Initial and boundary condition in structural analysis

For all structural cases, the initial condition of zero velocity and acceleration is defined by damping function (see in Appendix B-1). Based on the continuum mechanics assumption, the dynamic equilibrium of the structure is described by the momentum equation given in a Lagrangian frame of reference (see in Chapter 2). Allowing large deformations, which geometrical non-linearities are not neglible the following boundary value problem, has to be considered [32]. Also, the boundary conditions defined are summarized as shown in Table 4.

3.2.4 Variations of the rib-wing position

There are many parameters affected to the wing's flexibility. One parameter is the rib-wing structures, which it has not been considered fully yet for defining the good wing's deformations. Some researchers have focused for developing the sensors mainly [62, 63]. Based on the hypothesis that if the rib-wing is placed as different position along the wingspan direction. Thus, the maximum deformation at the trailing edge can be specified by the deformation in chord direction at the end of the wing. Fig.3-10 shows the variations of the rib-wing located with the main wing frame, the imaginary of the wing's deformation on the membrane part. One the end of the rib-wing is fixed with the rigid part of the wing frame, which x/c is 0.9375 (75 mm). And, opposite side of the end of the rib-wing is contacted with the elastic part of the wing frame, which the details are summarized as shown in Table 4. Also, the variations of the rib-wing positions are modelled, which the cases of simulations are summarized as shown in Table 5.

The objects of these cases of simulations are to compare how different rib-wing locations affect the wing's deformation, and to be useful for decision selecting the structural model in FSI simulation. Moreover, to optimize CPU-time requirement and solution convergence, the varying of structural models are modelled as shown in Table 6. In typically, the structural deformation depends on the loading, materials, motion, and materialization. By FEM, the realistic structural deformations depend on the loading, flexibility, BC, meshing, and time step size. Hence these parameters will be varied in the structural simulations for considering their effects to the wing's deformation characteristics.

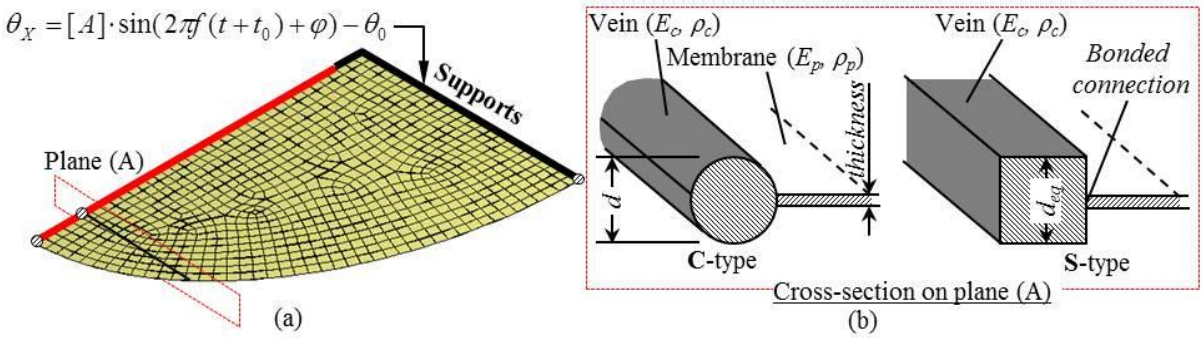

Fig.3-9 Structural modeling, (a) Computational grid and Boundary conditions, (b) The contact condition

Table 3 Material properties of wing structures

Materials	Sizing	Young's modulus, $\boldsymbol{E}$ [GPa]	Density, $\boldsymbol{\rho}$ [kg/m^3]	Poison's ratio, $\boldsymbol{\nu}$
Carbon rod	*∅=0.5, □=0.44*	*133, 350, 533*	*1400, 1500, 1600*	*0.28*
Membrane (Paper)	*(t) =35, 70μm.*	*0.8,1.0*	*600,300*	*0.3*

Table 4 Structural simulation conditions and wing's flexibilities

Structure	*Carbon Rod/ Paper*	Analysis Type	*Transient Structural*
Stiffness behavior	*Flexible*	Supports	*Remote Displacement*
Inertial	g_y*=-9.806 m/s^2*	Node number	*3 ~ 8×10^4*
Initial Velocity	*0. m/s*	Time step, Δt [s]	*0.1, 0.2, 0.5, 1×10^{-3} [s]*
Flapping cycle	*6*	Cal. time	*4 days*

Moreover, the results on the structural analysis will be useful for the fluid engineering in designing of a good elastic wing. Actually, many researches have designed the wing structure which includes the rib-wing only to remain the original wing shape and wing's strength. However, appropriate deformation of the wing can better produce the thrust force.

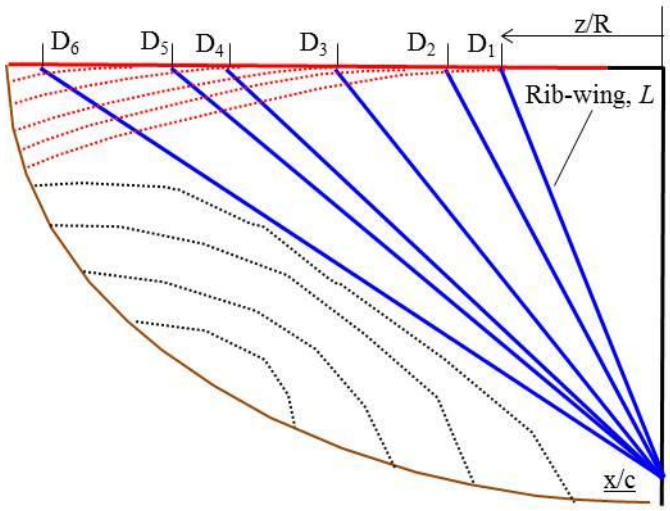

Fig.3-10 Models of the variations of rib-wing location

Table 5 the models of the variations of the rib-wing positions

Model	A	D_1	D_2	D_3	D_4	D_5	D_6
Half-wingspan, *z* [mm]	*0*	*30*	*40*	*60*	*80*	*90*	*114*
Dimensionless wingspan, *z/R*	*0*	*0.25*	*0.33*	*0.5*	*0.67*	*0.75*	*0.95*
Rib-wing length, *L* [mm]	*0*	*81*	*85*	*96*	*110*	*117*	*136*

Table 6 Results of FEM simulation (6 cycles)

Models	*Ec*	*Ep*	Thickness [μm]	Node numbers	Mesh sizing, *Δ* [mm]	Time step, *Δt* [s]	Cal. Time [Days]	Deformation , *δmax* [m]
A (***S***-type)	*533*	*1*	*70*	*3200*	*2*	10^{-3} ~10^{-7}	*6*	*7*
A (***S***-type)	*350*	*1*	*70*	*3200*	*2*	10^{-3} ~10^{-7}	*7*	*9*
A (***S***-type)	*133*	*1*	*70*	*3200*	*2*	10^{-3} ~10^{-7}	*8*	*17*
B (***S***-type)	*533*	*1*	*70*	*5500*	*2*	*0.0005*	*8*	*6.5*
C (***S***-type)	*533*	*1*	*70*	*5600*	*2*	*0.0005*	*8*	*1.5*
D (***S***-type)	*533*	*1*	*70*	*8000*	*2*	*0.0005*	*7*	*6*
A (***C***-type)	*533*	*1*	*70*	*4500*	*2*	10^{-3} ~10^{-7}	*6*	*7.1*
D6 (***S***-type)	*533*	*0.8*	*35*	*50000*	*1.5*	*0.0001*	*12*	*24.5*
A (***S***-type)	*533*	*0.8*	*35*	*28000*	*1.5*	*0.0001*	*14*	*25*
D2 (***S***-type)	*133*	*1*	*35*	*80000*	*1*	*0.0001*	*32*	*35*

3.2.5 Calculation of nodal displacement components

In FEM simulation, nodal data has stored as each node position. For Lagrangian view point, each node on moving body is referred from the origin of global coordinate system. Due to the motion of a flapping wing is assumed like a motion of continuum body, thus its position can be specified by the vector position components as shown in Fig. 3-11(a). Hence, deformed configuration depends on *x*, *y* and *z* position and time motion (*t*). In order to consider only the elastic deformation effects, the current configuration should be subtracted by undeformed wing (flapping rigid wing) at the same time either. Actually, nodal position is calculated from the changing of position referred from initial configuration as shown in Fig. 3-11(b). The nodal position ($\boldsymbol{r}_E$) is defined to be specified each node position as having three components ($r_{E,x}$, $r_{E,y}$, $r_{E,z}$).

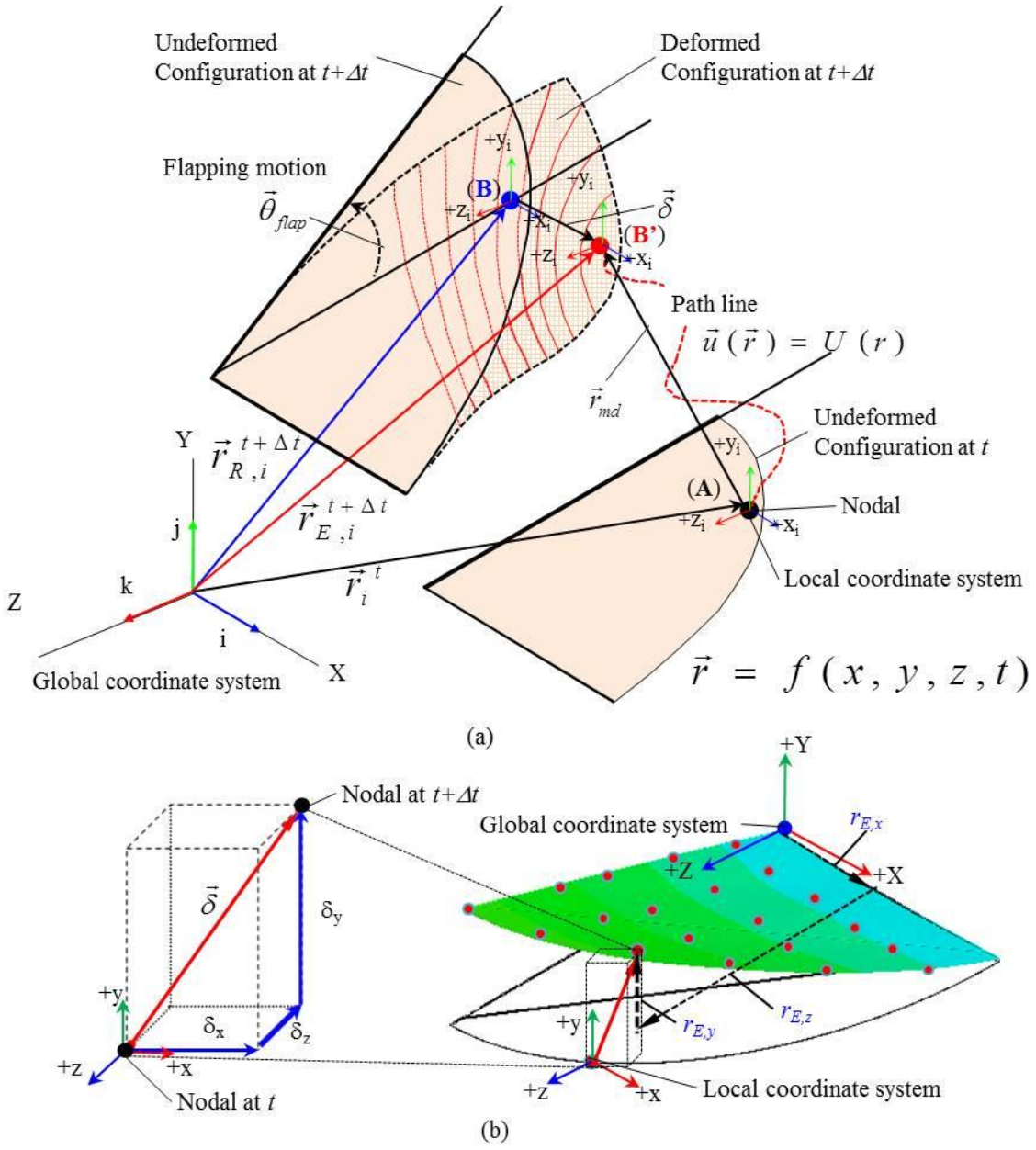

Fig. 3-11 Imaginary of moving elastic wing, (a) Nodal displacement at node i due to flapping motion and wing's deformation, (b) Nodal deformational components

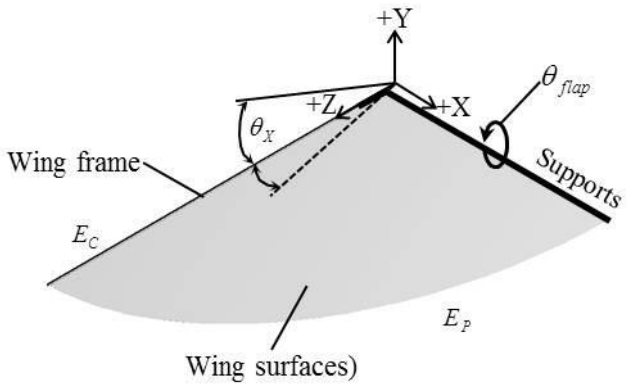

Fig. 3-12 Current flapping rigid wing for calculation the deformational amounts

Fig. 3-12 shows the current wing of the flapping rigid wing (left wing). In scalar form, the local node displacements can be calculated as:

$$r_{Rx,i}^{t+\Delta t} = r_{x,i}^{t_0} \tag{3-3}$$

$$r_{Ry,i}^{t+\Delta t} = [r_{z,i}^{t_0}]\sin(\theta_{flap}) \tag{3-4}$$

$$r_{Rz,i}^{t+\Delta t} = [r_{z,i}^{t_0}]\cos(\theta_{flap}) \tag{3-5}$$

where $r_i^{t_0}$ is the initial displacement of each nodes. So, the displacement magnitude can be computed by:

$$r_{R,i}^{t+\Delta t} = \sqrt{(r_{Rx,i}^{t+\Delta t})^2 + (r_{Ry,i}^{t+\Delta t})^2 + (r_{Rz,i}^{t+\Delta t})^2} \tag{3-6}$$

3.2.6 Calculation of the deformational components (δ)

In order to consider only changing of deformation, the deformation expression is defined by that nodal deformation is equal to the nodal elastic displacement subtracted with the nodal rigid displacement as shown in Fig. 3-13. The nodal rigid displacement is the function of the time-dependent flapping angle, $\theta_{flap}(t)$, which is referred from the global origin point.

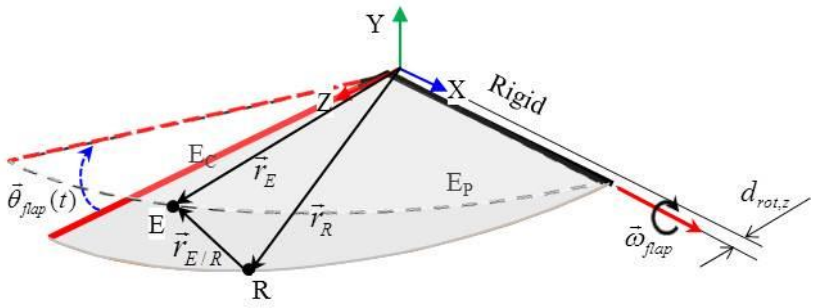

Fig.3-13 Wing's deformation based on flapping rigid wing

Physically, the total displacement consist from that the nodal positions change by flapping motion and the deformation caused by the flexibility. Moreover, the initial wing at current time is calculated as flapping rigid wing, and then the deformational components (δ_x, δ_y and δ_z) can be written as:

$$\vec{\delta} = \vec{r}_E - \vec{r}_R \tag{3-7}$$

where $\vec{\delta}$ is the deformation amount, which is vector value, $\vec{r}_E$ is elastic deformational displacement, and $\vec{r}_R$ is the rigid displacement based on flapping motion.

Also, in scalar form, the deformational components are given as:

$$\delta_x = r_{md,x} \tag{3-8}$$

$$\delta_y = r_y + [(r_z - r_{md,z})(1 - \frac{d_{rot,z}}{|r_z - r_{md,z}|}) \cdot \sin(\theta_{x,flap}) \tag{3-9}$$

$$\delta_z = r_z - [(r_z - r_{md,z})(1 - \frac{d_{rot,y}}{|r_z - r_{md,z}|}) \cdot \cos(\theta_{x,flap}) + (r_z - r_{md,z})(\frac{d_{rot,z}}{|r_z - r_{md,z}|})] \tag{3-10}$$

where r_{md} is the total mesh displacement from the point (A) to the point (B'), as can be seen in Fig. 3-11(a), r_y and r_z are the current nodal displacements referred from the global coordinate, $d_{tot,z}$ is the distance from global origin to the rotation axis ($d_{rot,z}$= 0.002 m is defined) as shown in Fig. 3-13.

So, the deformation magnitude of each node on the wing surface can be computed by:

$$\delta = \sqrt{(\delta_x^2 + \delta_y^2 + \delta_z^2)} \tag{3-11}$$

To consider only the deformation effects on wing, the result from Eq. (3-11) has especially been one way to evaluate only deformation occurred, which the flapping motion does not affect to the nodal deformation. According to it is derived from Eq. (3-7), thus it means that is the different wing position between the flapping elastic wing and rigid wing. Most researches have used the wing displacement amount to consider the deformation effects on a flow structure and aerodynamic forces. Hence, it has been difficult to consider the main effect because of the physical amount of the displacement is dominated both the elastic deformation effect and the variables of the flapping wing motion such as flapping amplitude, flapping frequency or wing configuration. Therefore, the deformation amount is better variable for considering only the deformation effects.

3.3 The principle of DRR

For moving elastic body, to fine some parameter for descriptions the physical meaning of the deformation behaviors, hence we have defined the deformation region ration, which named DRR (indicated with displacement,δ), its unit is m^3. And also, it can consider as dimensionless parameter, which calculated by the ratio of volumetric deformation with the volume of the wing area moving.

3.3.1 Physical meaning

Volumetric deformation is closely related to the volume flow of the moving surface, since both quantities are proportional to the deformation area, $A_{y,i}$, (in the case of flexible wing) and the deformation value, $\delta_{y,i}$, as shown in Fig. 3-14. DRR is equal to the summation of each deform region divided by the root wing surface moved. Therefore, by looking at the variation of during flight, it has been possible to determine how the elastic deformation will vary and in particular when it will reach its maximum value. This point of maximum dynamic thrust is often related to as max DRR multiply the different surface pressure. Especially, it has been a critical parameter to predict the thrust coefficient for considering wing efficiency.

3.3.2 Definition of DRR

Volumetric deformation is defined by:

$$DRR = \sum_i A_{yi,deform} \cdot \delta_{y,i} \tag{3-11}$$

where: $A_{yi,deform}$ is the split deformation area on one side of wing surface, $\delta_{y,i}$ is the deformational displacement which is calculated by Eq. 3-9.

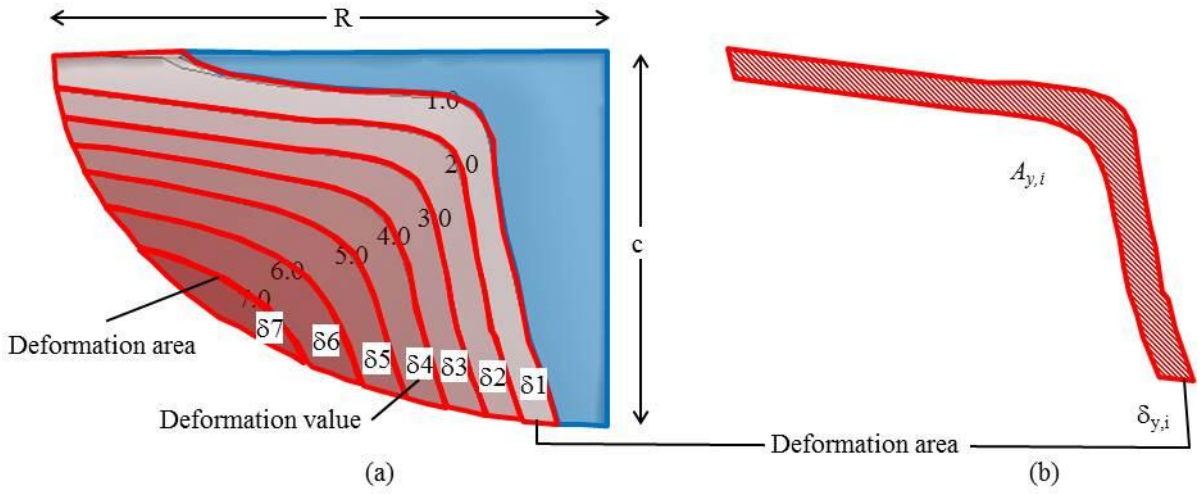

Fig.3-14 Calculation of DRR, (a) Deformation distribution for calculating DRR, (b) The split area each defamation value

Let's DRR_{yi} is the dimensionless area ratio, which is calculated by each deformational area to the wing surface as Eq. 3-11. The dimensionless deformation area is defined as:

$$DRR_{yi} = \frac{A_{yi,deform}}{A_{wing}} \tag{3-13}$$

where $A_{yi,deform}$ is the each deformational area, and A_{wing} is the original half-wing area. Let's consider all deformational area. Now I will give very important definition as main definition of this section. The dimensionless deformation, which compared with wingspan (R) of three shapes, can be expressed as:

$$\delta_{yi}^{*} = \frac{\delta_{yi}}{R} = \frac{\delta_{yi}}{c_m} = \frac{\delta_{yi}}{\sqrt{A_{wing}}} \tag{3-14}$$

So, the total DRR over the wing surface deformation can be found as:

$$DRR = \sum_{i} \left[\frac{A_{yi,deform}}{A_{wing}} \cdot \frac{\delta_{yi}}{\sqrt{A_{wing}}} \right] \tag{3-15}$$

In general dimensionless DRR variable, it can be related with the characteristic of the wing surface (A_{wing}). Thus, from Eq. 3-15, it can be reduced as general form as:

$$DRR = \frac{\sum_{i} (A_{yi,deform} \cdot \delta_{yi})}{A_{wing}^{1.5}} \tag{3-16}$$

Let's note that this is a general definition which works in many different wing shapes. It works not only in square shape but also other shape. Moreover, it can be used with an infinite wing (2D analysis), by calculating the wing area and deformational area per unit wingspan. For example, it is the analysis of 2D elastic aerofoil. The original half-wing surface for the very thin-membrane of the wing can be defined at the following assumption, $S \cong 2A_{wing}$. In Fig. 3-14(a), each split area is defined as being $\Delta\delta_{yi}$ of 1 mm. The blue area is δ of 0 to 1 mm, so $\delta_{y1,ave}$ of 0.5 is used for calculating DDR_{y1} as shown in Figure 2-14(b). Hence, the accuracy of DRR calculated has depended with division of the deformation scale ($\Delta\delta$). Moreover, the general expression of DRR can be applied to the other wing shape by using their wing surface like in Fig. 3-15.

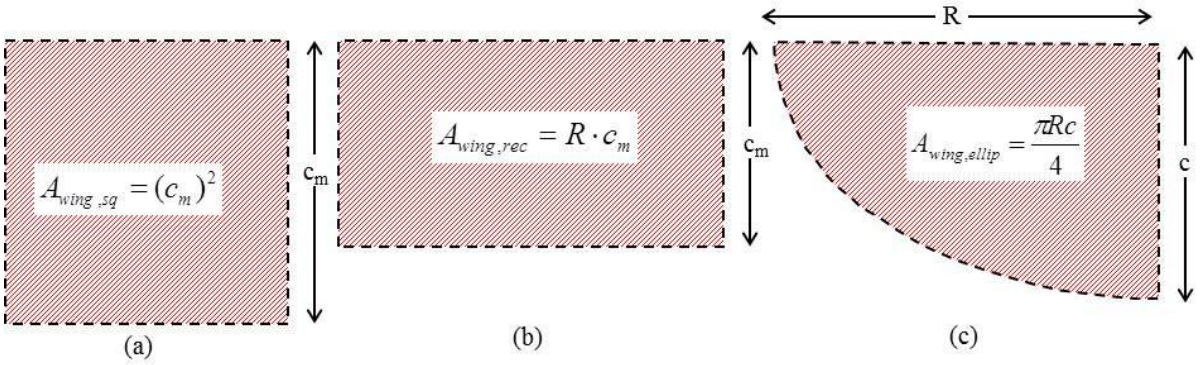

Fig.3-15 An original shape of half-wing area (A_{wing}) of, (a) Square, (b) Rectangular, (c) Half-ellipse

3.3.3 Results and Discussion

In this section, the FEM results are obtained from the structural analysis for some case studies. To start with the study of the deformation mechanisms of the wing's deformations, which the symmetric problem is assumed, following these results is presented. The deformational mechanisms can be described by the wing's surface displacements, and also the wing's deformations, which calculated by subtracting of the total elastic displacement (r_E) and the total rigid wing displacement (flapping rigid wing motion), are considered. Thus, the deformation results are further demonstrated as follows below.

3.3.3.1 Wing's flexibility and positions

From structural analysis results, three types of wing structures have selected for evaluating the deformations as shown in Fig. 3-16. The contours of the elastic deformations on the wing structures are plotted, in order to clearly show the elastic deformation variations. The key feature observed here is the presence of two regions of the deformations that rapidly change as the wing positions. The results demonstrated the deformations of A-, C- and D-Type wings at the top-dead and bottom-dead points, which Young's modulus of the car bon rod of 133 MPa as shown in Figs. 3-16(a) and 3-16(b), respectively. It shows that the elastic deformation strongly depends on the positions of flapping angles. Besides, the elastic deformations depend on the structural flexibility (E) very well as shown in Fig. 3-17. Each wing structures are fixed the global second moment of area (I) by using the same dimension of wing structure. In addition, it illustrates that not only the deformations on the main spar is decreased, but also the deformation on the membrane at the trailing edge. Due to the effects of the main spar strength at trailing edge reinforces on the membrane, hence the deformation is decreased either. Also, the maximum deformations have occurred following this, 15, 9, and 7 mm with Young's modulus as 133, 350, and 533 MPa, respectively (see in Fig. 3-17). Furthermore, the positions and length of some ribs attached with the main spars are very strong effects with the deformation on the membrane, because the carbon rod connected with the membrane is high flexibility (EI). Hence, the maximum deformation is decreased by some ribs as comparison with the original wing (A-Type wing).

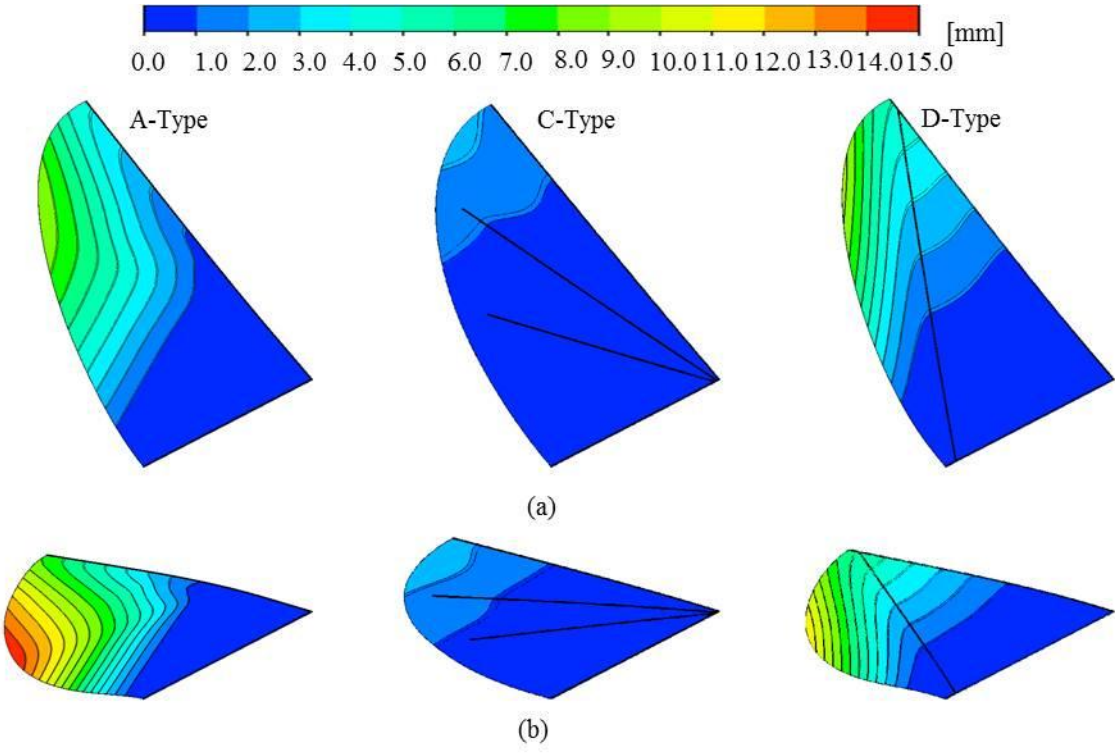

Fig. 3-16 Deformation as varying wing positions, E_c=133, (a) Top-dead point, (b) bottom-dead point

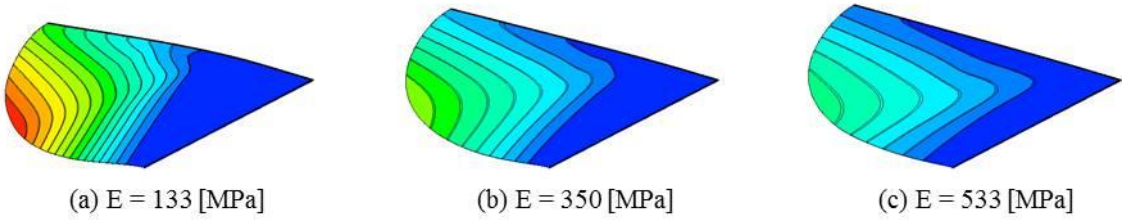

Fig. 3-17 Max-Deformation as varying Young's modulus, on A-Type wing

3.3.4.2 Rib-wing effects

In order to specify the elastic deformation region, the way of rib-wing structure is illustrated. It is found that large deformation region is similar in wing A, B and D, qualitatively. It has occurred at near middle trailing, because is far from the wing frame and rib-wing supports. On the other hand, large deformation has occurred at near the end of wing in only wing C, because the rib is fixed at the rigid support (A), but it is free end, which is very close with free trailing edge as shown in Fig. 3-18.

This is only demonstrated as being the instantaneous deformation. However, the deformation depends on both the local position and time motion. Hence, the deformation based on the magnitude, position and time motion have to be considered, and after that it will be useful for prediction of the elastic deformation effects to generate the driving force. The max-deformation is possible to determine how much the deformation will affect to obtain dynamic forces. Hence the max-deformations are further plotted in Fig. 3-19, corresponding with Fig. 3-18. And, it might be a guide line to select the FEM wing's models for further FSI simulation.

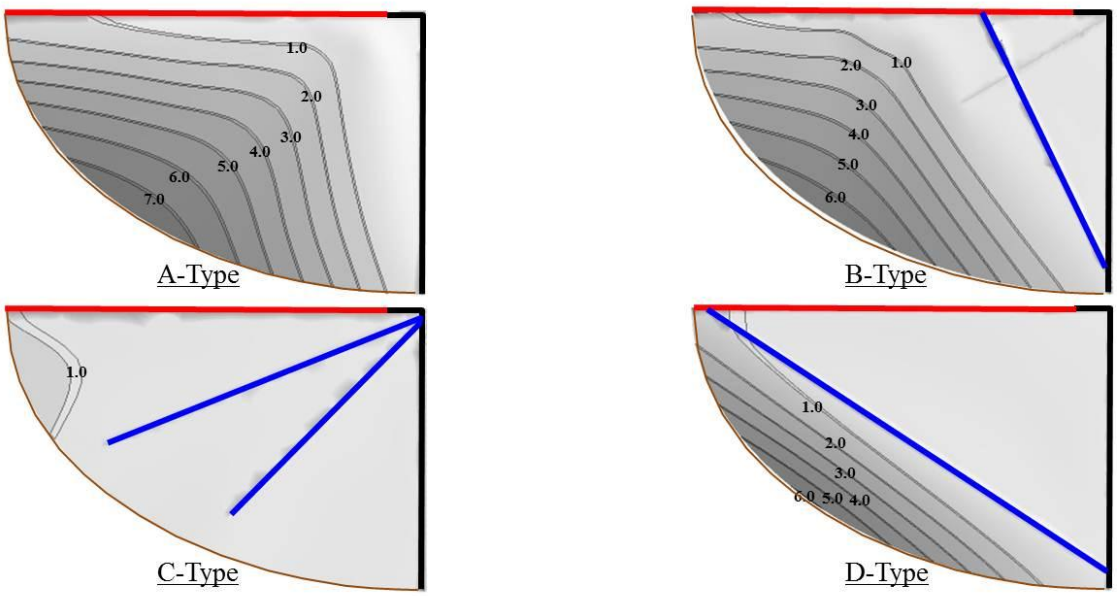

Fig. 3-18 Deformation distribution due to the rib-wing structure, t/T = 0.85, E =533 GPa.

3.3.3.3 Local max-deformation on wing surface

It is found that the max-deformation has occurred at the point A on the trailing-edge as shown in Fig. 3-19. Hence, these points on each wing structure are focussed for evaluating the flexibility effects to the elastic deformations. Due to there are three components of the deformation, all deformation components are calculated and plotted as shown in Fig. 3-20. It is shown that Y-component deformation is mainly affected to the deformation magnitude, because this flapping motion is rotation only about X-axis. In addition, only wing B and D have 4 peaks of high deformation because of the periodic deformation at trailing edge has occurred. On the other hand, it has 2 peaks of high deformation in cases of wing A and C, because they have the trailing edge deformation motion as being same with flapping motion.

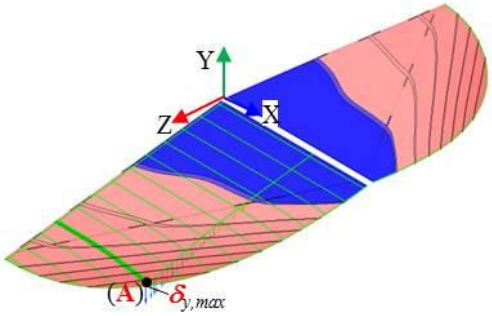

Fig.3-19 Max-deformation at TE, FEM simulation

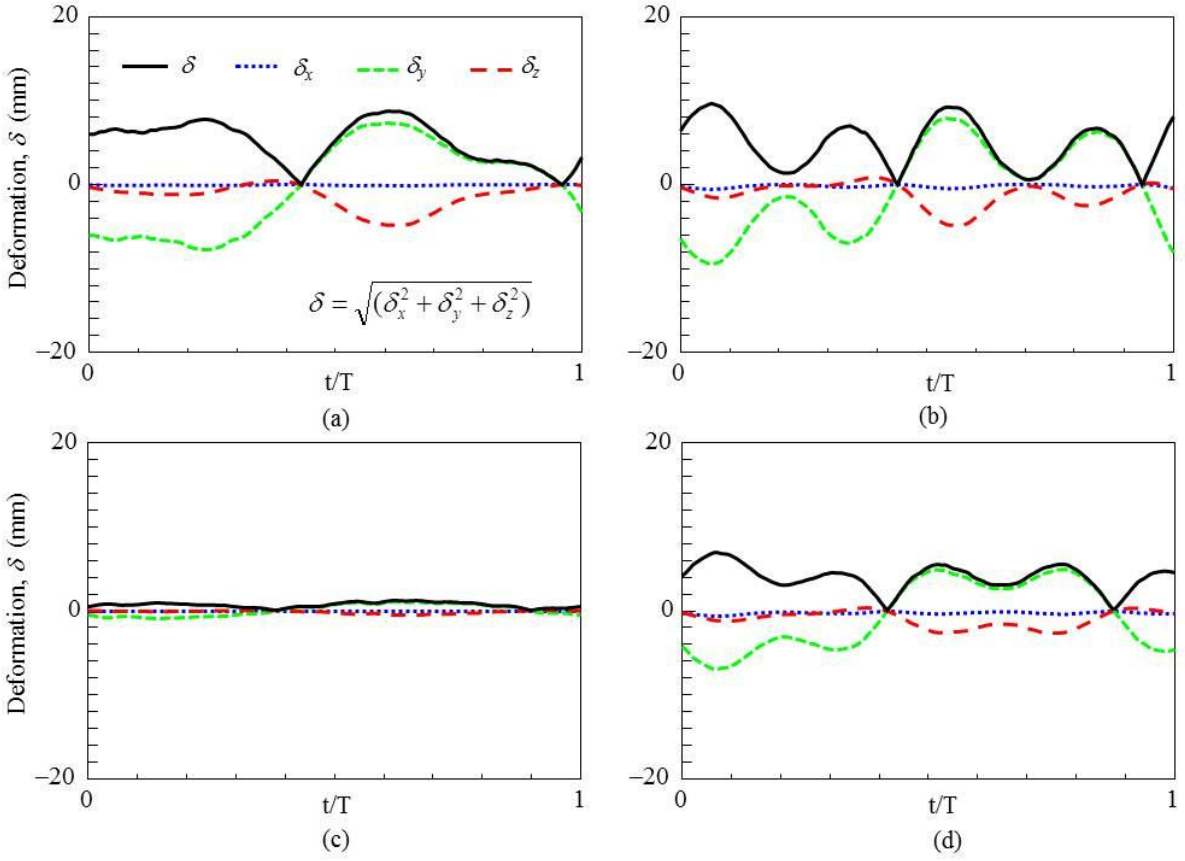

Fig.3-20 Deformational components of max-deformation at TE, FEM simulation, (a) Wing A, (b) Wing B, (c) Wing C, (d) Wing D

3.3.3.4 DRR variations and wing's deformation behaviors

According to DRR's principle which is firstly proposed for evaluating the elastic deformation effects, thus their results will be discussed in this section. The DRR results of each wing structures are plotted by Eq. 3-16 and demonstrated as shown in Fig. 3-21(a). This is DRR as a long with flapping motion. It is found that DRR has been similar tendency with the max-deformation (see Fig. 3-20) qualitatively, because it is calculated by the production of the deformation magnitude as shown in Fig. 3-21(b). Moreover, DRR can be indicated with the deformation quantity affected by the flexibility due to the rib-wing, which is one way of how to define the location and magnitude of the deformation. And also, DRR can evaluate the order of magnitude of the deformation quantity. For the results of the rib-wing structure effects, the results of the wing A (without rib-wing) and wing D (within rib-wing) were adopted to describe how it is affected (Fig. 3-21(b)). It is found that the rib-wing has dominated the deformation through max-deformation at trailing-edge. Especially, the number of the deformation peak has been varied by the trailing-edge deformation behaviour.

However, DRR's principle is just new idea which is proposed for considering the elastic deformation effects on the thrust-production. It also can be applied for both 2D and 3D elastic deformation problems. In addition, the wing's structure is also dominated the DRR's characteristics of the wings. Hence, it will be useful for further considering the deformation effects to the thrust-production in the flapping flight, which it will be death with in next chapter.

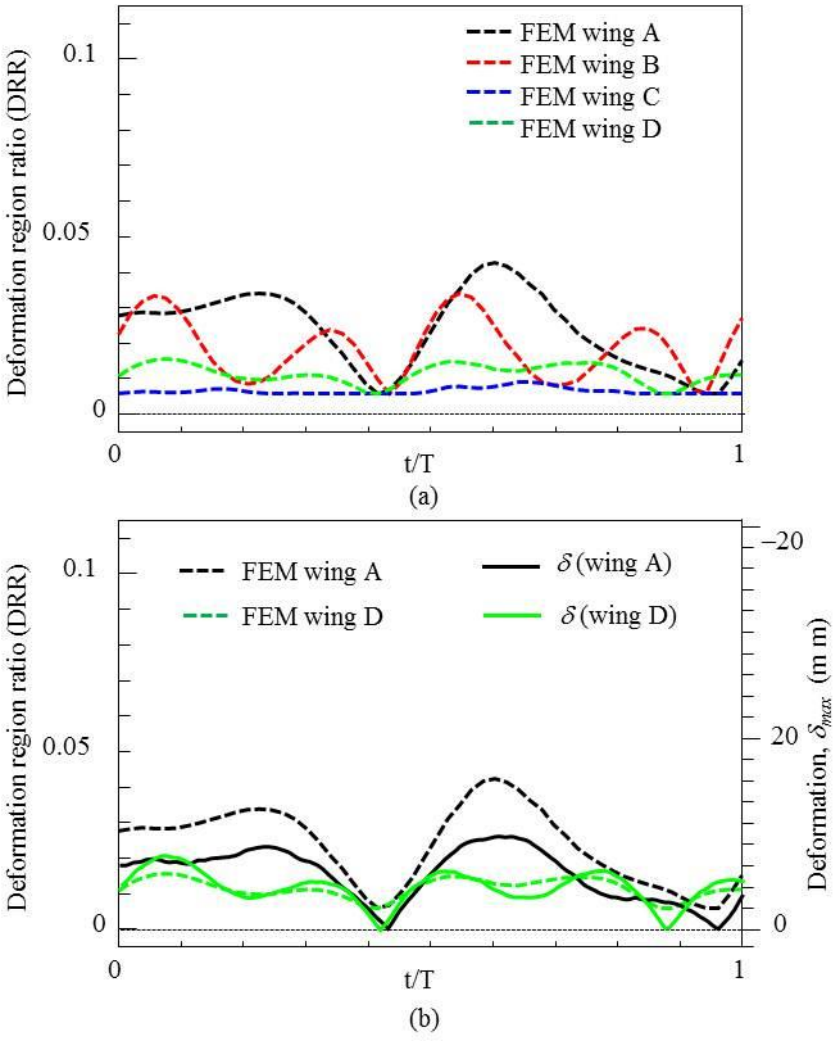

Fig.3-21 DRR variable for each wing type, (a) Dynamic DRR, (b) DRR related with deformation

3.4 Summary

In order to evaluate the deformation effects, the results on flapping rigid wing have been performed to clarify the mechanism how the flapping wing deforms and their effects to the flow structure. The flapping rigid wing was firstly modelled to use its results to compare further with the flapping elastic wing's results. CFD analysis for flapping rigid wing and FEM analysis for flapping elastic wing have been simulated.

In case of flapping rigid wing analysis, the flying robot obtains lift by flapping itself wings, which caused to making vortices also. In particular, a pair of large-scale vortices is formed on the wing tip. It is found that the flapping angular velocity is strongly affected to produce the lift force. On the other hand, the angle of attack is slightly affected to increase lift, but is strongly affected to increase drag. Although, the maximum angular velocity occurred at the flapping angle of 12 degree, it has not only affected to produce low drag and high lift force. However, at the top- and bottom-dead position of flapping wing angle, the drag and lift is still generated which may cause of the effects of the unsteady leading edge vortex over the entire wing. In addition, increasing the angle of attack is only useful for generating average lift force, on the other hand, it has decreased the driving force (positive drag) either. For simple model, the simulation results of rigid flapping motion have only agreed with experimental results

In cases of flapping elastic wing analysis as largely and complexly deforming wing, the wing's deformation making as function has been unable to predict its deformation closely. Actually, in order to perform the real deformation of flapping wing based on actual application by simulation, it has needed both the actual initial and boundary conditions and real material properties. Hence, finite element method (FEM) is achieved to predict large deformation. For structural analysis as well as FEM, there are many ways to make itself wing deformation such as material properties, structural sizing or rib-wing structures. It has been found that, the maximum deformation has occurred at the wing's trailing edge due to some rib-wing. And also, the period and frequency of the wing's deformation motion have been dominated by the wing's mass and flexibility, which cause both the amplitude and initial phase of the flapping motion.

Moreover, it has been demonstrated that, some rib-wing structures attached with the main wing frame of the wing structures can control the wing deformations, which can be evaluated by the DRR variable. Although, DRR's principle was proposed to consider how the deformation affects to thrust-production and to evaluate the order of magnitude of the deformation quantity. However, it has needed both the realistic deformation and thrust-production result to clarify these research aims. Only sstructural analysis has not been good sufficient for considering the elastic deformation effects, because it cannot predict the realistic deformation of the wing, and has not obtained thrust force either. However, it is useful to find the appropriate structure model and to clarify some structural deformation mechanisms. They will be used in further numerical simulations based on fully FSI analysis, which will be described in next chapter.

In particular, it has noted that, by comparing with experimental results, the simulation results have been too different, because initial force is only considered and also they are different in the material properties, (which the deformation behaviour is illustrated as shown in Fig. B-5(a) and B-5(b) which is the experimental and simulation result, respectively). However, the simulation way is better to consider the elastic deformation effects to generate the dynamic thrust force than experimental approach for small wing system, because both thrust force and momentum flow data cannot be obtained by experiment well yet.

CHAPTER IV

Modification of DRR

To find the realistic deformation of the structural phenomena and understand the mechanisms of its deformation, the fluid-structure interaction (FSI) simulation is useful for solving fluid-structure coupled problems. FSI is new way for fluid engineering. For numerical framework of flapping elastic wing simulations, the brief description of the fluid and structural dynamic approaches for the aeroelastic analysis of flapping flexible wing is presented. From these, an aeroelastic framework is developed for the analysis of low *Re* flows and their interactions with flexible flapping wing [19, 32, 38, 45, 53, 59, 63and 64]. The governing equations of fluid are the unsteady, incompressible 3-D Navier-Stokes equations and the continuity equation, which are all most same with the simulation of the flapping rigid wing (see in chapter 2).

Especially, the aim is to clarify the research hypothesis how DRR can predict the dynamic thrust force on the wings with deformation effects. Due to FEM can perform the physical deformation only, hence consideration of thrust-production needs the flow field solutions (pressure, velocity) significantly, as relations shown in Fig. 4-1. Hence, in this section, FSI approach will be employed to be completed in the research aim.

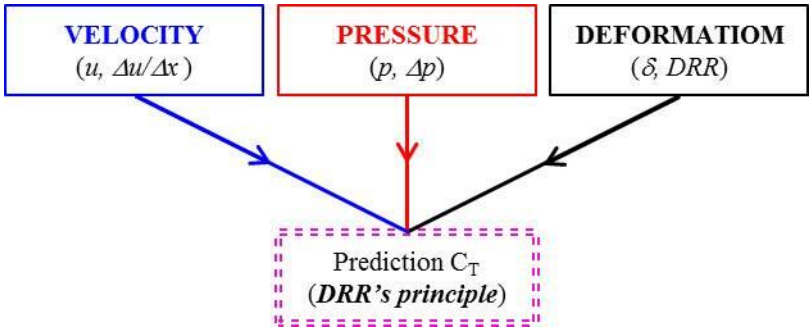

Fig. 4-1 DRR's principle for a fluid application

4.1 Wing modelling for FSI simulation

4.1.1 Wing modelling

In FSI simulation, two cases of the flapping wing structure have been adopted for calculation to compare the results from FEM simulations to consider the elastic deformation effects to generating dynamic thrust. For the validation of present DRR expression for obtaining thrust results the following two cases were considered as shown in Fig. 4-2. Also, its deformation results will be used to verify the principle of DRR.

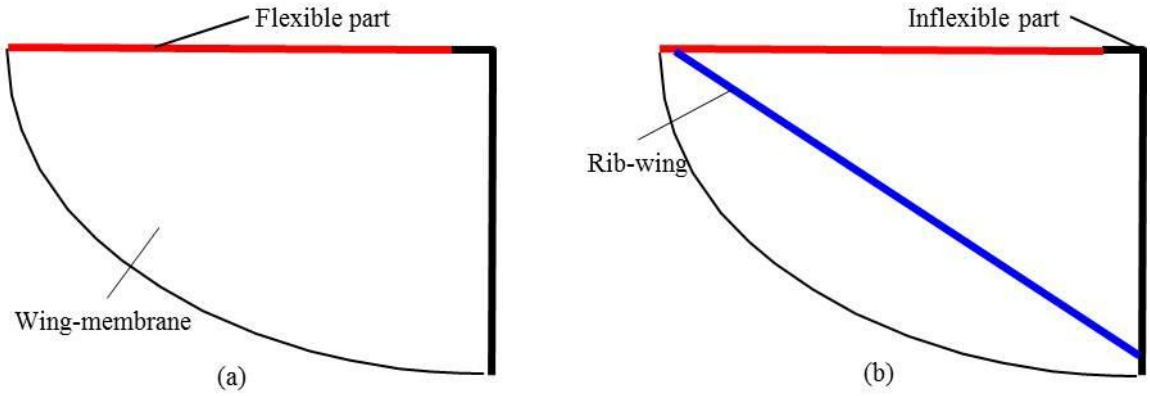

Fig. 4-2 FSI wing models in CSD, (a) wing A (no rib), (b) wing D (within rib)

The flexible wings modelling for FSI simulation are the wing structure without some rib-wing (Fig. 4-2(a) and within the rib-wing (Fig. 4-2(b). They have been adopted because it can compare the different physical deformation as well, which are the wing A and D. It is caused by both the wing's flexibility and rib-wing structures. The wing C had not been simulated because it has been very small deformation, also for the wing B is because it has been similar deformation with the wing A.

4.1.2 Initial and Boundary condition for FSI simulation

4.1.2.1 Wall interface

In Eulerian approach, at a cell face that is the interface between the wing surface and fluid domain (Fig. 4-3(a)), the normal velocity $u_{\perp}$ disappears so that only the pressure terms in the flux remains. This boundary condition can be implemented by extrapolating the pressure from adjacent cell. In the N-S calculations, both $u_{\perp}$ and $u_{//}$ disappear at the wall boundary and pressure is extrapolated from inside, which is assumed as no-slip condition. In FSI simulation, the fluid forces acting on the wing surface lead to the nodal displacement on the wing surface, which depends on the computational grid generated as shown in Fig. 4-3(b). Otherwise, the computational domain is no longer fixed by changes in time, which has to be taken into account. In order to achieve higher precision near the wall surface, the use of the mesh morphing method is advantageous for maintaining the boundary surface grid in the grid formation when the wall moves, which is the wing interface as illustrated in Fig. 4-3(a), with the structural defamation [65]. This method named the bi-directional coupling simulation of fluid structure interactions for the flow field around an elastic moving body. It has been used for clarifying the wake structure of the vortices and characteristics of the dynamic thrust of the 2D elastic moving airfoil numerically [66]. And also it has been clarified by experiment [67].

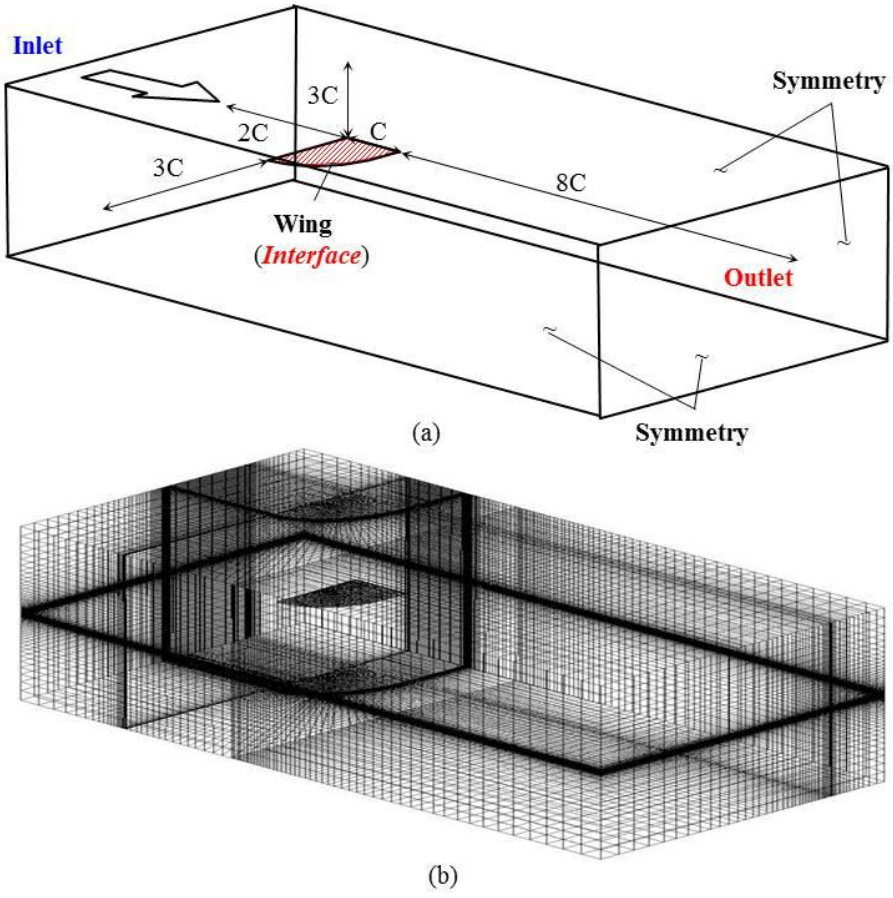

Fig. 4-3 FSI wing models in CFD, (a) fluid domain analysis and boundary conditions, (b) computational grid

4.1.2.2 Boundary conditions for FSI simulation

The boundary conditions in FSI simulation are summarized as shown in Table 7, which are almost same with CFD analysis of the flapping rigid wing model for fluid analysis and FEM modelling for structural analysis. In addition, zero angle of attack (α=0°) is defined, because only the deformation effect to the thrust-production will be considered. The material properties of the wing frame, which are E_c of 533 [GPa], ρ_c of 1600 [kg m^-3], and poison's ration (ν) of 0.3, are defined. For the wing membrane, E_p of 1[GPa], ρ_p of 300 [kg m^-3], poison's ration (ν) of 0.3, and thickness of 70 μm, are adopted, because it is the best FEM model for FSI simulation.

Especially, FSI model has needed to setup very strict conditions. Hence, it has been so difficult to find the appropriate condition for all models. However, meshing, time step and coupling criteria must be specified as appropriate criteria for each wing model. For example, in these models, mesh convergence and time step are *10e-4* and *10e-4* respectively.

Table 7 Conditions in FSI simulation of the flapping elastic wing

Materials (Fluid/Structure)	*Air/ Carbon rod & Paper*	Vel. Inlet	*1.5 [m/s]*
E_C / E_P	*533 / 1 GPa*	Re	*8000*
Node (CSD) / Mesh (CFD)	*8,000 / 1,200,000*	Solution convergence	*10e-4*
Turbulent model	*SST k-w*	Mesh convergence	*5e-6*
Angle of attack, α	*0 °*	Time step, Δt	*0.0005 [s]*
Motion/Cycle	*Flapping/ 6 cycles*	Cal. Time	*5 weeks*

4.1.2.3 Limitation of FEM analysis with the prediction of thrust-productions

Figure 4-4 shows DRR results both FEM and FSI simulation, which can be seen that maximum DRR results from FSI analysis has been larger that FEM results about 55 and 45 percentage of the wing A and D respectively, due to the fluid force effects. In addition, the percentage difference will increase when the wing flexibility increase relatively. Since, it is shown that FSI simulation is better than FEM to predict the realistic deformation characteristics. Thus, the deformation effects to thrust-production from FSI simulation have been close to actual behaviors.

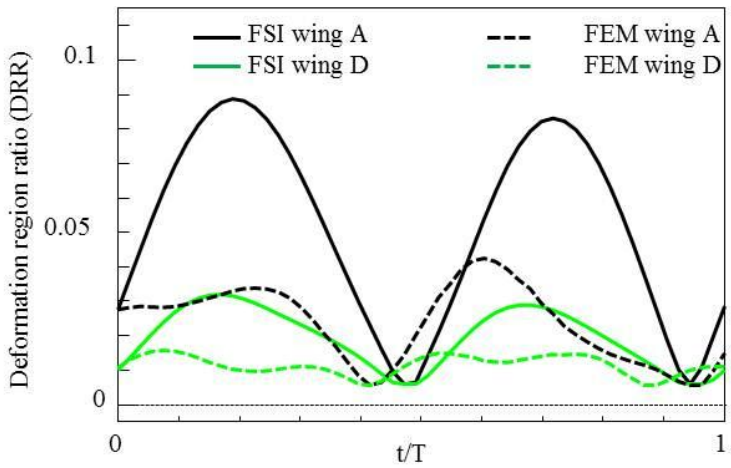

Fig. 4-4 Comparison of DRR results performed by FEM and FSI simulation

4.2 Modification of DRR's principle

4.2.1 Application of DRR's principle for predicting thrust force

Recently, it has not had a good way for predicting the thrust generated by an elastic deformation. To be useful for fluid engineering, the new way of these prediction has been proposed, which I named the principle of the deformation region ratio (DRR). In physical meaning, the order magnitude of the wing's deformation effects to increasing dynamic thrust, which is compared with flapping rigid wings and original wing shape, has been studied. Because of the shape of flapping elastic wing can be changed by flexibility and flapping motion, hence it causes to the thrust produce of the wings either. Most of the designing the wings have not been considered that the elastic deformation effects can improve the wing efficiency by itself deformation. Besides, it has been difficult for predict the elastic deformation effect by considering vortex structure, and also its relationships have been indirect involving. On the other hand, the deformation has directly affected to the thrust-producing as shown in Fig. 4-5.

However, it has been found previously that C_T and *DRR* have been similar tendency qualitatively, but different in their amplitude and phase as illustrated in Fig. 4-6. Hence, the reasons of why they have been different have to be explained clearly to support the hypothesis.

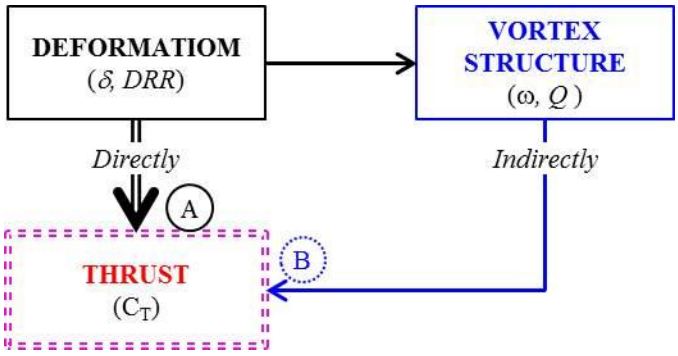

Fig. 4-5 Relationship of producing thrust force based on the deformation effects

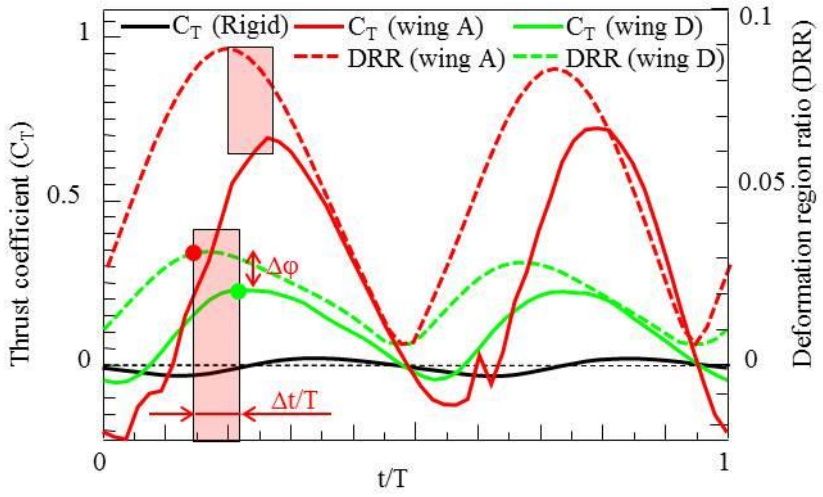

Fig. 4-6 Different amplitude and phase between dynamic thrust and DRR variable

4.2.2 The relationships between DRR and dynamic thrust

In order to find the reasons why the phase and amplitude of DRR variable are different from thrust coefficient, the expression of the thrust force, which depends on DRR, has to be defined.

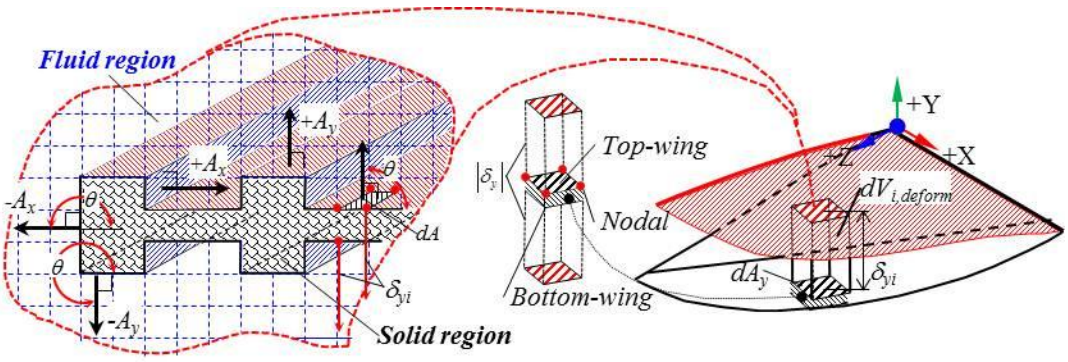

Fig. 4-7 Wing's volumetric deformation related with deformational displacement

Let's $Vol_{y,deform}$ is the volumetric deformation as shown in Fig. 4-7(right). In general, for a flat, plane and curve area, the volumetric deformation equation is a surface integral of the deformational displacement (δ_y) around the wing surface can be expressed as:

$$\left|Vol_{deform}\right| = \oint_A \left|\vec{\delta}_y\right| d\vec{A} \tag{4-1}$$

where *A* is the wing's surface. Due to the deformational displacement is vector value, so absolute deformation is only the positive value. The area required to calculate the volumetric deformation. For fluid passing through a wing, the volumetric deformation changing is equal to volumetric flow rate. It may be useful for considering force acting on the moving body by momentum analysis. Actually, the vector area is a combination of the magnitude of the area through which the pressure acts on it and a unit vector to the area, ***n***. The relation is ***A*** = *A****n***.

Since, the reason for the dot product is as follows:

$$V_{deform} = \delta_y A \cos\theta \tag{4-2}$$

where θ is the angle between the unit normal ***n*** (***A***=*A****n***) and the deformational displacement of the deformational volume element as can be seen in Fig. 4-7(left). All volumetric deformation which is in tangential direction to the area, that is perpendicular to the unit normal of area, so the volumetric deformation is zero. This occurs when $\theta = \pi/2$ and $3\pi/2$.

Since, the wing's surface has both top- and bottom-surface, thus a half volumetric deformation is equal to the volumetric deformation of DRR variable, which had been defined in Eq. 3-16 (see in section 2.3.1).

Now, newly DRR's expression can be written by:

$$DRR = \frac{\left|V_{deform}\right|}{2A_{y0}^{1.5}} = \frac{\left|V_{deform}\right|}{2A_{wing}^{1.5}} \tag{4-3}$$

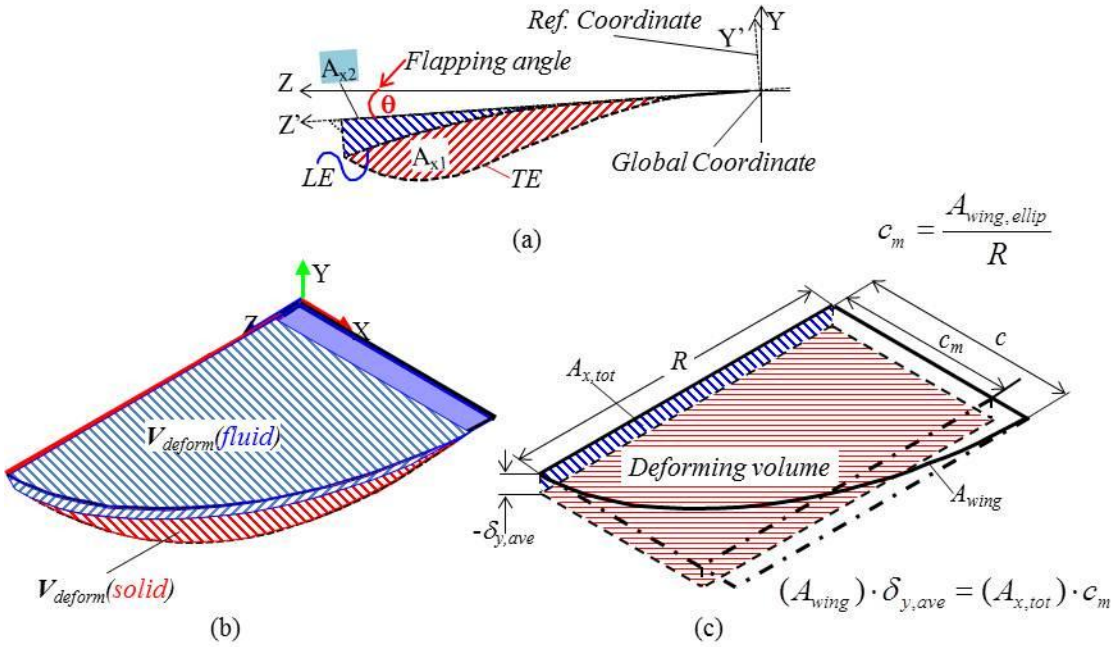

Fig. 4-8 Imaginary of volumetric deformation due to flapping motion of elastic wing, (a) The projection area on the wing surface, (b) Deformational area projected on fluid and wing surface, (c) Average volumetric deformation calculated by average deformation

4.2.3 Leading- and Trailing-edge deformation and the deformational projection area

Let's total volumetric deformation consists two volume, which are occurred by the leading-edge deformation area (blue area) and trailing-edge deformation area (red area) as shown in Fig. 4-8(a). Thus, the volumetric deformation is separated into two volumes, which it is computed by mean chord multiply with the deformational area projected on fluid and wing surface as shown in Fig. 4-8(b). So, the volumetric deformation can also be calculated by:

$$V_{deform} = A_{x,tot} \cdot c_m \tag{4-4}$$

where $A_{x,tot}$ is the total projection area, which Y-deformation (δ_y) required to calculate it, c_m is the mean chord length as shown in Fig. 4-8(c). Note that the total projection areas, which belong in flight direction, occur from the wing's deformation, thus the leading-edge deformation area is only projected on the fluid domain. On the other hand, the trailing-edge deformation is only projected on the wing's surface. If the total projection area can be calculated by an average deformation ($\delta_{y,ave}$) and wingspan (R), thus the volumetric deformation can also expressed by:

$$V_{deform} = \left(R \cdot \delta_{y,ave}\right) \cdot c_m \tag{4-5}$$

where $\delta_{y,ave}$ is the average deformation in Y-axis. By Eq. 4-3 and 4-5, so we get following expression as:

$$2DRR \cdot A_{wing}^{1.5} = A_{x,tot} \cdot c_m \tag{4-6}$$

Since, the projection area can be given by:

$$A_{x,tot} = A_{xTE,deform} + A_{xLE,deform} \tag{4-7}$$

where $A_{xTE,deform}$ is the trailing edge deformation area, and $A_{xLE,deform}$ is the leading edge deformation area.

Thus, we will have:

$$(A_{xTE,deform} + A_{xLE,deform})c_m = 2DRR(A_{wing}^{1.5}) \tag{4-8}$$

Now, the trailing-edge projection area can be found as:

$$A_{xTE,deform} = \frac{2DRR(A_{wing}^{1.5})}{c_m} - A_{xLE,deform} \tag{4-9}$$

The trailing edge projection area ($A_{xTE,deform}$) required to calculate the thrust force generated by the elastic deformation. Moreover, the pressure difference between top- and bottom-wing surfaces is used for calculating the resultant force acting on the wing together.

4.2.4 Physical meaning of the deformational projection area

The quantity of the trailing-edge projection area is proportional to the volumetric wing's deformation and the leading-edge deformation. In particular, the positive leading-edge deformation means that, the deformational velocity is same direction with the flapping velocity. Hence, it will increase the lift force, on the other hand, in the opposite direction, will decrease the lift force. Moreover, their same velocity direction will increase the pressure difference between the top- and bottom-surface of the wings.

Another important aspect of the trailing-edge projection area is that the thrust force experienced by the wing's deformation is proportional to both DRR and the leading-edge projection area. Fig. 4-9 illustrates the different wing's deformation volume but similar projection area. These two cases is similarly deformational velocity at the leading-edge. However, they have produced the different thrust force. Thus, the projection area is just one parameter dominated the thrust-producing on the wing's deformations.

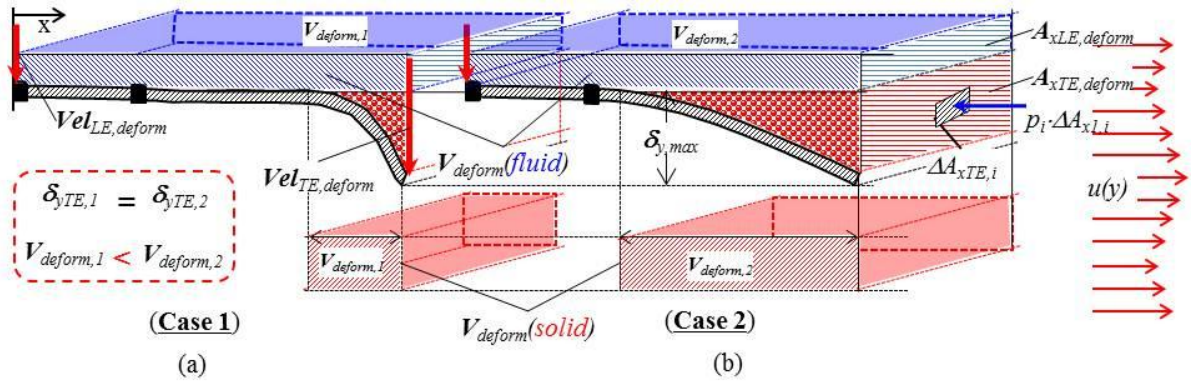

Fig. 4-9 Deformational projection areas, (a) case of small DRR, (b) case of large DRR

4.2.5 Pressure difference on flapping elastic wing

By considering the pressure distribution on the wing surface, average pressure is one variable which can be used for finding the pressure force as shown in Fig. 4-10(a). From the results of pressure distribution, you can compute the average pressure to be using in calculation of the total thrust force, because the local thrust for cannot evaluate the thrust coefficient of the wing. Due to pressure is the scalar quantity, thus the different pressure between top- and bottom-surface wing becomes small actual value occurring like Fig. 4-10(a) shows. In fact, this pressure difference has occurred larger than average it form local pressure, because only compressive pressure is positive value. Hence, the absolute local pressure will be used for calculating the average pressure as Fig. 4-10(b) shows.

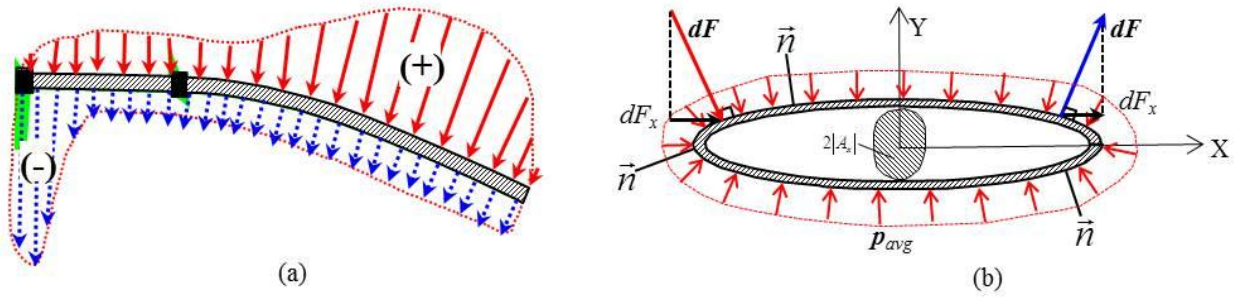

Fig. 4-10 Pressure distribution on wing surface, x/R=0.75, (a) Pressure profile, (b) Average pressure

So, the average pressure can be calculated as:

$$p_{ave} = \frac{1}{A}\int_A |p| dA \tag{4-10}$$

Let's thrust force estimate with average pressure and the projection area on the wing surface. Due to average pressure is integrated from absolute pressure over close surface, thus pressure difference (Δp) equals to two times of the average pressure ($2p_{ave}$). Also, you can see twice projection area for the close surface in Fig. 4-10(b). Thus, an absolute thrust force can be defined by:

$$T = 2p_{ave} \cdot A_{x1} \tag{4-11}$$

Since, $2p_{ave}=\Delta p$. So,

$$|T| = \Delta p \cdot A_{x1} \tag{4-12}$$

Now, the absolute thrust coefficient can be calculated as:

$$|C_T| = \frac{|T|}{0.5\rho_f A_{wing} U_{ref}^2} \tag{4-13}$$

So, we got that

$$|C_T| = \frac{\Delta p \cdot A_{x1}}{0.5\rho_f A_{wing} U_{ref}^2} \tag{4-14}$$

Using the projection area and DRR variable, thus the thrust coefficient can be expressed by:

$$C_{T,DRR} = \left(\frac{\Delta p}{0.5\rho_f A_{wing} U_{ref}^2} \right) \cdot \left(\frac{2DRR \cdot A_{wing}^{1.5}}{c_m} - A_{LE,deform} \right) \tag{4-15}$$

Also, new equation of calculation the thrust coefficient is given by:

$$C_{T,DRR} = \left[\frac{2\Delta p \cdot A_{wing}^{1.5}}{0.5\rho_f c_m A_{wing} U_{ref}^2} \right] DRR + \left[\frac{-\Delta p A_{LE,deform}}{0.5\rho_f A_{wing} U_{ref}^2} \right] \tag{4-16}$$

Let's K_{DRR} and C_{DRR} is the factors for calculating the thrust coefficient using the DRR production. So, it can be reduced as:

$$C_{T,DRR} = K_{DRR} \cdot DRR + C_{DRR} \tag{4-17}$$

where, K_{DRR} is the DRR's factor based on the characteristics of the wing, and C_{DRR} is the DRR constant based on the leading deformation, which it will be equal to zero when no deformation at the leading-edge. Both K_{DRR} and C_{DRR} depend on the wing's surface pressure, which is dominated by the flight speed, flapping velocity, deforming velocity. Thus, they can be expressed as:

$$K_{DRR} = \frac{2\Delta p \cdot \sqrt{A_{wing}}}{0.5\rho_f c_m U_{ref}^2} \tag{4-18}$$

$$C_{DRR} = \frac{\Delta p \cdot A_{LE,deform}}{0.5\rho_f A_{wing} U_{ref}^2} \tag{4-19}$$

Note that the dynamic pressure difference and trailing projection area are like as the wave form function. In general form, they can be defined these following are:

$$\Delta p = A\sin(2\pi ft + \varphi) + \phi \tag{4-20}$$

$$A_{TE,deform} = A\sin(2\pi ft + \varphi) + \phi \tag{4-21}$$

Hence, the C_T amplitude depends on the amplitude both pressure difference and trailing edge projection area. On the other hand, *DRR* amplitude has only depended on the amplitude of trailing edge projection area.

4.2.6 Physical meaning of K_{DRR} and C_{DRR}

From Eq. 4-15, K_{DRR} is related to the potential energy which exists when a force acts on the wing's surface. According to the law of conservation of energy, energy cannot be created or destroyed, hence this energy cannot disappear. Instead, it is stored as potential energy. When the wing is deformed, this stored energy will be converted into kinetic energy by the restoring force, which is wing's elasticity. At maximum deformational velocity is its maximum potential energy (dynamic pressure). When the wing speed is down, the potential energy turns into kinetic energy. C_{DRR} indicates the potential energy due to the elasticity at the leading edge.

4.3 Results and Discussions

4.3.1 Dynamic lift and thrust based on the elastic deformation effects

To clarify the elastic deformation effects, the unsteady dynamic forces should be considered. As mentioned before, the flapping motion also affects to generating dynamic forces, hence the results based on the elastic deformation effects should be compared with the flapping rigid wing. Also, main purpose is to consider only the elastic deformation effects to obtaining aerodynamic forces.

4.3.1.1 Dynamic lift

Firstly, dynamic lift versus the flapping motion will be considered as shown in Fig. 4-11. It can be seen that increasing lift is caused by vertical velocity which consists between angular and deformational velocity. In particular, small effect has been at the angular velocity closed to zero as zone A and B in Fig. 4-11. Moreover, these zones correspond with the maximum deformation at point (A) and (B) in Fig. 4-12. On the other hand, other region has dominated the increasing lift force.

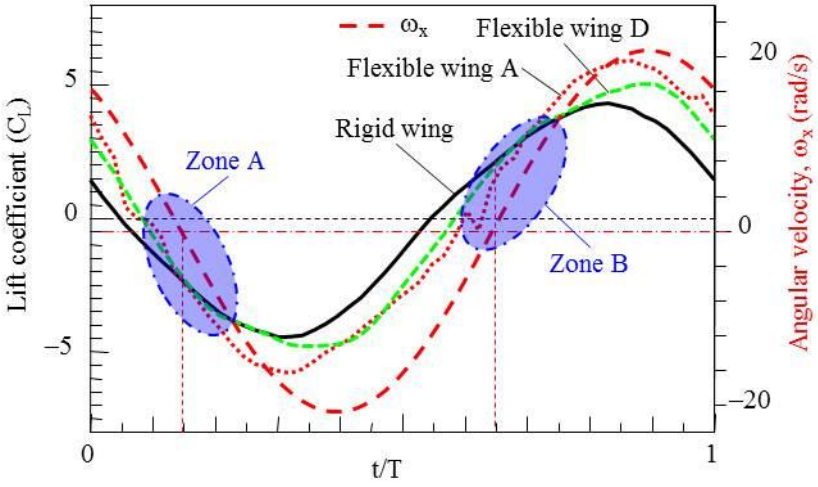

Fig. 4-11 Dynamic lift versus non-dimensionless period time, α = 0. [deg]

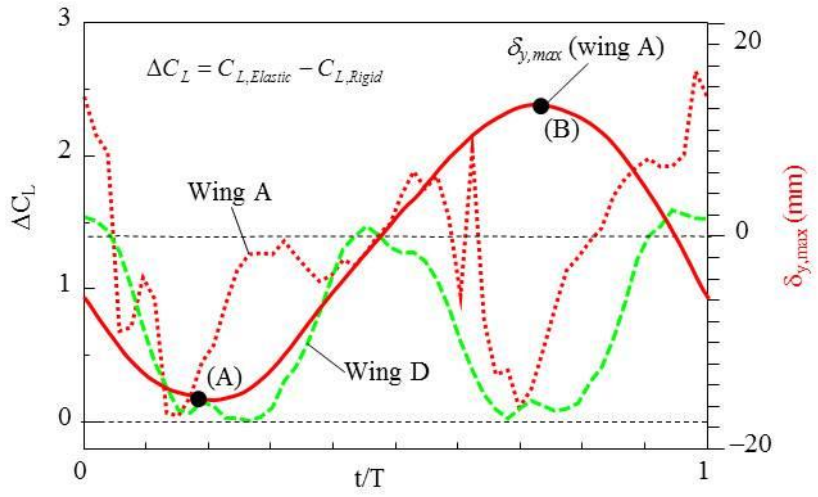

Fig. 4-12 Increasing dynamic lift based on elastic deformation versus non-dimensionless period time

4.3.1.2 Dynamic thrust

In chapter 3, dynamic drag force had discussed, otherwise it invers of the thrust force. Thrust is the structural force exerted on the fluid (which is opposite direction with the direction of body motion). For the other way of generating driving force, C_D must be decreased. However, for flapping flight, C_T should be increased, which caused by flapping motion and elastic deformation motion. Increasing thrust caused by elastic deformation is also demonstrated as shown in Fig. 4-13. It is found that high thrust has occurred, which it delays from the maximum deformation. It seems to be phase shift between the maximum deformation and thrust difference (ΔC_T) as shown in Fig. 4-14.

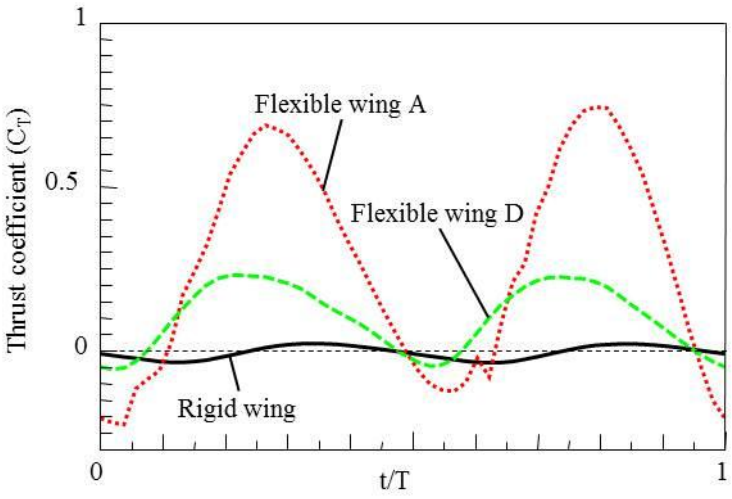

Fig. 4-13 Dynamic thrust versus non-dimensionless period time

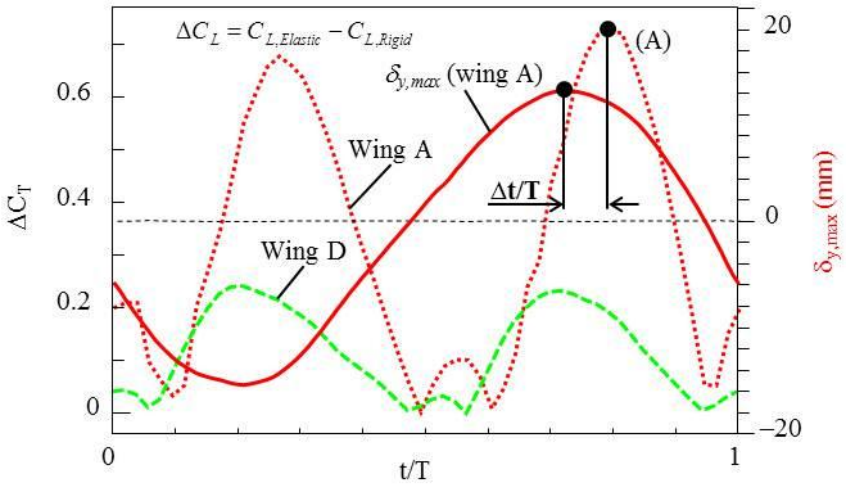

Fig. 4-14 Increasing dynamic thrust based on elastic deformation versus non-dimensionless period time

4.3.2 Vortex structure around elastic wings

Recently, the wake patterns, thrust force coefficient, and propulsive efficiency have been observed [12, 56, and 68]. To establish a relationship between the flow structures and force-production, the instantaneous vorticity and deformation distribution are further plotted on the bottom- and top-wing surface at the point (A) in Fig. 4-13 as shown in Fig.4-15, correspondingly. Iso-surface voticity of 160 [s^-1] has been plotted, which it seems that wing's deformation has slightly affected the vortex structure around the wing. Since, the leading edge vortex is strongly affected by the flapping motion, which mainly affects the force-production rather than thrust-production on deformation effects (see illustration in Appendix C.3). Hence, it has difficultly distinguished the deformation effects to the vortex structures and thrust-productions. Especially, this way has worked rather with smooth shape circulation as shown in Fig. 4-16 [68]. Additionally, the deformational velocity has rather been smaller than the angular velocity (see section 4.4.6 deformational velocity).

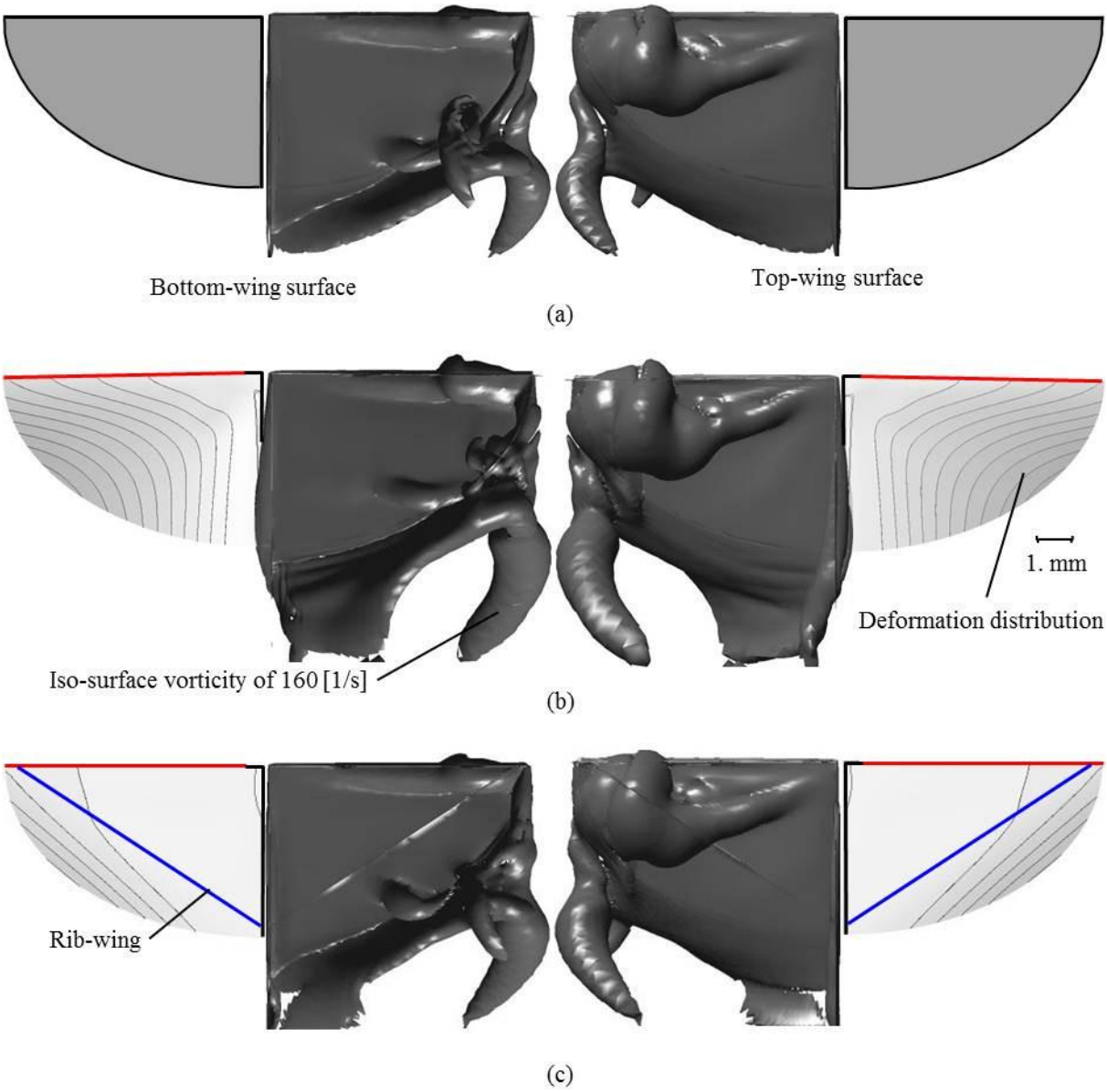

Fig. 4-15 Iso-surface vorticity based on elastic deformation effects, t/T = 0.21, (a) Inflexible wing A, (b) Flexible wing A, (c) Flexible wing D

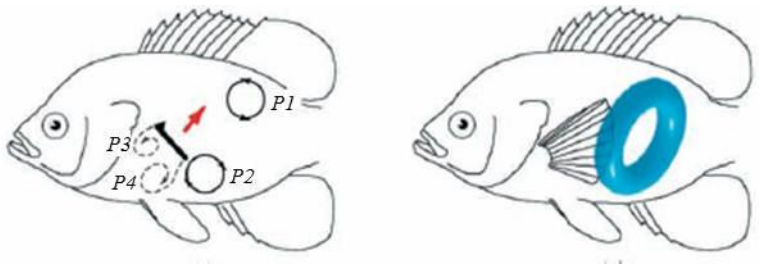

Fig. 4-16 3D vortex wake dynamic on a swimming fish to be used for measurement the dynamic forces

4.3.3 Momentum transferred by deformation

Based on fluid dynamic view point, as well known, total force acting on the control surface (wing surface) of fluid domain equals to momentum changes across that control surface. The momentum in flow direction (X-axis) is considered for finding the thrust force obtained by elastic defamation effects. In case of flapping rigid wing and assumption of very small shear force (see Fig. 4-17(a)), it has no horizontal force by deformation effect because of that is zero projection area.

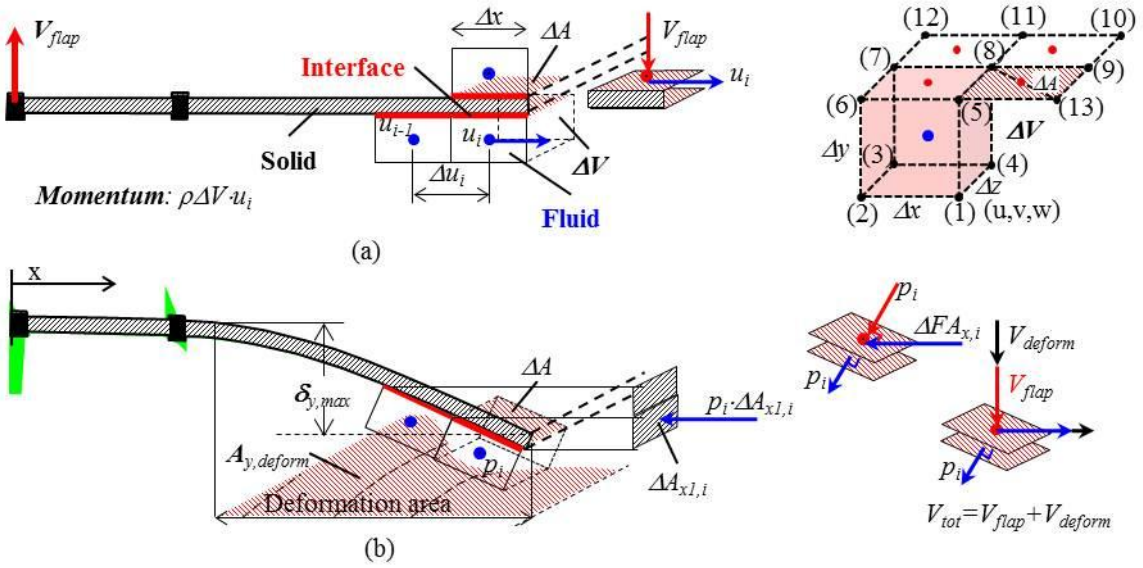

Fig. 4-17 Momentum transferred at the interface surface, (a) Flapping rigid wing, (b) Flapping elastic wing

For elastic wing, trailing edge deformation causes to make the projection area as shown in Fig. 4-17(b), thus x-momentum per unit volume can be defined as:

$$P_{x,i} = \rho \frac{\Delta u}{\Delta t} \Delta V = \frac{\Delta p}{\Delta x} \Delta V = \Delta p \Delta y \Delta z \tag{4-22}$$

So, the momentum transferred by wing's deformation can be written as:

$$P_x = u \cdot \delta_{y,\max} \cdot \left(\frac{x}{c_m}\right) \cdot \left(\frac{\rho_f R}{A_{wing}}\right) \left[\frac{N \cdot s}{m^3}\right] \tag{4-23}$$

Thus, general equation in X-axis for each one fluid finite volume can be found as:

$$P_{x,i} = (\rho_f u_i) \cdot \left(\frac{\delta_{y,i}}{\sqrt{A_{wing}}}\right) \cdot \left(x_i R^{0.5} c_m^{-1.5}\right) \tag{4-24}$$

Now, max-momentum at max-deformation can be computed by:

$$P_{x,\max} = (\rho_f \cdot u) \cdot \left(\frac{\delta_{y,\max}}{\sqrt{A_{wing}}}\right) \cdot \left(c_{ref} R^{0.5} c_m^{-1.5}\right) \tag{4-25}$$

4.3.3.1 Horizontal velocity nearest the wing surface

The max-deformation has occurred at the plane of x/R of 0.75 (wing D). So, the velocity profile on these planes is shown in Fig. 4-18. It can be seen that the horizontal velocity produced on the wing gives rise to vertical deformation.

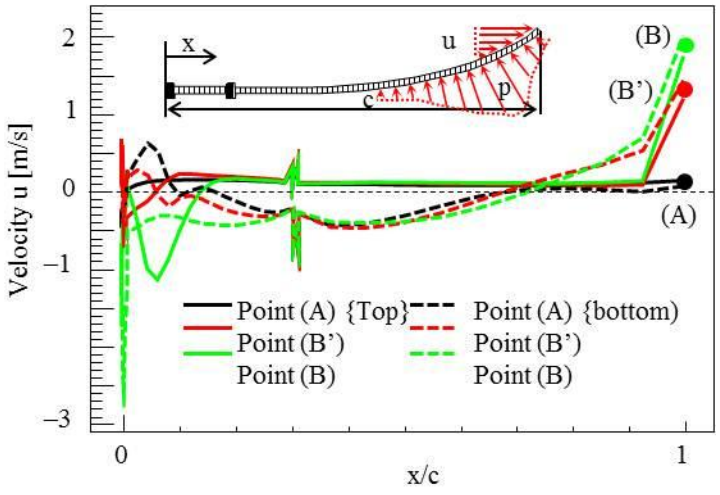

Fig. 4-18 Velocity distributions versus the non-dimensional chord length, Wing D

4.3.3.2 Momentum based on DRR variable and Thrust

A flapping elastic wing of the flying robot generates forward thrust when air is pushed in the direction opposite to flight, which the flapping robot normally achieve thrust during flight by flapping their wings. The forward thrust is proportional to the mass of the airstream multiplied by the change in velocity of the airstream. Thus, the velocity distribution on the wing has dominated the thrust as the results shown in Fig. 4-19(a), which the thrust force on the point B is higher that point B' because of the velocity. Although, high velocity which relates to dynamic pressure has occurred at both leading- and trailing-edge position, but the dynamic pressure at trailing-edge is strongly affected to thrust because of it has high projection area either. Also, the max-momentum given by Eq. 4-25 and thrust coefficient are plotted as shown in Fig. 4-19(b). It is demonstrated that thrust coefficient tends to be similar with momentum. In particular, maximum thrust force has occurred when momentum is maximum value as point (B) and (D) in Fig. 4-19(b).

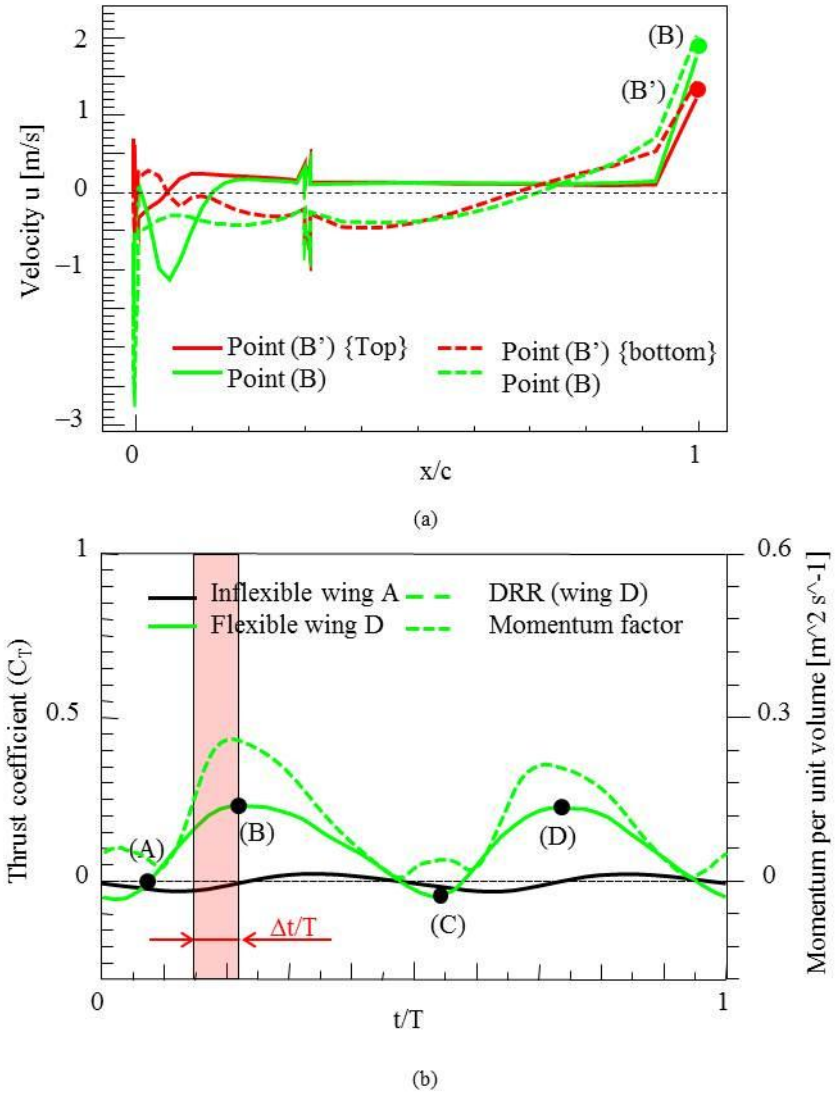

Fig. 4-19 Dynamic thrust based on flow momentum, (a) Velocity profiles on the wing's surface, (b) Contribution to dynamic thrust by exit momentum

4.3.4 Relationships between DRR variable and dynamic thrust

Based on the hypothesis whether DRR can predict the thrust coefficient, all the FSI simulation results presented in the subsequent sections are for the flapping elastic wing during the 6th cycle of flapping. The relation between thrust coefficient (C_T) and wing's deformation which is based on the variable of deformation region ratio (DRR) is demonstrated as shown in Fig. 4-20. It can be seen that thrust force produced on the wing gives rise to DRR according to the stroke flapping cycle, which it has occurred two times in one loop of flapping motion. Thrust force makes the negative horizontal force. Also, it shows that high structural velocity region has mainly affect to lift force, and the zero phase difference between rigid and elastic wing has occurred. When the wing moves in upstroke and downstroke give rise to negative and positive horizontal force. Actually, the flying robots employ asymmetric wing motion during downstroke and upstroke [53]. However, it has only been small different in resultant force acting on the wing surface, but rather different in flow structure around the wings. Due to the thrust force related directly with the wing's deformation, hence one side of the flexible wing was modelled by two-way coupling of fluid-structure interaction (FSI) simulation.

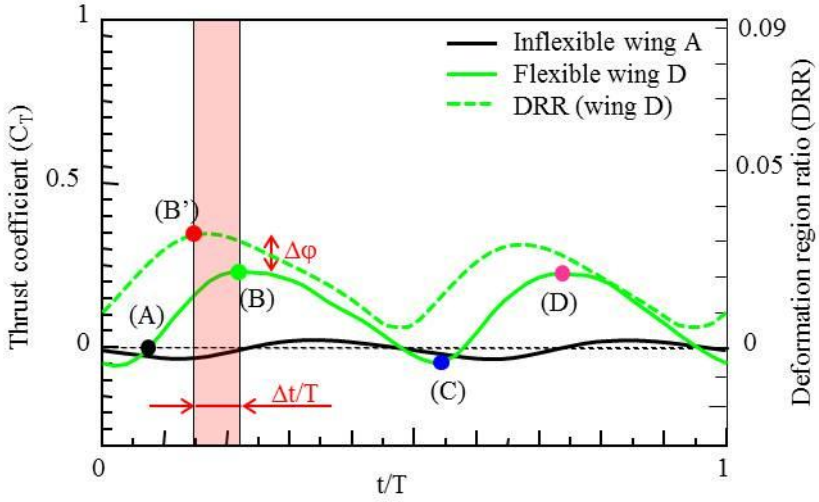

Fig. 4-20 Critical thrust coefficient and DRR versus the non-dimensional period time, Wing D

By FSI simulation, the both dynamic deformation and forces can be obtained. Herein, the realistic deformations can be performed, because both inertial and fluid force effects are considered in this model too. It is shown that the fluid force effect has increased the max-deformation of about 1.25 (no rib) and 1.18 (within rib, wing D) times of the inertial force effect, which is compared with FEM results (see Appendix B.3). However, this effects based on the wing's flexibility, thus when wing's flexibility was changed, the fluid force effect would change either. However, FIS simulation is better than only FEM simulation, because it has been able considering the deformation effects to generating dynamic forces. Due to DRR variable can evaluate the order magnitude of deformation, hence it is plotted with thrust coefficient as shown in Fig. 4-20. Now, the five critical points was focused as (A), (B'), (B), (C) and (D), which (A) is the zero thrust force, (B') is the max-deformation, (B) is the max-thrust force (up-stroke), (C) is no thrust force, but drag force generated by main flow, and (D) is the max-thrust force (down stroke). In addition, those five points (A, B', B, C, and D), are occurring at the non-dimensional period time of 0.075, 0.15, 0.2, 0.55 and 0.74 respectively. DRR and thrust coefficient has phase difference ($\Delta t/T$) of 0.05.

4.3.5 Surface pressure

Actually, total thrust force is calculated by integrating both the surface pressure and viscous traction in the flow direction over the wing surface area. To approximate the surface pressure effect based on the local surface pressure, the pressure difference on wing sections based on wingspan and chord direction is shown in Fig. 4-21. This figure is plotted as pressure difference (Δp), which referred from Eq. 4-10 as shown in Fig. 4-22(a) and 4-23(a).

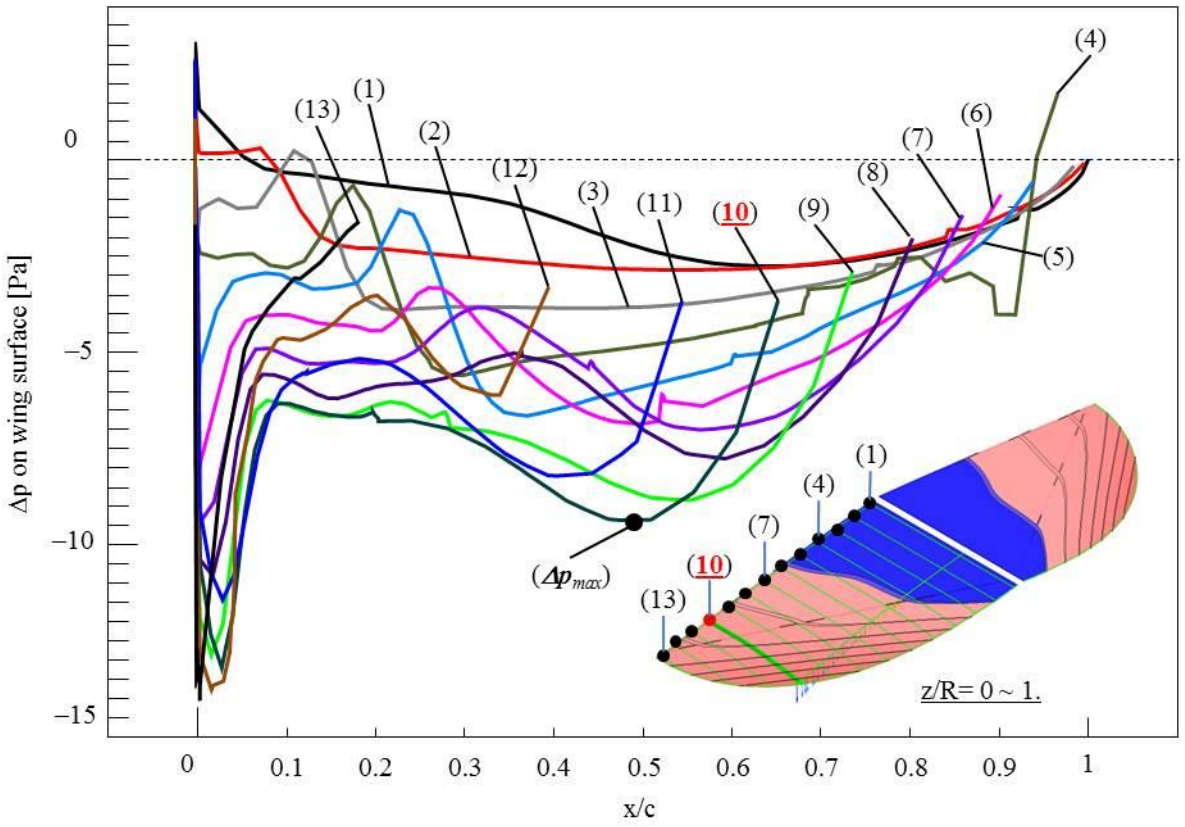

Fig. 4-21 Pressure difference between the Top- and Bottom-wing surfaces versus the wing span and chord length, Wing D, t/T=0.2 , Point (B)

Thirteen section planes of cross-section are focused in wingspan direction, which are *z/R* step increments of 0.083 (10 mm/*R*). It can be seen that the maximum pressure difference has occurred at the cross-section of the maximum deformation as the line (10) in Fig. 4-21. However, the maximum pressure difference has not occurred at the trailing edge, but it is at the leading edge. This maximum pressure is dominated by the leading edge vortex (LEV) [53]. It is described in chapter 3. If the deformation effect to producing of the thrust force has been considering, then the maximum pressure at the leading can be neglected, because it has been no projection area in thrust direction at the leading edge. It can be seen in Fig. 4-24(b), which all the lines is no deformation gradient a long chord direction. Although, the surface pressure depends on the deformational, angular velocity (flapping motion) and flight speed as the imaginary shown in Fig. 4-22. But, thrust force is created when the wing pushing on the air by flapping and deformation mainly. Thus, flight speed is the producing of net thrust force.

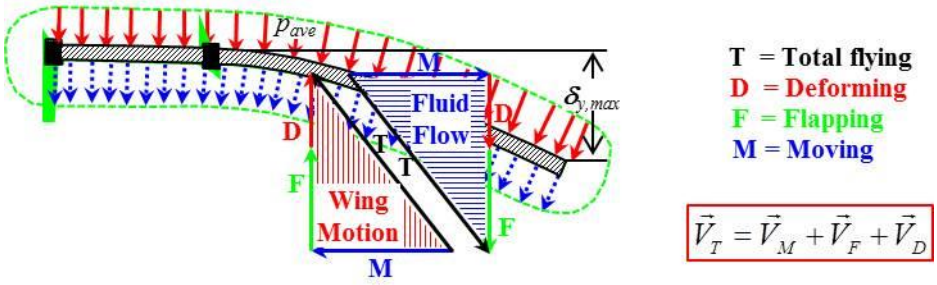

Fig. 4-22 Imaginary of surface pressure related with solid motion

The cross-section at z/R of 0.75 and the point (B) corresponding with Fig. 3-18, is adopted to illustrate the local pressure effect to the average pressure on the wing surface, because it is highest pressure difference and dynamic thrust as shown in Fig. 4-23. At this point, the wing is moving up, which means upward flapping velocity (see in Fig. 4-23(a)). Since, it occur the positive pressure on the top-wing surface and negative pressure (vacuum pressure) below the bottom-wing surface. Thus thrust force should be calculated from minus pressure difference (-Δp). Although, they are opposite pressure value of the point (B) and (D), but both of them still give the positive thrust force due to the direction of trailing edge deformation. This can be seen by comparing the results in Fig. 4-24(a) and 4-24(b). Moreover, the maximum pressure difference is found at the x/c of 0.5.

Basically, Δp can be used for estimating aerodynamic forces directly, but the centre pressure difference must be determined either. Experimentally, it has been difficult to measure it for a small structure.

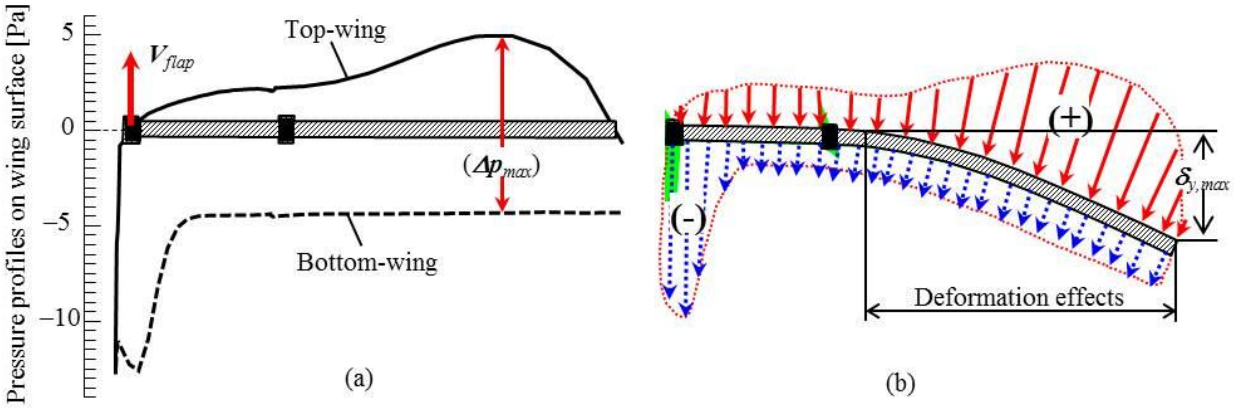

Fig. 4-23 Pressure profile at the max-deformation, z/R = 0.75 (Line ***(10)***), Wing D

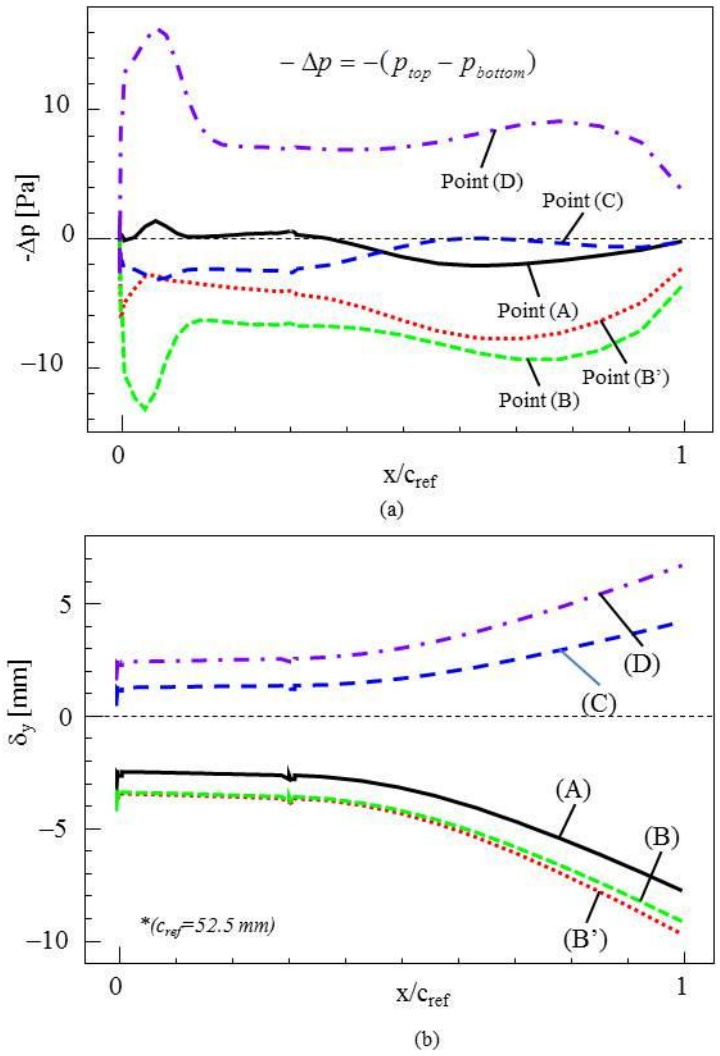

Fig. 4-24 Pressure difference on the wing surface and wing's deformation versus the chord length, z/R=0.75, Wing D, (a) Pressure difference, (b) Vertical deformation component

4.3.6 Deformational velocity and dynamic thrust

Herein, the wing's flexibility is main parameter to the thrust force affected by deformation. The principal wing velocity is dominated by the deformation amount, which can be evaluated as DRR variable. Hence, a changing of deformation has been similar to the variation of the wing's motion. Figure 4-25 shows the velocity components at the max-deformation point related with DRR value and dynamic thrust. It is found that max-DRR has occurred when the zero deforming velocity, at point (A), because net pressure force and structural elasticity force is in equilibrium ($V_{deform}=0.0$). On the other hand, the thrust force is still increasing to maximum point lately, because the effects of the deformational velocity (back colour of solid line) and DRR (red colour of dot line). Although, the maximum deformation ($\delta_{y,max}$) has been nearly same value, but they are different in thrust force as well as shown in Fig. 4-26. It causes of DRR characteristics of each wing.

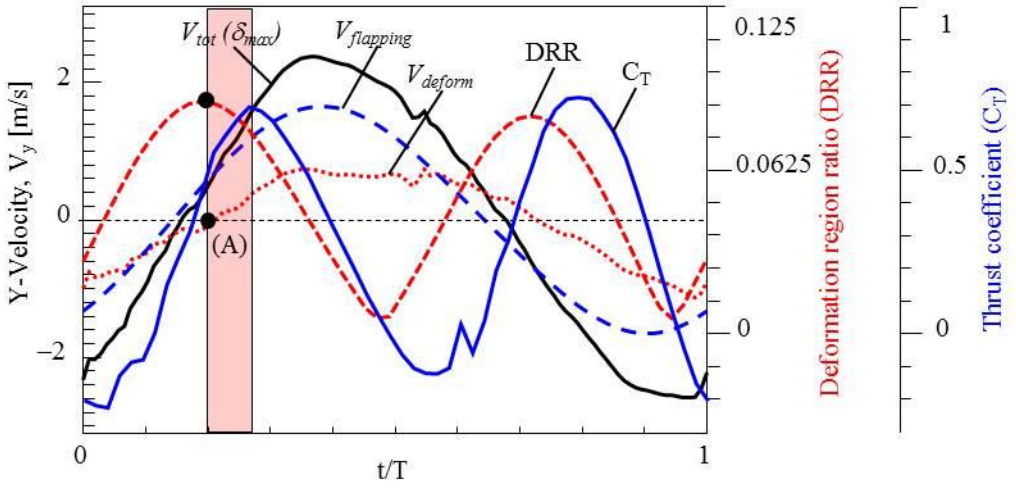

Fig. 4-25 Deforming velocity at the maximum deformation point ($\delta_{TE,max}$), Wing A

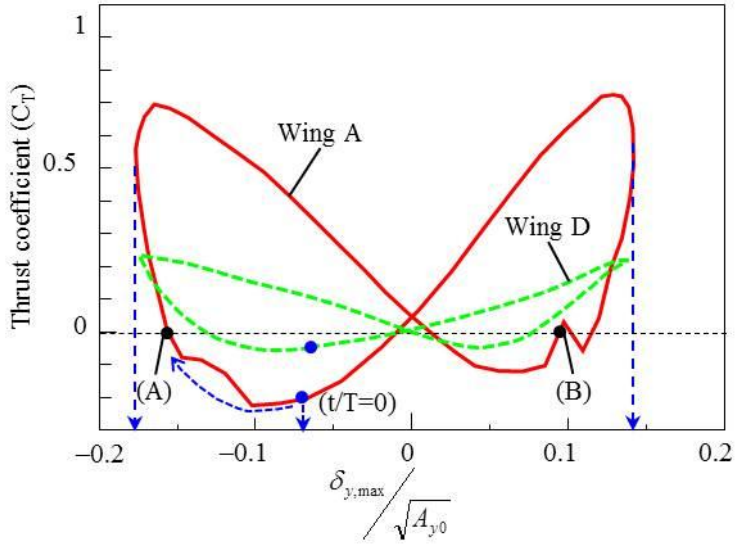

Fig. 4-26 Dynamic thrust versus the max-deformation, Wing A and D, $\delta_{TE,max}$

4.3.7 Projection area related with the elastic deformation

As mentioned in subsection of the surface pressure, thrust force does not only depend on the pressure difference but also the amount of the trailing edge projection area. Figure 4-27 shows the leading- and trailing-edge deformation versus the position along wingspan direction. Five critical points are illustrated to compare the variations of deformation, corresponding with Fig. 4-20. The leading- and trailing-edge deformation difference ($\Delta\delta_{TE-LE}$) causes to occur the deformational angle of attack (α_{deform}), which can be expressed as:

$$\alpha_{deform} = \tan^{-1}\left(\frac{\Delta\delta_{TE-LE}}{c_{ref}}\right) \tag{4-26}$$

The maximum α_{deform} of 4.4, 6.6, 6.5, 3.3 and 4.4 [deg] are found for the points (A), (B'), (B), (C), and (D) respectively. Note that c_{ref} of about 52 mm is used to calculate α_{deform}. Also, dynamic projection area versus the non-dimensional period time is shown in Fig. 4-28.

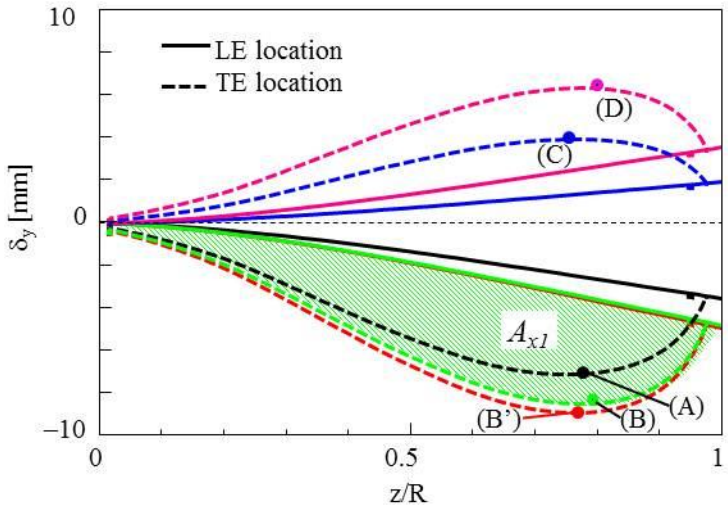

Fig. 4-27 LE and TE detonation in Y-axis versus the non-dimensional span, Wing D

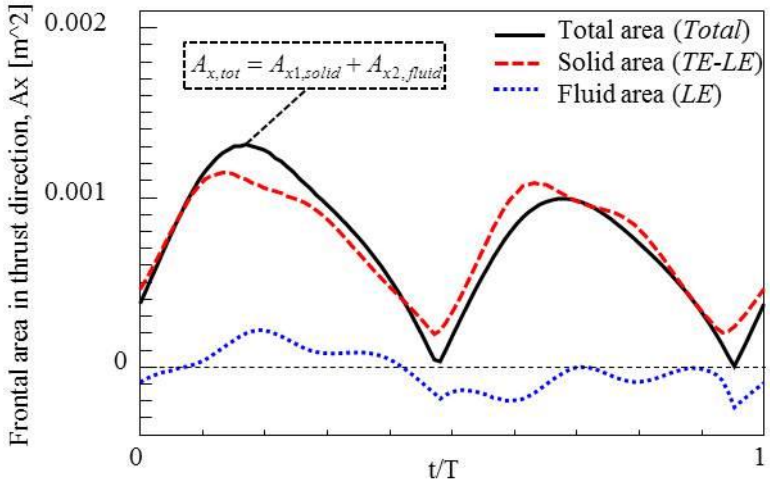

Fig. 4-28 Projection areas versus the non-dimensional period time, Wing D

The projection area on the wing surface ($A_{x1,solid}$) is calculated for the case of no viscosity effect, thus it is not zero when the total projection area becomes zero as well. However, it may be possible to be used for estimating the thrust force based on DRR variable. Also, you can see more results of the deformational angle of attack effects as reported in Appendix E.

Now, we have both pressure difference and projection area based on DRR variable, which they are like wave form function as Eq. 4-20 and 4-21. Therefore, the dynamic thrust force has occurred from that two waves are in phase. Next, the constructive interference behaviour between the pressure difference and projection area will be described in next subsection.

4.3.8 Constructive interference

A pair of pressure and area wave has experienced interference when they pass through each other. The individual waves have added together (superposition), thus a new wavefront of thrust force is created as shown in Fig. 4-29. The constructive interference has occurred when the maxima of pressure difference and projection area add together (the two waves are in phase). Hence, the amplitude of the force resulting wave is equal to the sum of the individual amplitudes. The effect of the constructive interference between the pressure and area with the different amplitude, but same frequency is illustrated, which both the projection area and average surface pressure cause to increase dynamic thrust as result as well.

Actually, wave form function of the pressure difference depends on the flapping motion as well. Due to the flapping motion is specified by time-dependent flapping angle $\theta_{flap}(t)$ as periodic motion, hence average pressure is time-dependent variable ($p_{ave}(t)$) either, which it belongs with the flapping velocity as result shown in Fig. 4-30. The absolute average pressure has been similar tendency with the flapping velocity qualitatively.

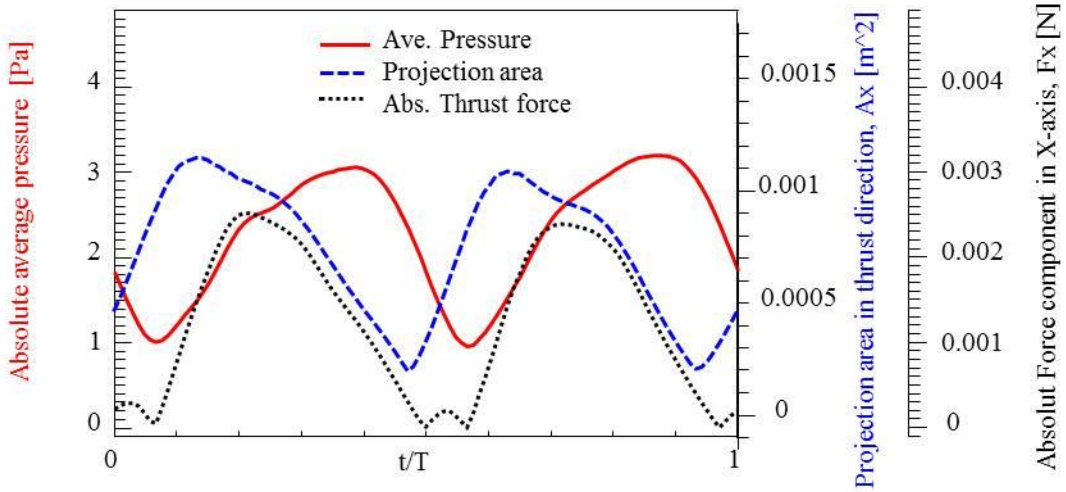

Fig. 4-29 Average pressure, projection area and dynamic thrust force versus the non-dimensional period time, the results of the wing D

Furthermore, the thrust force calculated by DRR variable-based and obtained by simulation are plotted as shown in Fig. 4-31. It can be seen that only high region of thrust force calculated has been closed to the simulation results, but on small thrust force region has been different rather. It might be because of the viscosity effects and the projection area, which was explained previously (the results in Fig. 4-28).

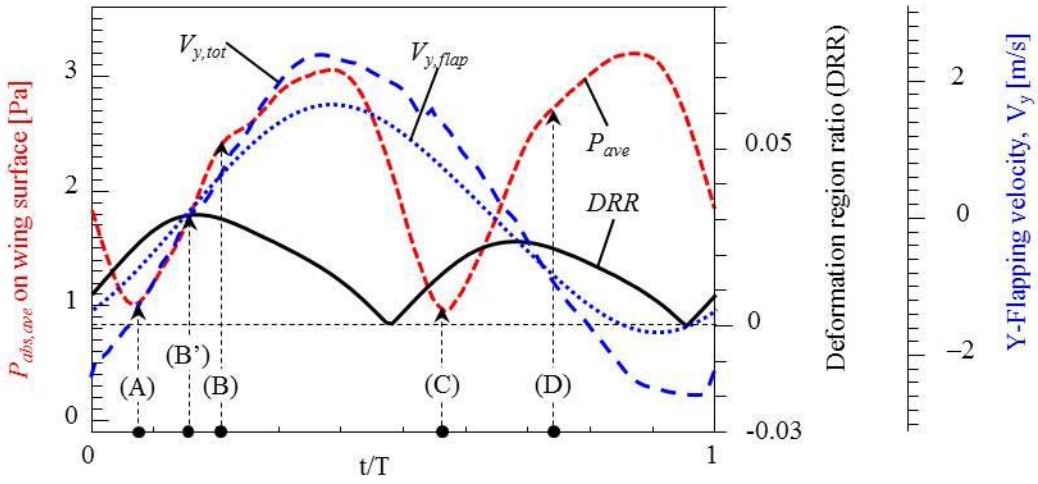

Fig. 4-30 Average surface pressure and DRR tendency versus the non-dimensional period time, Wing D

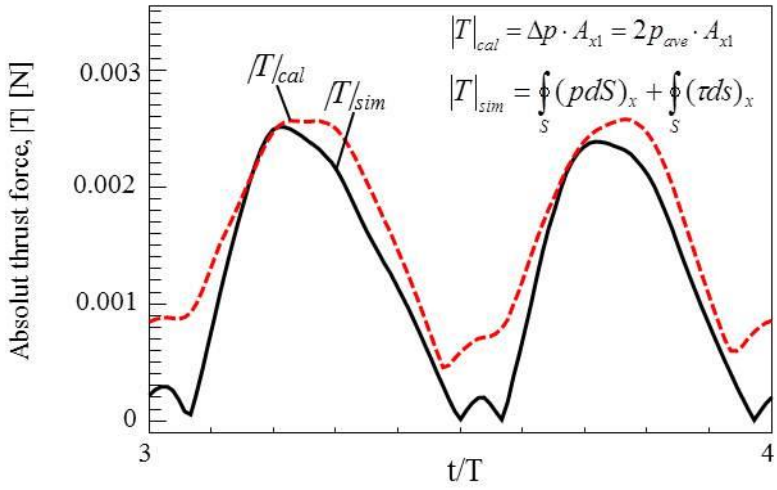

Fig. 4-31 Thrust force calculated by the pressure product and deformational projection area versus the non-dimensional period time, Wing D

Using Eq. 4-16, thrust coefficient is calculated and plotted to compare it with the simulation result as shown in Fig. 4-32. Additionally, it is to verify the development of newly DRR model that predics thrust coefficient. It also shows the relationship between C_T and DRR with DRR's factor and constant should be considered as Eq. 4-20 and 4-21. The calculation results hace been more different with simulation results at the point (A) and (C) than the other points. At both the point (A) and (C), they have lowest the average pressure (see in Fig. 4-30). On the other hand, these points have not occurred lowest DRR. Only one term of right-hand side of Eq. 4-16 is proportional with DRR. But, both terms are protional with the pressure difference. By comparing the order of magnitude between DRR and Δp, it is found that Δp has mainly affected the dynamic thrust.

Since, DRR's principle has been developed to predict the thrust force affected by the elastic deformation for the wings. Results are compared with simulation results for the wing structure without rib-wing and within rib-wing. By comparing, it is found that new thrust coefficient is closed to the simulation results, which an error of 8% and 18 % have occurred for high thrust and small thrust force region, respectively.

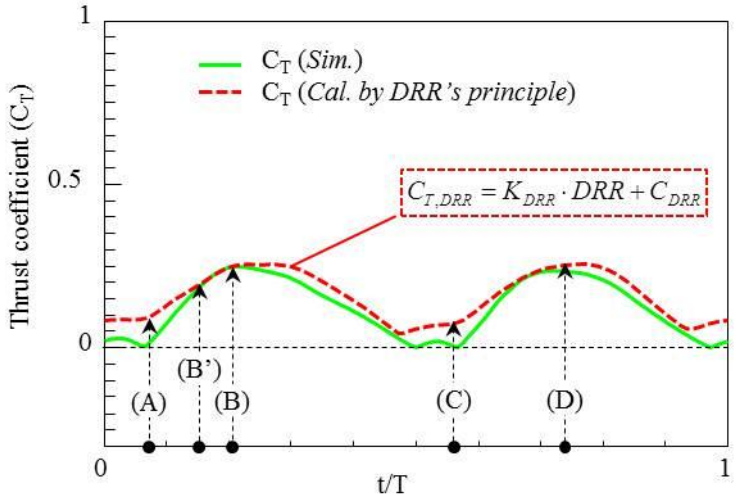

Fig. 4-32 Thrust coefficient calculated by DRR variable versus the non-dimensional period time, Wing D

4.4 Summary

In order to clarify the research hypothesis how DRR can predict the dynamic thrust force on the wings with the elastic deformation effects clearly. FSI simulations for the flapping elastic wings have been performed. Based on the DRR results calculated by FEM and FSI simulation, it has been found that FSI simulation is better than FEM simulation for predicting the realistic deformation characteristics. As results, DRR has decreased about 50% without fluid force effect, which is bases on E_c=533 and E_p=133 GPa and membrane thickness of 70 μm has occurred. Otherwise, the deformation effects to thrust-production from FSI simulation have been close to actual behaviors. In particular, FEM simulation has not been sufficient to predict the realistic defamation and thrust force. Thus, FSI analysis is better way to obtain the realistic deformation behaviours and thrust force. Also, it has been demonstrated that the way of rib-wing can be used for specifying the characteristics of the wing's deformations as well. Otherwise, it will be benefit to the areas of passive flow control for fluid engineering. In additional, it is found that the maximum deformations of FEM results have been different about 25% and 45 % with FSI results for E_C = 133 and 533 GPa, respectively.

Besides, the elastic deformation effects to the lift-production have been smaller than the thrust-production as being the same angle of attack (α=0°). In cases of the elastic wing structure, as well as FSI simulation, the deforming velocity has dominated more the lift- and thrust-production through the pressure surface on the wing than the flapping rigid wing structure. Hence, the structural engineering has to make a good wing's deformation to increase the thrust force and average lift in one flapping cycle. In addition, it has been found that both the max-pressure difference and max-deformation have affected to make high dynamic thrust, because of that the same direction of the flapping and deforming velocity cause the high surface pressure. Hence, wing's deformation generates the driving force (thrust). Especially, the flapping velocity has mainly dominated the generation of leading-edge vortex (LEV), which is has affected the lift-production rather. On the other hand, the deformation has slightly affected the vortex structures. Thus, it has been difficult to distinguish the deformation effects on the vortex structures, and to predict the thrust-production from vortex structure viewpoint either.

Moreover, based on the view point of momentum analysis, the relationship between the flow momentum on the wing surface and the dynamic thrust has been considered. It has been found that the high thrust force generated by flapping elastic wing has been occurred by high changing of flow momentum over the wing. Especially, it exists behind occurred the maximum deformation, because of the structural momentum which consists with the flapping and deforming velocity. Flow momentum is an opposite direction with the deformation. Otherwise, these thrust force acts on the boundary of fluid domain equally. Fluid boundary velocity is equal to the wing surface at the interaction region due to that is no slip condition.

Finally, DRR's principle, which is simple prediction method, has been developed to predict the thrust force affected by the elastic deformation for the wings. The results are compared with simulation results for the wing structure without rib-wing and within rib-wing. By comparing, it is found that new thrust coefficient is closed to the simulation results, which an error of 8% and 18 % have occurred for high thrust and small thrust force region, respectively. Furthermore, the phase difference of the maximum flapping and deforming velocity causes to make the different phase in DRR and thrust either, because of the combination of both high momentum and high deformational velocity has dominated the highest thrust force. In addition, their highest combination has occurred at the maximum trailing-edge deformation on the wing's membrane. Otherwise, it has the combination of the projection area and pressure difference between top and bottom wing surface. Especially, it can be also explained by that K_{DRR} and C_{DRR}, which K_{DRR} indicates the potential energy caused by the surface pressure and total wing's deformation and the leading-edge deformation indicated by $C_{DRR.}$

CHAPTER V

Conclusions

5.1 Conclusions

Numerical simulations based on FSI as well as FEM simulation have been performed. It has been frond that only structural analysis has not been good enough for considering the elastic deformation effects, because it cannot predict the realistic deformation of the wing, and has not obtained thrust force either. Although, FEM simulation has only obtained the deformations, it has been advantages for FSI analysis further. Hence FSI must be necessary to predict exactly the thrust force.

In order to predict the wing's flexibility effects to the thrust production, the way of DRR's principle has been developed to explain the relationships between DRR variations and thrust coefficient. To verify DRR's principle, the reasons of their amplitude and phase difference have been found, as these following are:

First, the amplitude difference, due to highest DRR has been proportional to both the maximum trailing-edge deformation and deformational area, at which point zero deformational velocity ($V_{deform} = 0$) occurs. On the other hand, the maximum thrust coefficient has been dependant on both high amplitude of dynamic pressure difference and the trailing projection area. Otherwise, both DRR and C_T have coupled only with the maximum trailing deformation.

Second, for phase difference, due to the effects of constructive interference between pressure difference, $\Delta p(t)$, and projection area, $A_{TE,deform}(t)$, with the same frequency but different amplitude have occurred, thus the resulting wave of thrust force has been equal to the sum of these two waves. The resulting wave of *DRR* has not only been affected by local $\Delta p\ (t)$, but also three-dimensional deformation of wing structure which can predict the preliminary results by FEM as well.

Especially, one of how DRR can predict the dynamic thrust can also be explained by that K_{DRR} and C_{DRR}, which K_{DRR} indicates the potential energy caused by the surface pressure and total wing's deformation and C_{DRR} represents the volumetric leading-edge deformation. For three-dimensional wing effects, both pressure difference and *DRR* are calculated by integrating their local quantities over the wing's surface. Therefore, it has been reliable for considering the 3D elastic body and the thrust-production very well.

5.2 Suggestions for further work

The present approach can be further extended to 2D structural deformation by considering the deformational area per unit wingspan length. Modifications can be made very easily since the DRR expression is written in general form. Also, it can be extended to the other wing shapes and deformation quantities. With numerical optimization techniques, the method can also be used for designing elastic wings. The viscosity effects can also be studied by incorporating suitable wall shear while calculating the total force by pressure difference in flight direction.

Additionally, investigations of new principle (DRR's principle) created for flexible moving body would be useful not only flyer area applications but also advanced aeroelastic design as well. I hope this work provides sufficient material to highlight the challenges and possibilities in lightweight and small flying robot flight, and will aid future researchers in fluid and structural engineering.

References

[1] Shyy W., et al., 1999, Flapping and flexible wings for biological and micro air vehicles, *Progress in Aerospace Sciences*, vol. 35(5), July 1999, pp. 455 – 505.

[2] Galinski, C. and Zbikowski, R. (2007), Materials challenges in the design of an insect-like flapping wing mechanism based on a four-bar linkage, *Materials and Design*, vol.28(3), February 2006, pp. 783 - 796.

[3] Nguyen, Q.V., Truong, Q.T., Park, H.C., Goo, N.S. and Byuni, D. (2010), Measurement of Force Produced by an Insect-Mimicking Flapping-Wing System, *Journal of Bionic Engineering*, vol.7(supp1), September 2010, pp. S94 – S102.

[4] Tsai, B-.J. and Fu, Y-.C. (2009), Design and aerodynamic analysis of a flapping-wing micro aerial vehicle, *Aerospace Science and Technology*, vol.13(7), October-November 2009, pp. 383 - 392.

[5] Wang, Z.J. (2000). Vortex shedding and frequency selection in flapping flight. *Journal of Fluid Mechanics*, vol. 410(1), September 2000, pp. 323 - 341.

[6] Lian, Y., Shyy, W., Viieru, D. and Zhang, B. (2003). Membrane wing aerodynamics for micro air vehicles. *Progress in Aerospace Sciences*, vol. 39(6-7), August-October 2003, pp. 425 - 465.

[7] Von Ellenrieder, K.D., Parker, K. and Soria, J. (2008). Fluid mechanics of flapping wings. *Experimental Thermal and Fluid Science*, vol. 32(8), September 2008, pp. 1578 - 1589.

[8] Deng, X., Schenato, L. and Sastry, S. (2006). Flapping Flight fot Biomimetic Robotic Insects: Part II – Flight Control Design. *IEEE Transactions on Robotics*, vol. 22(4), June 2006, pp. 789 - 803.

[9] Fujikawa, T., Hirakawa, K., Okuma, S. and et al. (2008). Development of a small flapping robotMotion analysis during takeoff by numerical simulation and experiment, *Mechanical Systems and Signal Processing*, vol.22(6), August 2008, pp. 1304 - 1315.

[10] F. Lehmann, 2004, *Aerial locomotion in flies and robots:kinematic control and aerodynamics of oscillating wings*, Arthropod Structure & Development 33, 331–345.

[11] Zhang, Q. and Hisada, T. (2001). Analysis of fluid-structure interaction problems with structural buckling ang large domain changes by ALE finite element method, *Computer Method in Applied Mechanics and Engineering*, vol.190(48), September 2001, pp. 6341 - 6357.

[12] Junchangpood, A., Fuchiwaki, M. and Tanaka, K. (2010). Study on vortex Structure and Dynamic Forces on Flapping Wings of Small Flying Robot by Numerical Simulation, paper presented in *the 10th Global Congress on Manufacturing and Management(GCMM2010) 2010*, Bangkok, Thailand.

[13] K.D. von Ellenrieder , K. Parker and J. Soria, 2008, *Fluid mechanics of flapping wings*, Experimental Thermal and Fluid Science 32 : 1578–1589.

[14] E. William Green and Paul Y. Oh, 2006, *Autonomous hovering of a fixed-wing micro air vehicle*, in Proceedings of the 2006 IEEE International Conference on Robotics and Automation, Florida , 2164–2169.

[15] C. Galinski and R. Z. bikowski, 2007, *Materials challenges in the design of an insect-like flapping wing mechanism based on a four-bar linkage*, Materials and Design 28, 783–796.

[16] B. Stanford, P. Ifju, R. Albertani and W. Shyy, 2008, *Fixed membrance wings for micro air vehicles: Experimental characterization, numerical modeling, and tailoring*, Progress in Aerospace Sciences, 44, 258-294.

[17] Combes, S.A. and Daniel, T.L. (2003). Into thin air: contributions of aerodynamic and inertial-elastic forces to wing bending in the hawkmoth *Manduca sexta*, *The Journal of Experimental Biology*, vol. 206(1), September 2003, pp. 2999 – 3006.

[18] Mazaheri, K. and Ebrahimi, A. (2010). Experimental investigation of the effect of chordwise flexibility on the aerodynamics of flapping wings in hovering flight, *Journal of Fluids and Structures*, vol. 26(4), May 2010, pp. 544 – 558.

[19] Mazaheri, K. and Ebrahimi, A. 2010 Experimental investigation of aerodynamics with flexible wings of flapping vehicles in hovering and cruise flight *Archive of Applied Mechanics*, Vol. 80(11), pp. 1255-1269.

[20] Mazaheri K. and Ebrahimi A., 2011, Experimental investigation on aerodynamic performance of a flapping wing vehicle in forward flight. *Journal of Fluids and Structures*, Vol. 27, pp. 586-595.

[21] Heathcote, S., Wang, Z. and Gursul, I. (2008). Effect of spanwise flexibility on flapping wing propulsion, *Journal of Fluids and Structures*, vol. 24(2), February 2008, pp. 183 – 199.

[22] Le, T.Q, Ko, J.H., Byun, D., Park, S.H. and Park, H.C. (2010). Effect of Chord Flexure on Aerodynamic Performance of a Flapping Wing, *Journal of Bionic Engineering*, vol. 7(1), March 2010, pp. 87 – 94.

[23] Mantia M.L. and Dabnichki P., 2011, Effect of the wing shape on the thrust of flapping wing. *Applied Mathematical Modelling*, Vol. 35, pp. 4979-4990.

[24] Yen S.C. and Hsu C.M., 2007, Investigation on vortex shedding of a swept-back wing. *Experimental Thermal and Fluid Science*, Vol. 31, pp. 849-855.

[25] Ho, S. et al., 2003, Unsteady aerodynamics and flow control for flapping wing flyers. *Prog. Aero. Scie.*, Vol. 39, pp. 635-681.

[26] Lin C-S. et al., 2006, The thrust and lift of an ornithopter's membrane wings with simple flapping motion. *Aerospace Science and Technology*, Vol. 10(3), pp. 111-119.

[27] Jin, T., Goo, N.S. and Park, H.C. (2010), Finite Element Modeling of a Beetle Wing, *Journal of Bionic Engineering*, vol.7(supp1), September 2010, pp. S145 – S149.

[28] Combes, S.A., Daniel, T.L. (2003). Flexual stiffness in insect wings I, Scaling and the influence of wing venation, *Experimental Biology*, vol. 206, June 2003, pp. 2979 – 2987.

[29] Combes, S.A., Daniel, T.L. (2003). Flexual stiffness in insect wings II, Spatial distribution and dynamic wing bending, *Experimental Biology*, vol. 206, June 2003, pp. 2989 – 2997.

[30] Lentink D. et al., 2008, Vortex-wake interactions of a flapping foil that models animal swimming and flight. *The Journal of Experimental Biology*, Vol. 211, pp. 267-273.

[31] Lui T. et al., 2010, Effects of Flexible Fin on Low-Frequency Oscillation in Poststall Flows. *AAIAA Journal*, Vol. 48 (6), pp. 1235-1247.

[32] Breuer M. et al., 2012, Fluid-structure interaction using a partitioned semi-implicit predictor-corrector coupling scheme for the application of large-eddy simulation. *Journal of Fluids and Structures*, Vol. 29, pp. 107-130.

[33] Kurzin V. B. and Yudin V. A., 2009, Aerodynamic Characteristics of a Thin Airfoil Cascade in an I deal Incompressible Flow with Separation from the Leading Edges. *Fluid Dynamics*, Vol. 44 (2), pp. 178-188.

[34] Little J. et al., 2010, High-lift airfoil trailing edge separation control using a single dielectric barrier discharge plasma actuator. *Experimental Fluids,* Vol. 48, pp. 521-537.

[35] Lehmann F-O., 2004, Aerial locomotion in flies and robot: kinematic control and aerodynamics of oscillation wings. *Arthropod Structure & Development,* Vol. 33, pp. 331-345.

[36] Lehmann F-O., 2001, The efficiency of aerodynamic force production in *Drosophila. Comparative Biochemistry and Physiology Part A,* Vol. 131, pp. 77-88.

[37] Hover F.S. et al., 2004, Effect of angle of attack profile in flapping foil propulsion. *Journal of Fluids and Structures,* Vol. 19, pp. 37-47.

[38] Heathcote S. et al., 2008, Effect of spanwise flexibility on flapping wing propulsion. *Journal of Fluids and Structures,* Vol. 24, pp. 183-199.

[39] Du G. and Sun M., 2012, Aerodynamic effects of corrugation and deformation in flapping wings of hovering hoverflies. *Journal of Theoretical Biology,* Vol. 300(7), pp. 19-28.

[40] Soueid H. et al., 2009, Optimization of the motion of a flapping airfoil using sensitivity functions. *Computers & Fluids,* Vol. 38, pp. 861-874.

[41] Shao X-M. et al., 2010, Numerical studies on the propulsion and wake structures of finite-span flapping wing with different aspect ratios. *Journal of Hydrodynamics,* Vol. 22(2), pp. 147-154.

[42] Sun M., 2005, High-lift generation and power requirements of insect flight. *Fluid Dynamics Research,* Vol. 37, pp. 21-39.

[43] Alam M.M. et al., 2003, Aerodynamic characteristics of two side-by-side circular cylinders and application of wavelet analysis on the switching phenomenon. *Journal of Fluids and Structures,* Vol. 18, pp. 325-346.

[44] Schouveiler L. et al., 2005, Performance of flapping foil propulsion. *Journal of Fluid Structures,* Vol. 20, pp. 949-959.

[45] Rozhdestvensky K.V. and Ryzhov V.A., 2003, Aerohydrodynamics of flapping-wing propulsions *Progress in Aerospace Science,* Vol. 39, pp. 585-633.

[46] Eppler R., 1997, Induced drag and winglets. *Aerospace Science and Technology,* Vol. 1, pp. 3-15.

[47] Ebin, D. E., "The initial-value problem for elastodynamics of incompressible bodies". *Arch. Rat. Mech. Anal.*, **94**(1) (1986), July, pp. 15–38.

[48] Peskin, C. S., "The immersed boundary method". *Acta Numerica.*, **11**(1)(2002), March, pp. 479–517.

[49] Hoffmann, K.A., and Chiang, S.T. (2000). Computaional Fluid Dynamics III. 4th ed., Engineering Education System, Wichita Kan.

[50] Wilcox, D. C. (1998). Turbulence Modeling for CFD, DCW Industries, Inc., La Canada, California.

[51] Menter, F. R., Kuntz, M. and Langtry, R. (2003). Ten Years of Experience with the SST Turbulence Model. In K. Hanjalic, Y. Nagano, and M. Tummers, editors, Turbulence, Heat and Mass Transfer 4, Begell House Inc., 625-632.

[52] Menter, F.R. (1994). Two-Equation Eddy-Viscosity Turbulence Models for Engineering Applications. *AIAA Journal*, vol.32(8), August 1994, pp. 1598 - 1605.

[53] Nakata T. and Liu H., 2011, A fluid-structure interaction model of insect flight with flexible wings. *Journal of Computational Physics,* Vol. 231(4), pp. 1822-1847.

[54] Sugiyama, K. and Sumoto, Y., (2011). A full Eulerian finite difference approach for solving fluid-structure coupling problems. *Journal of Computational Physics*, vol. 230(3), Febuary 2011, pp. 596 - 627.

[55] Guerrero J.E., 2010, Wake Signature and Strouhal Number Dependence of Finite-Span Flapping Wings. *Journal of Bionic Engineering,* Vol. 7 (Suppl), S109-S122.

[56] Sarkar S. and Venkatraman K., 2006, Numerical simulation of incompressible viscous flow part a heaving airfoil. *International Journal for Numerical Method in Fluid,* Vol. 51, pp. 1-29.

[57] Zhang Z. et al., 2008, The simulation of 3D unsteady incompressible flows with moving boundaries on unstructured meshes. Computers & Fluids, Vol. 37, pp. 620-631.

[58] Adkins, D., Yan, Y. Y., "CFD Simulation of Fish-like Body Moving in Viscous Liquid". *Journal of Bionic Engineering*, **3**(3) (2006), February, pp. 147–153.

[59] Miao, J. –M., Ho, M.–H., "Effect of flexure on aerodynamic propulsive efficiency of flapping flexible airfoil". *Journal of Fluids and Structures.*, **22**(3) (2006), April, pp. 401–419.

[60] Aider J-L. et al., 2010, Drag and lift reduction of 3D bluff-body using active vortex generators. *Experiment Fluids,* Vol. 48, pp. 771-789.

[61] LaBryer A. and Attar P.J., 2010, A harmonic balance approach for large-scale problem in nonlinear structural dynamics. *Computers and Structures,* Vol. 88, pp. 1002-1014.

[62] Guo S. et al., 2012, Theoretical and experimental study of a piezoelectric flapping wing rotor for micro aerial vehicle. *Aerospace Science and Technology,* Vol. 20.

[63] Pfeiffer A.T. et al., 2010, Ornithopter flight simulation based on flexible multi-body dynamics. *Journal of Bionic Engineering,* Vol. 7(1), pp. 102-111.

[64] Kamakoti R. and Shyy W., 2004, Fluid-structure interaction for aeroelatic applications. *Progress in Aerospace Sciences,* Vol. 40, pp. 535-558.

[65] Sigal, I. A., Yang, H., Robert, M. D., Crawford Downs, J., "Morphing method to parameterize specimen-specific finite element model geometries". *Journal of Biomechanics.*, **43**(2)(2010), January, pp. 254–262.

[66] Nagata T., Fuchiwaki M., Tanaka K., Study on Vortex Flow Structure and Dynamic Forces on an Elastic Heaving Airfoil by Fluid-Structure Interaction Simulation, Cincinnati, U.S.A, *ICJWSF*, 2010

[67] Fuchiwaki M. and Tanaka K., Detailed Wake Structure behind an Elastic Airfoil, *Journal of Fluid Science and Technology*, Vol.4, No.2(2009), pp.391-400.

[68] Drucker E.G. and Lauder G.V., 1999, Locomotor forces on a swimming fish: Three-dimensional vortex wake dynamics quantified using digital particle image velocity. *The Journal of Experimental Biology,* Vol. 202, pp. 2393-2412.

[69] Ahlborn B. et al., 2002, On drag, Strouhal number and vortex-street structure. *Fluid Dynamics Research,* Vol. 30, pp. 379-399.

[70] Shyy, W. et al. 2008 Computational aerodynamics of low Reynolds number plunging, pitching and flexible wing for MAV application. *Acta. Mech. Sin.*, Vol. 24, pp. 352-373.

[71] Do T. et al., 2010, Numerical study of turbulent trailing-edge flows with base cavity effects using URANS. *Journal of Fluids and Structure,* Vol. 26, pp. 115-1173.

[72] Breitsanter C., 2011, Wake vortex characteristics of transport aircraft. *Progress in Aerospace Sciences,* Vol. 47(2), pp. 89-134.

[73] Levin, O. and Shyy, W. 2001 Optimization of a Low Reynolds Number Airfoil with Flexible Membrane. *CMES*, Vol. 2, pp. 523-536.

Acknowledgements

It is a great pleasure to thank everyone who helped me throughout the process of writing my dissertation. I am sincerely and heartily grateful to my advisors, Professor Kazuhiro TANAKA and Associate professor Dr. Masaki FUCHIWAKI for their valuable guidance, inspiring ideas, stimulating thoughts at every stage of my research work. Also, I am highly indebted and thankful to Professor Toshio KOBAYASHI, Professor Takahiro ITO, Professor Hiroshi SUZUKI, for this encouragement and guidance in the area of fluid engineering.

I would like to especially thank all the staff at Tanaka and Fuchiwak Labotory (T.F.L.), and Library at Kyushu Institute of Technology (KIT), Iizuka campus, for their helpfulness in providing facilities and materials for my research work. And also, King Mongkut's University of Technology North Bangkok (KMUTNB) and ASSURAN International Scholarship Foundation who help me for their encouragement, financial support for the duration of my study. I am sure it would have not been possible without their help.

Finally, my graduation would not be achieved without the support and love of my parents, Mr.Virat and Mrs.Charin Junchangpood, and the woman I love, who helps me in everything and has given me the greatest love and willpower throughout this time. I sincerely thank one and all who have contributed to my research through helpful discussions and in one way or the other.

Appendix

A Validation of flapping motion with experiment results

A.1 Kinematic motion of flapping robot's wing

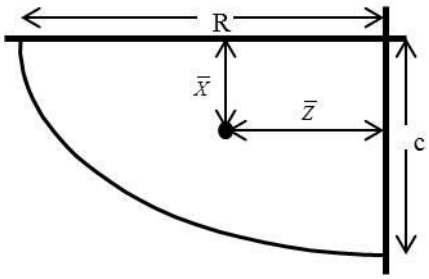

Fig. A-1 Specification of flapping wing model

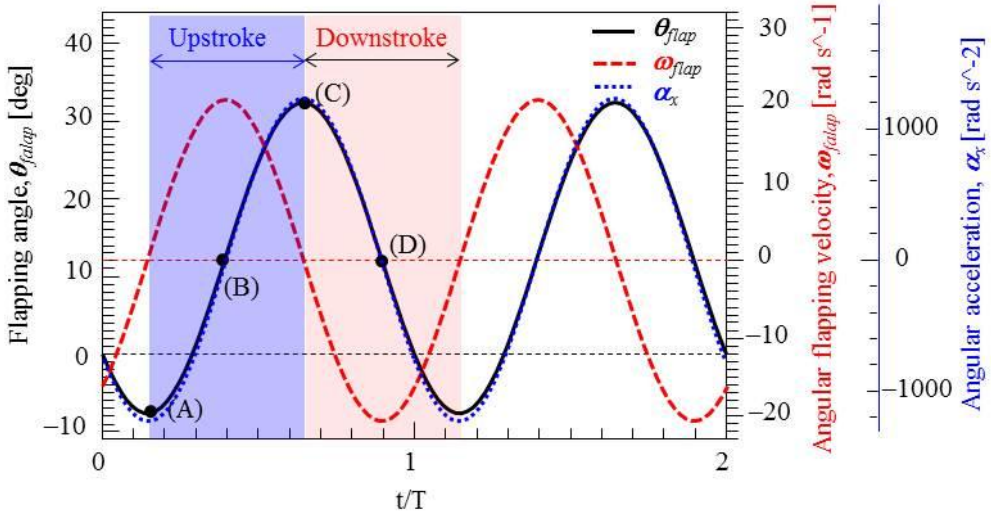

Fig. A-2 Calculating results for flapping angle and angular flapping velocity (10 Hz of one cycle) referred from experiment data

The flapping wing model is illustrated for analysis on the wing's deformation effects, as shown in Fig. A-1. The wing consists of a main frame, no tail and one flexible membrane wings, which the figure shows as only left-side wing. The half-wing span (R) is 120 mm, and its maximum chord length (c) is 80 mm. Due to the wing shape is a semi-ellipse, the average wing chord of 63 mm can be found. In addition, the flapping frequency of about 10 Hz is used for the condition of the flapping motion. Also, the wing's specifications are summarized in Table 8. Fig. A-2 shows the flapping motion used in the simulation. By varying the flexibilities of the wing, one affects the aeroelastic performance of the wing. This change in wing shape and velocity will cause changes in the flow field around the wing. One could attempt to experimentally find the optimum configuration by examining different wing designs [18-20]. Fig. A-3(a) shows the experimental approach to measure some point displacements as shown in Fig. A-3(b). Also, the results are demonstrated in Fig. A-4. Only rigid region has been quite similar with the experiment results.

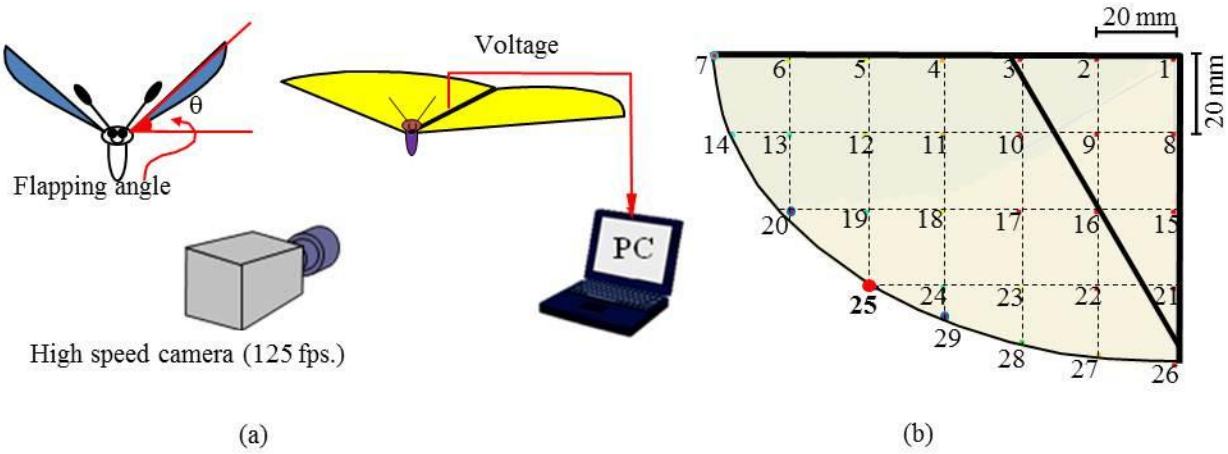

Fig. A-3 Experiment approach for performing the wing's deformation, (a) Schematic of experiment, (b) Point acquired data

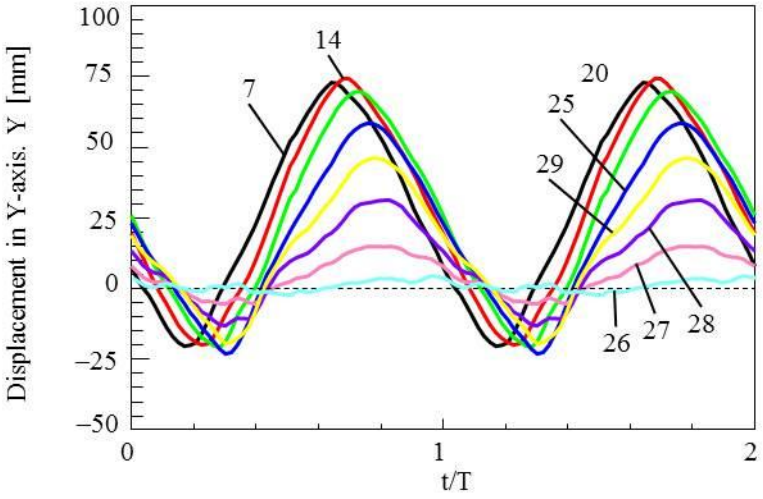

Fig. A-4 Nodal displacement in Y-axis versus the non-dimensional period time, at point of trailing edge

Table 8 Wing's specifications

Parameter	Specification	Parameter	Specification
Wing span (mm)	240	Chord length (mm)	80
Wing aspect ratio	3.82	Mean chord [mm]	63
Flapping frequency [Hz]	10	Half-wing area [m^2]	0.00753982
Upstroke angle [deg]	30	Downstroke angle [deg]	10

A. 2 Dynamic forces based on flapping rigid wing

The objective of these simulations is to compare how different rigid and elastic wing affect the generated aerodynamic forces. Moreover, I would like to find the relations of the combination of the angle of attack, wing flexibility and drag-production. One may note that a rigid wing will not produce high average lift and thrust force, while the wing's deformation will produce high thrust force. The drag and lift coefficient varying with the angle of attack are obtained as shown in Figs.A-5 and A-6, respectively. It can be seen that the angle of attack affects the increasing of an average lift only, but it does not also affect to increase an average thrust (negative drag).

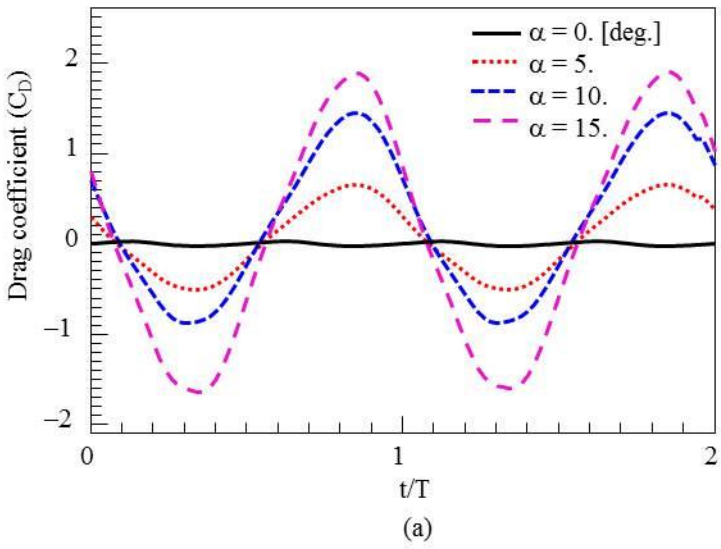

Fig. A-5 Dynamic drag coefficient versus the angles of attack

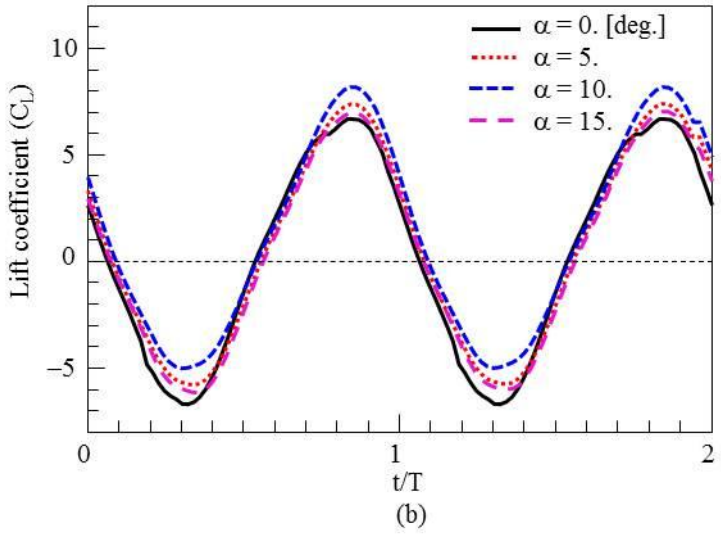

Fig. A-6 Dynamic lift coefficient versus the angles of attack

In addition, both drag and lift coefficient varied with the flapping angle are considered as shown in Fig. A-7 to A-11. It can be seen that the maximum and minimum both drag and lift have occur at the flapping of 18 and 6 degree, respectively. Although, the maximum angular velocity is generated at the flapping angle of 12 degree, however it has not only affected to produce low drag and high lift force. Furthermore, at the top- and bottom-dead position of flapping wing angle, the drag and lift is still generated which may cause of the effects of the unsteady leading edge vortex over the entire wing.

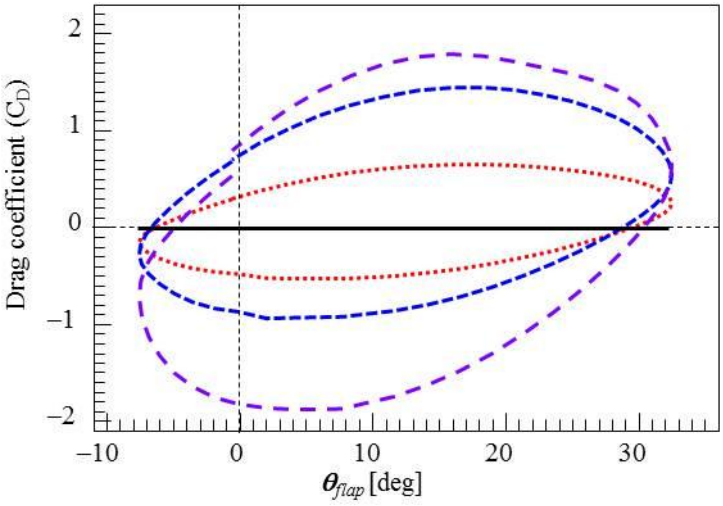

Fig. A-7 Drag coefficient versus the flapping angle

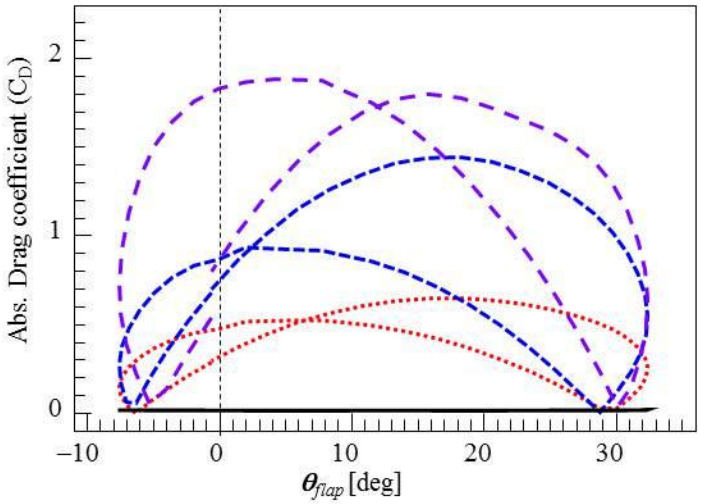

Fig. A-8 Absolute drag coefficient versus the flapping angle

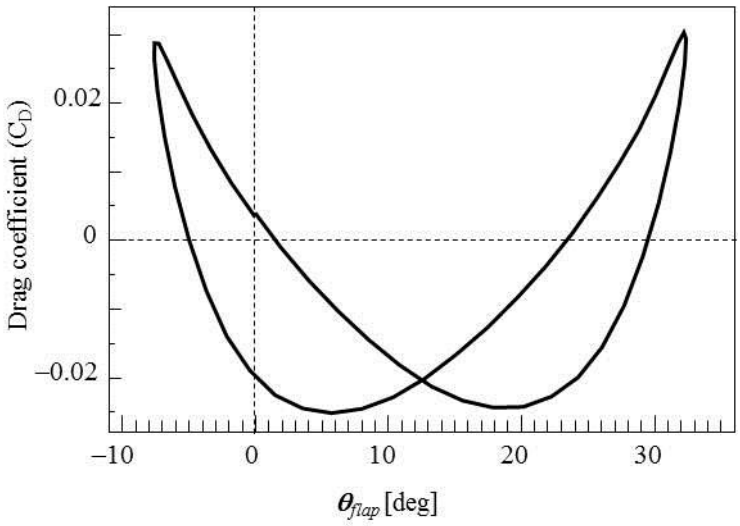

Fig. A-9 Drag coefficient versus the flapping angle (zoom scale), $\alpha = 0.$ [deg]

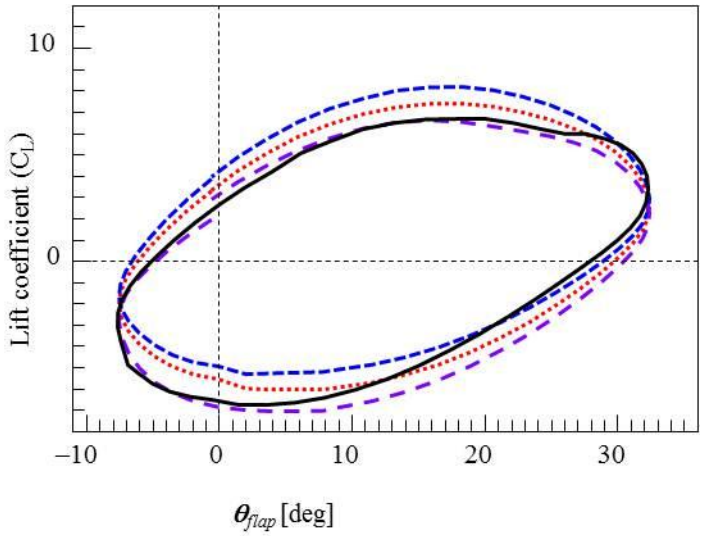

Fig. A-10 Lift coefficient versus the flapping angle

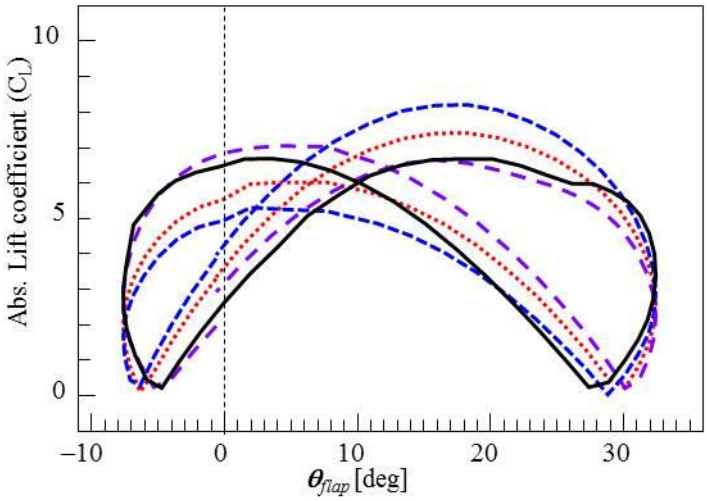

Fig. A-11 Absolute lift coefficient versus the flapping angle

A. 3 Angle of attack effects (AOA) to the wake structures

Figure A-12 shows that a broad wake region is formed downstream for high AOA. On the other hand the fluid forms a relatively narrow wake region which small AOA.

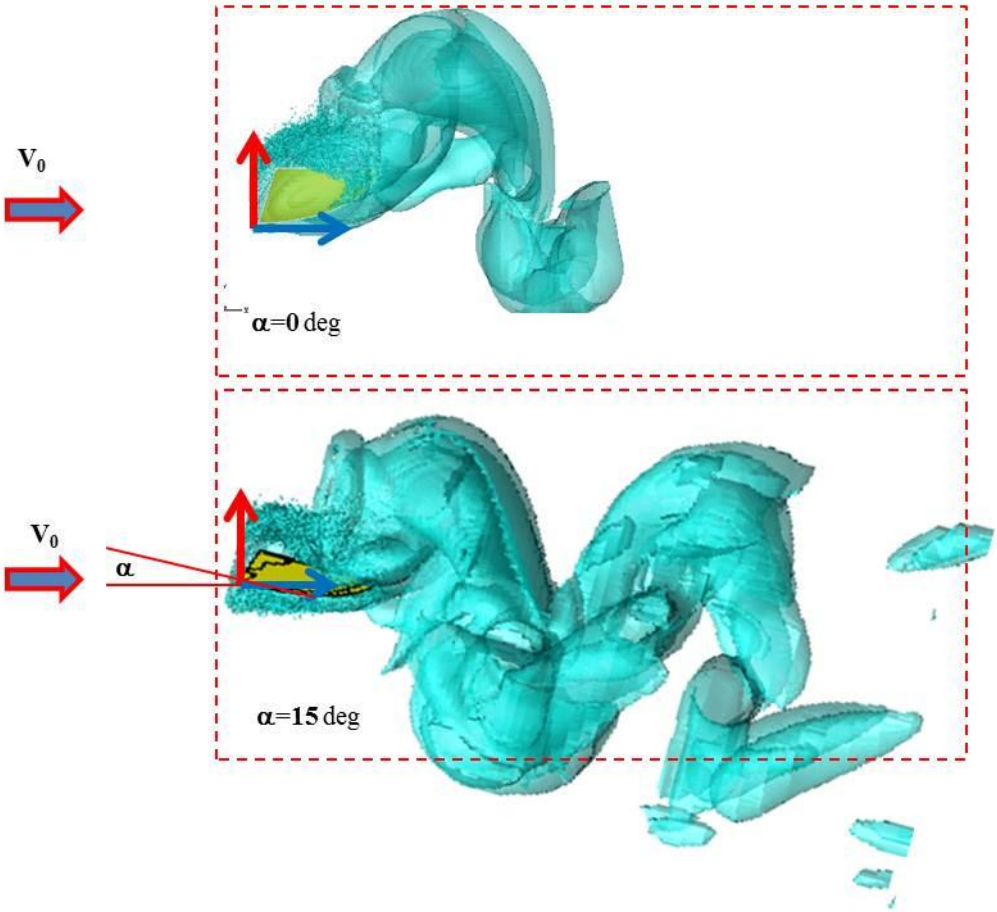

Fig. A-12 Wake structure versus the angle of attack (0 and 15°), ω = 40 [s^-1]

A.4 Vorticity around flapping rigid wing of α=15°

Due to the vorticity can measure of the local rotation of fluid, so Iso-surface vorticity around flapping rigid wing, angle of attack of 15°, is illustrated as shown in Fig. A-13. Sometime, the iso-surface vorticity magnitude is called as the iso-surface of |ω|-cirterion [56]. It can be seen from this figure that increasing angle of attack causes to generate vortex flow and also increase lift force as well (compare with Fig. 3-7).

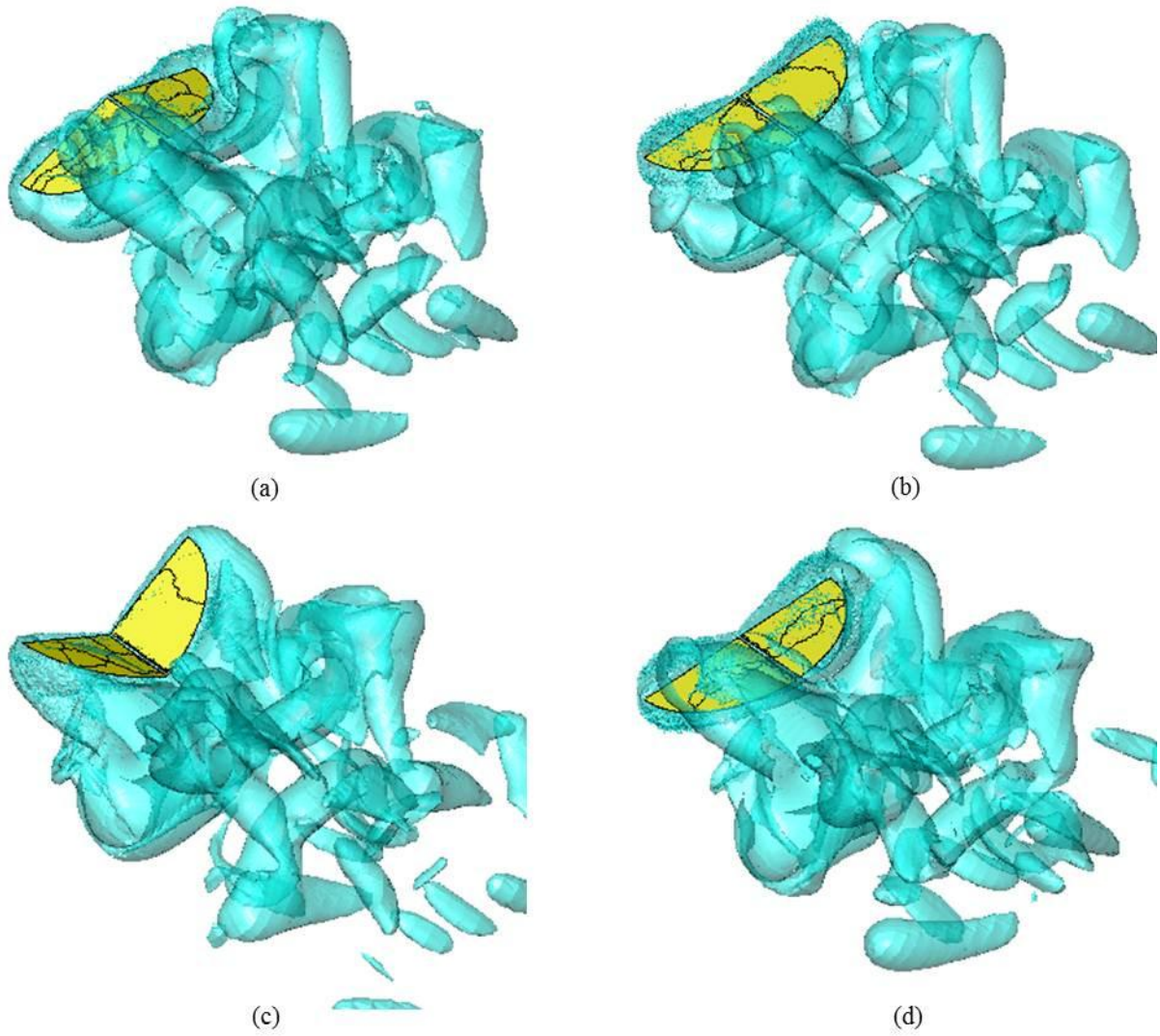

Fig. A-13 Vortex structure visualized as the iso-surface vorticity, ω=40 [s^-1], α=15 [deg], (a) At bottom-dead point, (b) At middle-upstroke point, (c) At top-dead point, (d) At middle-downstroke point

A. 5 Iso-surface of Q-criterion

As found in pervious results of vorticity, that similar vortex structure and wake patterns are obtained, hence other viewpoint based on the Q-criterion was also demonstrated for vortex topology characterization as shown in Fig. A-14. Also, it can be seen that Q-criterion can illustrate vortex structure more than ω-criterion.

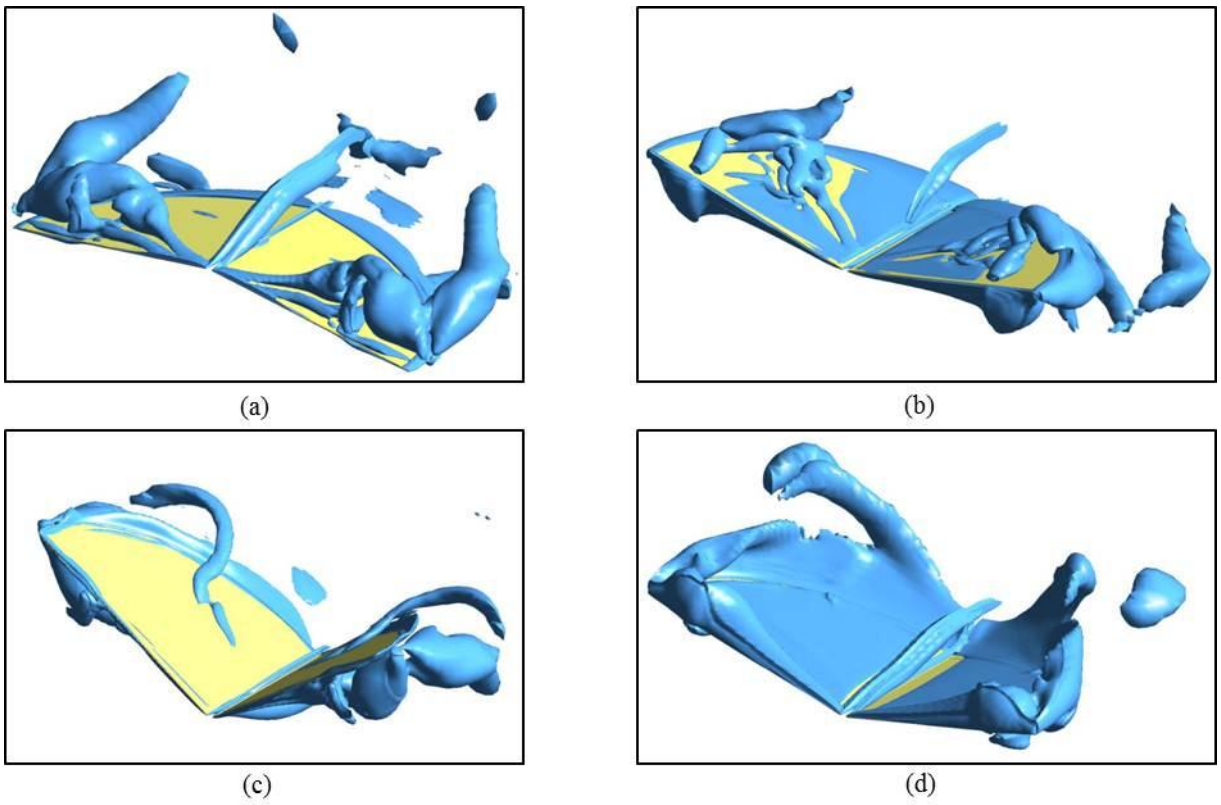

Fig. A-14 Vortex structure visualized as second invariant of the velocity gradient tensor (Q-criterion), (a) At bottom-dead point, (b) At middle-upstroke point, (c) At top-dead point, (d) At middle-downstroke point

B. FEM simulation

B. 1 Damping function for initial condition in FEM simulation

Due to initial condition for transient structural analysis needs to set as being velocity or acceleration of zero, hence I defined the increment function of angular velocity based on flapping time as eq. B-1.

$$K_{damp} = 1 - 2^{kf} \tag{B-1}$$

where K_{damp} is the damping function for initial flapping motion

k is the damping factor [s], = 1, 2, 5 and 10

f is the flapping frequency [s^-1], ≈ 10 Hz

The damping factors were varied as four values for finding the best condition in simulation. From tasting each condition in simulation, k of 2 sec. is the best condition like the results as Fig. B-1. The new flapping angle used for defining the initial and boundary condition are further plotted at five cases of the damping factors in Fig. B-2, correspondingly. It is shown that more than *k* of 5 is quite to be same with no damping effects. However, it can be not used for the boundary condition, because the angular velocity is high increment. It causes to that the solution is uncovered. In the cases of small damping factor, even if it is very good condition for the solution convergence, but it has been high CPU cost and long-time calculating either. By optimized between the solution convergence and time calculating, the damping factor of 2 had adopted for simulation, because is enough to capture the phenomena of elastic deformations. The results should be considered from second cycle of flapping motion which the error of flapping angle and angular velocity are about 3 and 4 percentages, respectively. You can see the difference of the angular velocity between no damping and including the damping effect as in Fig. B-3. .

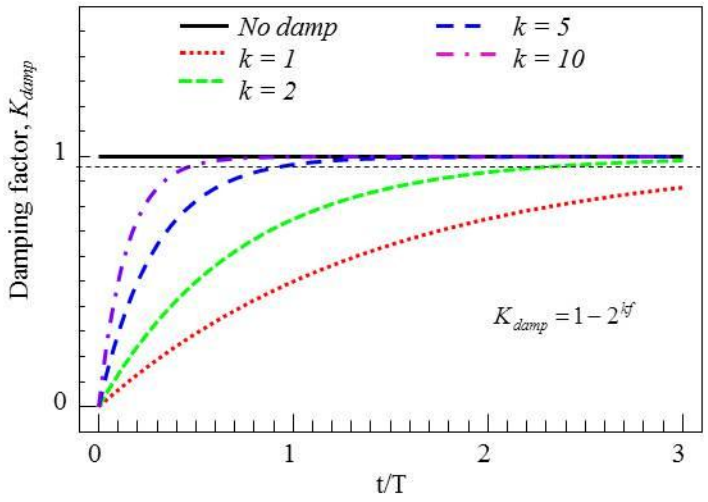

Fig. B-1 Damping factor for initial condition in FEM simulation

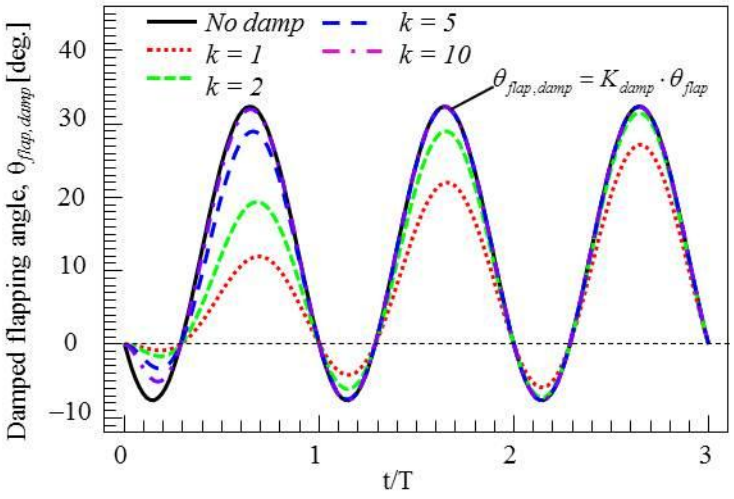

Fig. B-2 Damped flapping angle for initial condition in FEM simulation

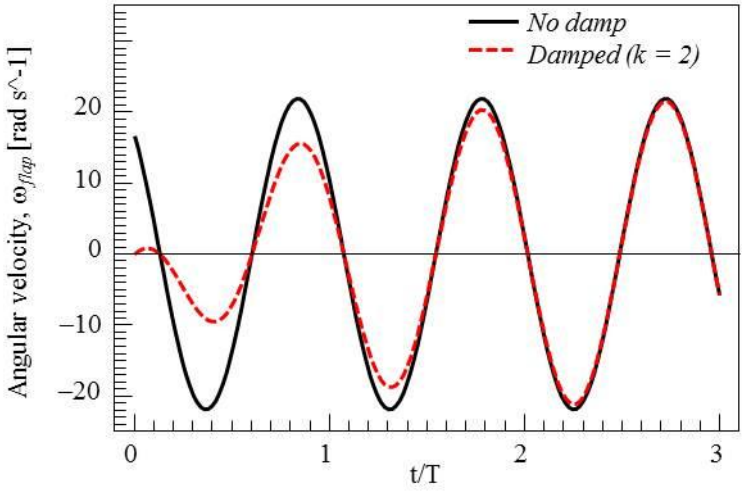

Fig. B-3 Angular velocity for boundary condition in FEM simulation

B. 2 Validation of a structural model for flexible wing.

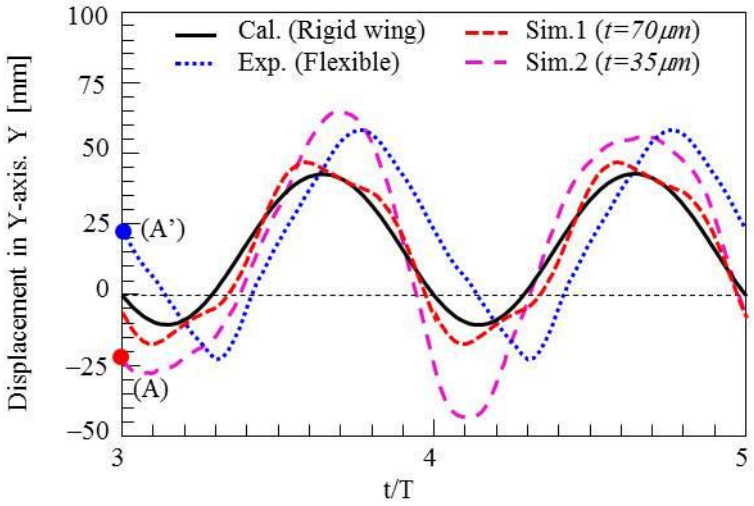

Fig. B-4 Nodal displacement in Y-axis versus the non-dimensional period time, at point of 25

For experimental works, I referred the experimental data from other research, which is actual application of flying robot [11]. The details following this are, the flapping frequency is low (approximately 10 Hz), and the average flight velocity is about 1.0 ~ 2.0 m/s. The schematic of experiment was set as shown in Figure A-4(a). A high-speed camera system with a resolution of 720 x 480 pixels and 125 fps was used for the experiments. The butterfly robot was a free flight. In experiment, the robot parameters are following this, half-wingspan of 120 mm, chord length of 80 mm, and the total robot's mass of 1.9 gram. Twenty nine of position on the wing surface was acquired as shown in Figure. A-4(b). I adopted the point of 25 to compare the displacement component inY-axis wing with calculation results of flapping rigid wing and simulation results either, because the maximum deformation has occurred nearest at this point, as results shown in Figure B-4. The results have been too different, because initial force is only considered and also they are different in the material properties. In addition, . Also, the deformation behaviour is illustrated as shown in Fig. B-5(a) and B-5(b), which is the experimental and simulation result, respectively.

However, the simulation way is better to consider the elastic deformation effects to generate the dynamic thrust force, because they have not obtained both thrust force and momentum flow data yet.

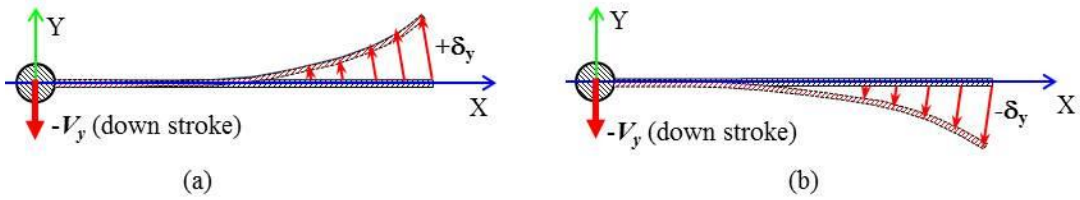

Fig. B-5 Wing deformation behaviour at trailing edge membrane, (a) Experiment at point (A'), (b) Simulation at point (A)

B. 3 Distributions of elastic deformation

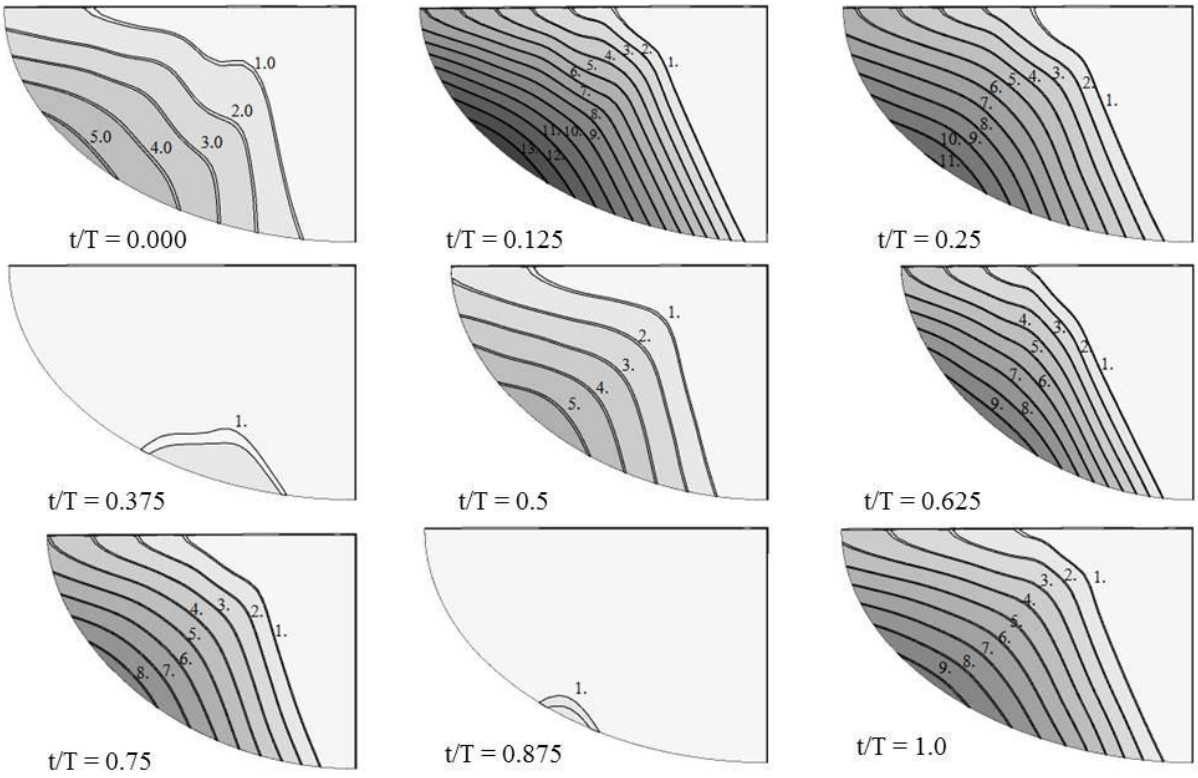

Fig.B-6 Elastic deformation by FEM simulation, Wing A

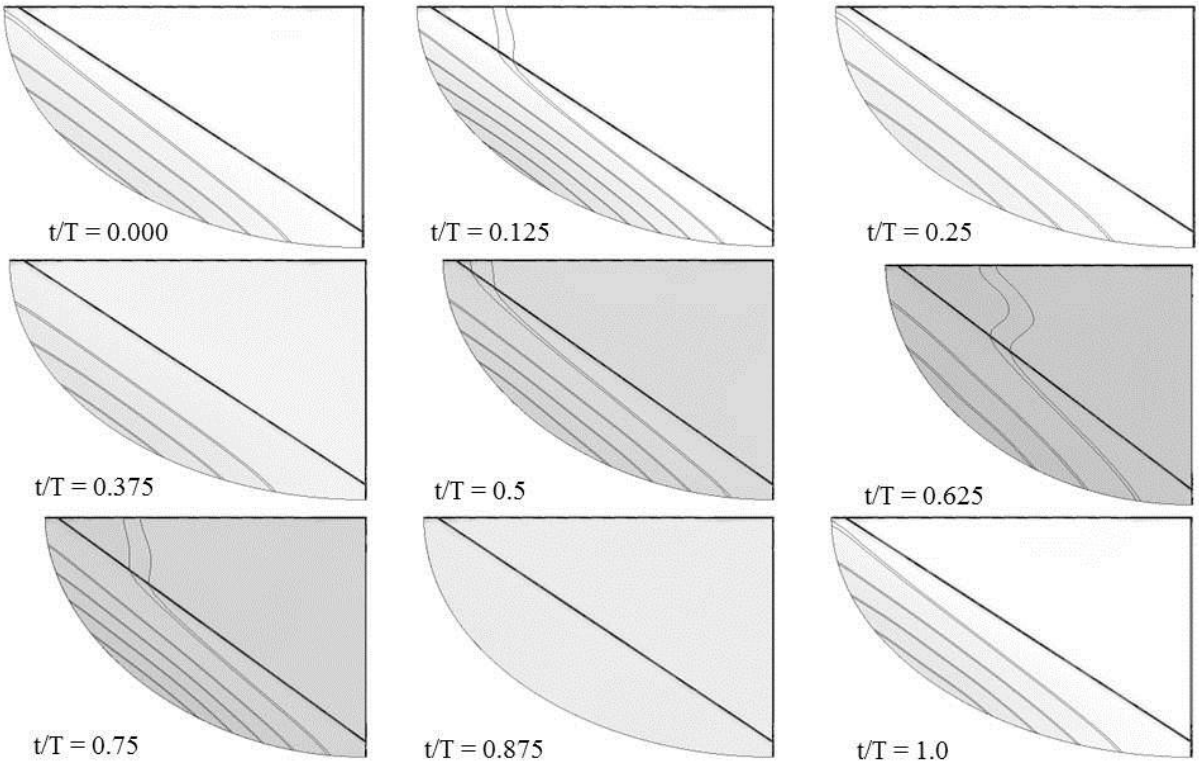

Fig.B-7 Elastic deformation by FEM simulation, Wing D

C. FSI simulation results

C.1 Comparison of FEM and FSI deformation results

By comparison between FEM and FSI results, it is shown that the fluid force effect has increased the max-deformation of about 1.58 (no rib) and 1.41 (within rib, wing D) times of the inertial force effect, which is compared with FEM results (see Appendix B. 3). However, this effects based on the wing's flexibility, thus when wing's flexibility was changed, the fluid force effect would change either. However, FIS simulation is better than only FEM simulation, because it has been able considering the deformation effects to generating dynamic forces.

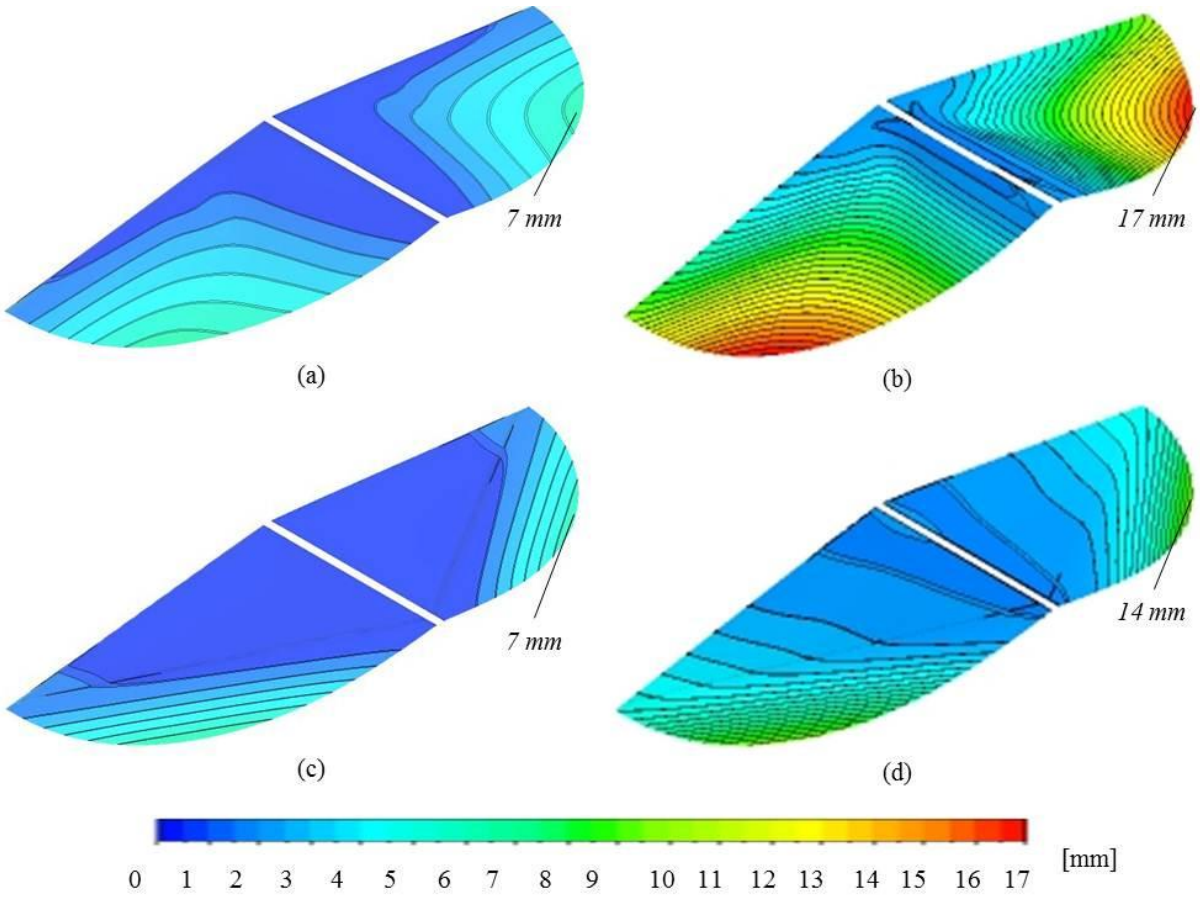

Fig.C-1 Deformation with FEM and FSI simulation, t/T = 0.075, E_C=533 GPa, (a) FEM wing A, (b) FSI wing A, (c) FEM wing D, (d) FSI wing D

C. 2 Vortex structure around flapping elastic wing

The defamation velocity can also be generated lift and thrust either. Hence, the structural engineering has to make a good deformation wings to be used for increasing thrust force and average lift in one flapping cycle.

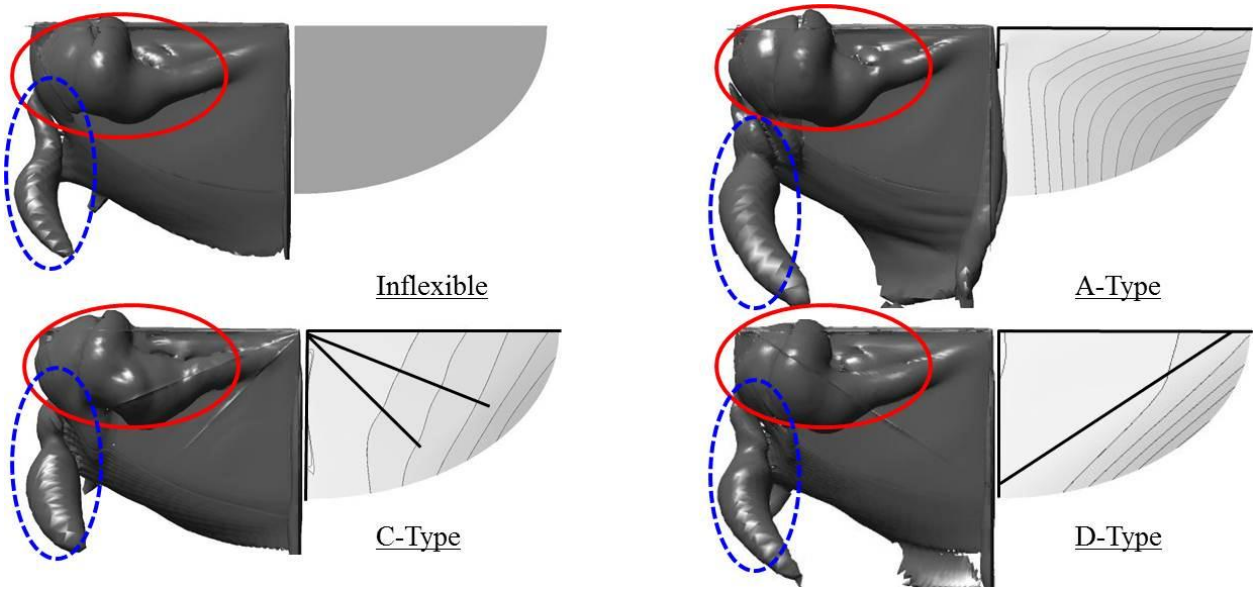

Fig.C-2 Vortex structure around the wing varying with rib-wing, t/T= 0.85, ω =160 [s^-1]

C. 3 Pressure distribution on the wing surface with variations of the rib-wing

In order to find the evidence of the relationship between the vortex structure and generating lift and thrust force, the pressure distributions on the wing surface were considered also.

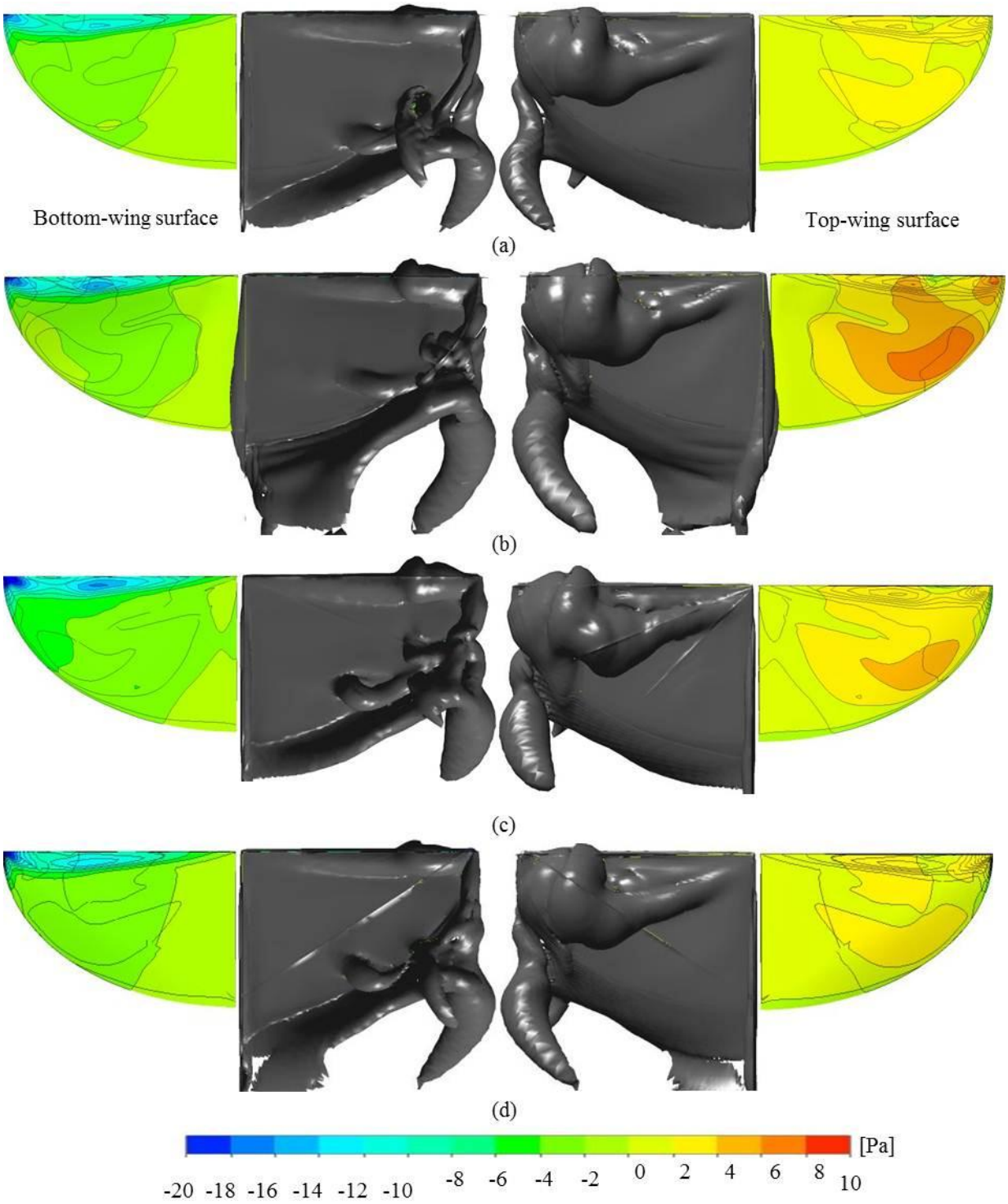

Fig.C-3 Surface pressure for FSI results, (a) Rigid wing, (b) Wing A, (c) Wing C, (d) Wing D

C. 4 Relationships between leading-edge vortex and lift-production on flapping wing

In order to measure the aerodynamic force-production, some researcher has studied about measurement aerodynamic forces with vortex wake dynamic, according to Kelvin's theorem [68, 69]. However, the relationship between the vortex structure and generating lift and thrust force, can be seen rather relation in lift force that thrust force as illustrated in Fig. C-4. Especially the vortex structures are influenced by the velocity swirling strength [70] (Fig. C-4(b)).

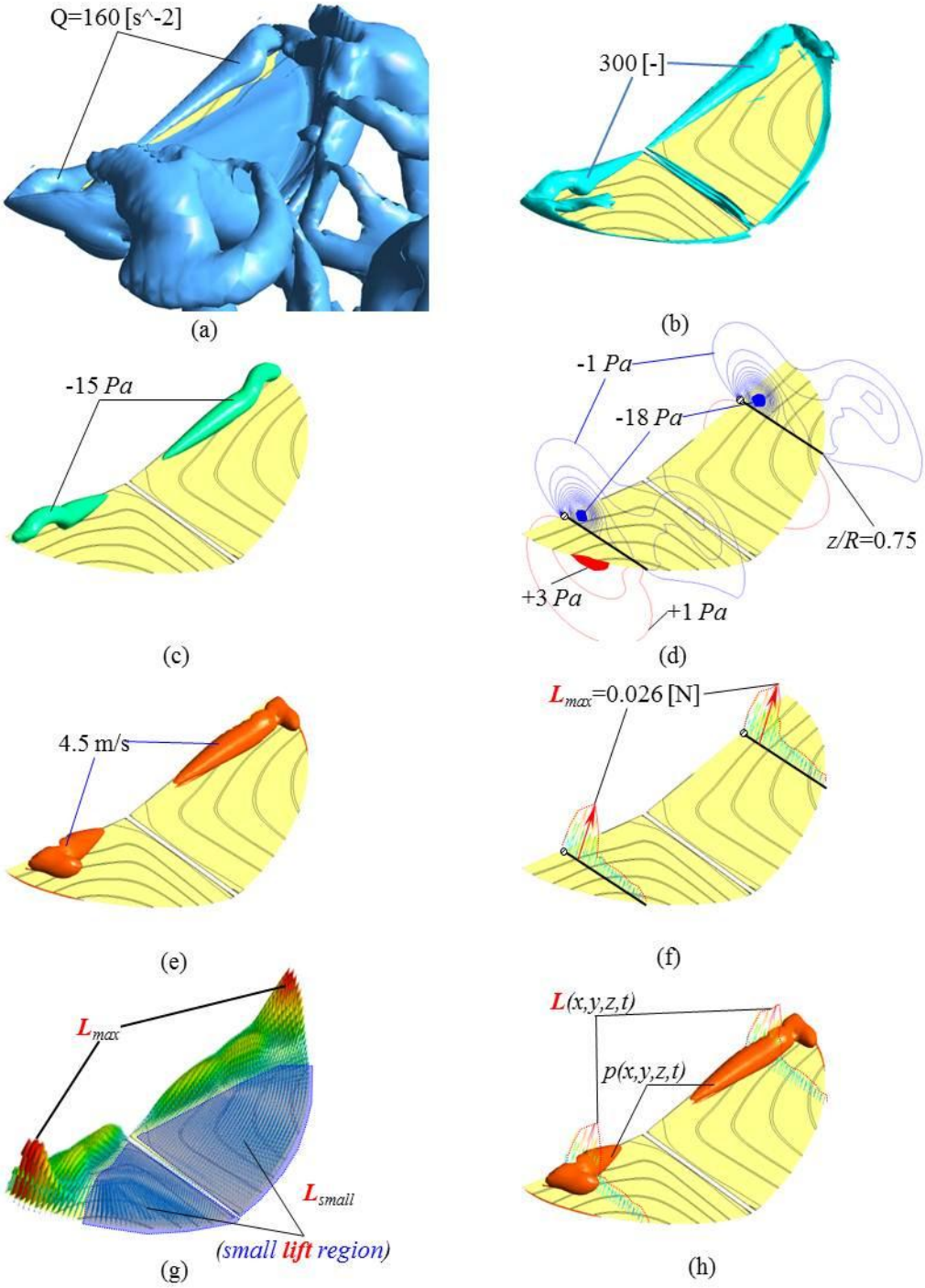

Fig.C-4 Results illustrated the relationships between vortex structure and lift-production, (a) Iso-surface Q-criterion (b) Production of velocity stretched swirling, (c) Iso-surface pressure, (d) Pressure distribution on plane of max-deformation, (e) Iso-surface velocity, (f) Vector of lift-production on the plane at z/R=0.75, (g) Vector distribution of the lift-production on the wing, (h) Lift-production related to vortex structure

D. Invariants of the velocity gradient tensors

D. 1 Calculation of invariants of the velocity gradient tensors

Herein, flow visualization on the elastic deformation effects due to the rib-wing is demonstrated as shown in Figure D-4. It is plotted based on the expressions below. Mathematically, 3-D flow topology is classified in invariants of the velocity gradient tensors.

For the velocity gradient tensor [xx];

$$D = [d_{ij}] = \begin{bmatrix} d_{11} & d_{12} & d_{13} \\ d_{21} & d_{22} & d_{23} \\ d_{31} & d_{32} & d_{33} \end{bmatrix} = \begin{bmatrix} \frac{\partial u}{\partial x} & \frac{\partial u}{\partial y} & \frac{\partial u}{\partial z} \\ \frac{\partial v}{\partial x} & \frac{\partial v}{\partial y} & \frac{\partial v}{\partial z} \\ \frac{\partial w}{\partial x} & \frac{\partial w}{\partial y} & \frac{\partial w}{\partial z} \end{bmatrix} \quad \text{(D. 4-1)}$$

The eigenvalues of gradient tensor satisfies;

$$\lambda^3 + P\lambda^2 + Q\lambda + R = 0 \quad \text{(D. 4-2)}$$

where λ is eigenvalue.

First invariant of velocity gradient tensor,

$$P = -tr(D) = -\nabla \cdot u = -(d_{11} + d_{22} + d_{33}) \quad \text{(D. 4-3)}$$

Second invariant of velocity gradient tensor,

$$Q = \frac{1}{2}[P^2 - tr(DD)] = (d_{22}d_{33} - d_{23}d_{32}) + (d_{11}d_{22} - d_{12}d_{21}) + (d_{33}d_{11} - d_{13}d_{31}) \quad \text{(D. 4-4)}$$

Third invariant of velocity gradient tensor,

$$R = \frac{1}{3}[-P^3 + 3PQ - tr(DDD)] = d_{11}(d_{23}d_{32} - d_{22}d_{33}) + d_{12}(d_{21}d_{33} - d_{31}d_{23}) + d_{13}(d_{31}d_{22} - d_{21}d_{32}) \quad \text{(D. 4-5)}$$

In general tensor form, Q is the second invariant which is defined as:

$$Q = \frac{1}{2}[P^2 - S_{ij}{}_{ji}S - W_{ij}W_{ji}] \quad \text{(D. 4-6)}$$

where $S_{ij} = \frac{1}{2}(A_{ij} + A_{ji})$ is the rate-of strain tensor and $W_{ij} = \frac{1}{2}(A_{ij}A_{ji})$ is the rate of rotation tensor. For incompressible flow the first invariant *P* is zero and all three-dimensional flow topology can be classified in terms of second and third invariant, Q and R respectively. Let's $u_i = A_{ij}x_j$ is nine components of the velocity gradient tensor. From Eq. (D. 4-6), Q of 60 1/s2 was plotted as shown in Figure D-4. It is found that is only small effects of deformation to the rotation flow over the wings. Hence, vortex structure consideration has not distinguished the elastic deformation effects well.

D. Vortex structure obtained by FSI simulation

D.1 Second invariant of the velocity gradient tensor

The objective is to compare the effects of the elastic deformation to the flow field. The second invariant of the velocity gradient can describe how fast the velocity gradient changes, which is illustrated as Fig. D-1 and D-2. It seems that the deformation has lightly affected with macro-scale vortex structure.

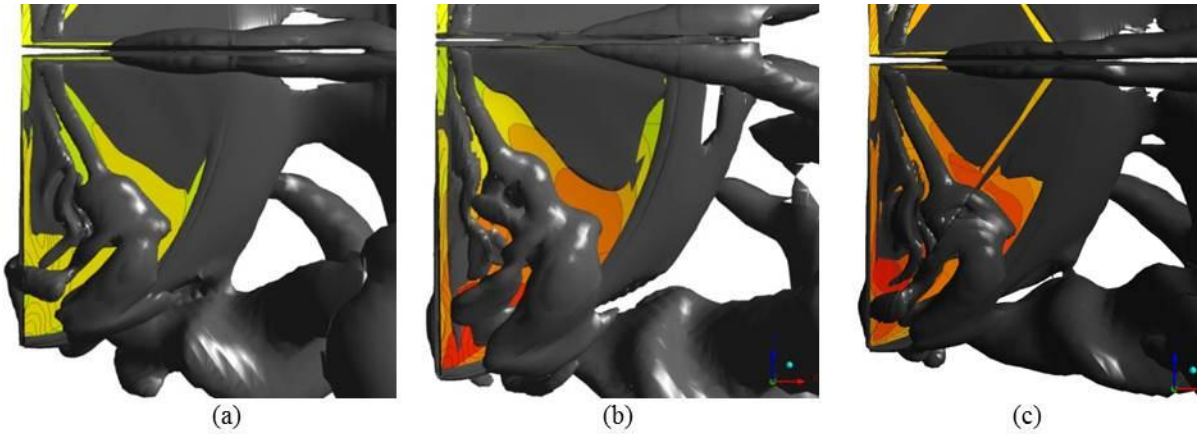

Fig.D-1 Iso-surface of second invariant, Q = 60 [s^-2], (a) Rigid wing, (b) Flexible wing A, (c) Flexible wing D

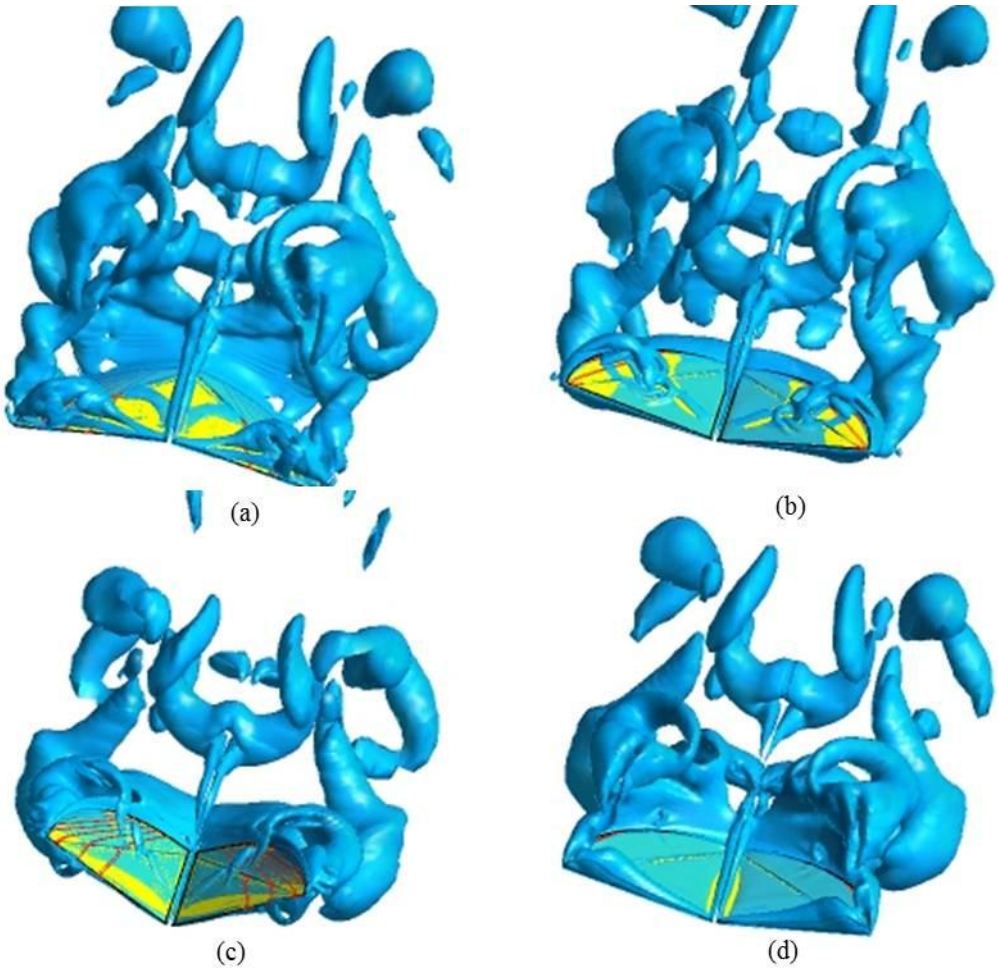

Fig. D-2 Iso-surface of Q = 160 varying the wing positions, Wing D, (a) Bottom-dead point, (b) ving down-center point, (c) Top-dead point, (d) Moving up-center point

E. Combination of Angle of Attack

Due to the trailing-edge projection area causes to increase the angle of attack, thus the deformational angle of attack is also one parameter which affects to the thrust forces as well, which it has been similar tendency with deformational AOA as shown in Figs. E-1(a) and E-1(b). Some research has been reported that the intensity of the vortex strengths at the trailing-edge is amplified, leading to an increase in the mean square pressure fluctuation. Also, it does have an apparent effect on the wake structure, local pressure fluctuations and lift force fluctuations [71, 72]. Although, the angle of attack (AOA) can increase the net lift force and wake structures behind the wings, however it has affected to decrease the thrust force either. Moreover, it has been found that AOA created by the wing's trailing-edge deformation has increased the thrust force as well as the results shown in Fig. E-2.

Moreover, the rib-wing can defined the wing's deformation characteristics, and also it has obtained the similar AOA, which is the result of no rib-wing effects illustrated by the wing A and including rib-wing effects illustrated by the wing D. On the other hand, each wing structure in these cases of studies has generated rather different thrust-production. Hence, it is found that, for flapping flexible wing, not only TE deformation has dominated the thrust force, but also DRR quantity of each wing's deformational characteristics.

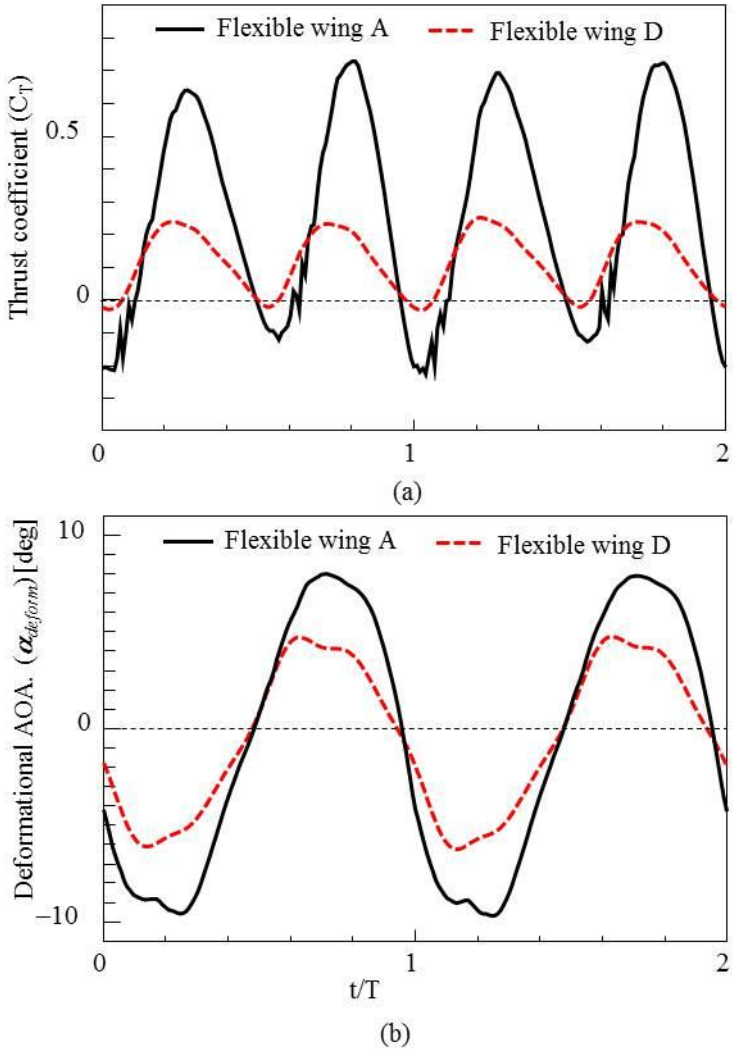

Fig. E-1 Deformational AOA effects, (a) On thrust coefficient, (b) Dynamic deformational AOA

In particular, as this conclusion, we can suggest that you have to consider the DRR variable for evaluating the order magnitude of the deformations, and then it can predict the thrust force on wing's deformation effects as described in Chapter IV.

Furthermore, to obtain a good condition for flight of the flapping robot, which both is enough average lift force in one flapping cycle and average thrust force is more than zero, DRR and rigid angle of attack should be optimize their combination. Based on the flying robot illustrated in this study, which it needs average lift more than 0.02 N, hence it cannot fly forward in rigid wing based on this simulation condition. However, it has been enough thrust force generated by this wing's flexibility. Table 9 summarizes the deformation and AOA effects to the average thrust and lift force. In the Table, the velocity freestream component can be also found, which is calculated by the expression in paper [73]. The negative $V_{\infty,y}$ means the robot can fly upward, which it has occurred at α=10° in rigid wing. According to Newton's second law, the acceleration in thrust direction, a (horizontal), can be calculated by:

$$a_{thrust} = \frac{T_{ave}}{m_{robot}} \tag{E-1}$$

where m_{robot} is the total moss of the flying robot, which is about 2 gram.

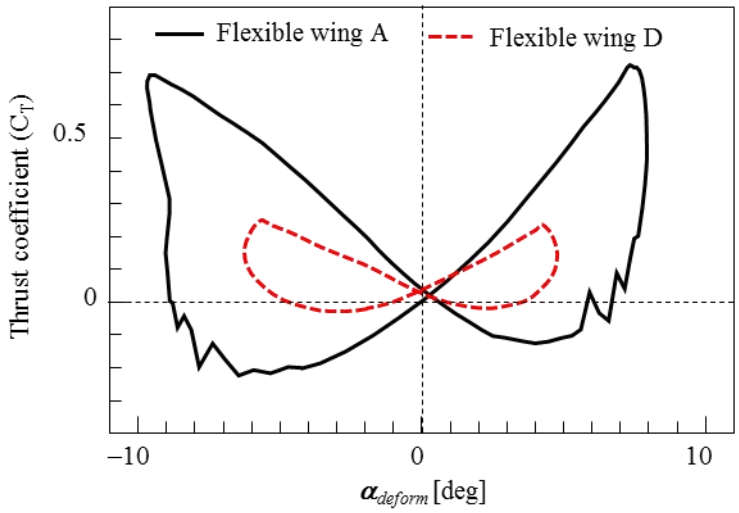

Fig. E-2 Thrust coefficient versus the deformational angle of attack

Table 9 Results of angle of attack effects (two wings)

Parameters/Models	α=0°	α=5°	α=10°	α=15°	$\alpha_0+\alpha_{deform}$ (wing A)	$\alpha_0+\alpha_{deform}$ (wing D)
T_{ave}	-0.00032	-0.00136	-0.004636	-0.002154	**0.00524**	**0.0024**
$C_{T,ave}$	-0.015699	-0.067645	-0.230616	-0.107121	0.261	0.119
L_{ave}	**-0.00063**	0.013014	**0.02523**	0.006864	**-0.00044**	**-0.00026**
$C_{L,ave}$	-0.03134	0.647352	1.255033	0.341449	-0.0216	-0.01247
a (horizontal)	-0.1578	-0.68	-2.318	-1.077	**2.62**	**1.2**
$V_{\infty,y}$	1.073	0.350	**-0.297**	0.676	1.064	1.054

F. Publications/Presentations from the Present Research Work

1. Junchangpood, A., Fuchiwaki, M. Tanaka, K., 2010, "Study on Vortex Structure and Dynamic Forces on Flapping Wing of Small Flying Robot by Numerical Simulation" in Proceedings of the 10th GCMM International Conference on Mechatronics, Bangkok, Thailand, pp. 470-476.

2. Junchangpood, A., Fuchiwaki, M. Tanaka, K., 2011, "Wake Structure around Moving Elastic Airfoils with Projections and Their Characteristics of Dynamic Forces by Fluid Structure Interaction Simulation" in Proceedings of the ASME-JSME-KSME Joint Fluid Engineering Conference 2011, Shizuoka, Japan.

3. Junchangpood, A., Fuchiwaki, M. Tanaka, K., 2011, "Study on an Ideal Elastic Deformation of the Flapping Wing Due to Some Ribs by Finite Element Method" in Proceedings of the 2nd TSME-ICoM International Conference on Mechanical Engineering, Krabi, Thailand.

4. Junchangpood, A., Fuchiwaki, M. Tanaka, K., 2011, "Vortex Structure around Ideal Elastic Deformation of the Flapping Wing Due to Some Ribs" Eighth International Conference on Flow Dynamics (ICFD2011), Sendai, Japan.